THE ADSORPTION OF ENVIRONMENTAL POLLUTANTS IN

GAS AND AQUEOUS MEDIA UTILIZING NANO-SCALE MATERIALS

_____

A Dissertation

Presented to

the Faculty of the Graduate School

at the University of Missouri-Columbia

_____

In Partial Fulfillment

of the Requirements for the Degree

Doctor of Philosophy

_____

by

Nathan R. Bays

Dr. Sheila Baker, Dissertation Supervisor

December 2021

The undersigned, appointed by the dean of the Graduate School,

have examined the dissertation entitled

THE ADSORPTION OF ENVIRONMENTAL POLLUTANTS IN

GAS AND AQUEOUS MEDIA UTILIZING NANO-SCALE MATERIALS

presented by Nathan R. Bays,

a candidate for the degree of Doctor of Philosophy,

and hereby certify that, in their opinion, it is worthy of acceptance.

_____

Professor Sheila Baker

_____

Professor Jerry Atwood

_____

Professor Matthew Maschmann

_____

Professor Timothy Glass

DEDICATION

I am eternally grateful to my friends and family who have always been there for me and supported me. From *the other* Nathan (formally of N^2), for whom I might have to cite my initial interest in the production of porous carbon materials, a.k.a. burned crud. To my lovely sisters who are always there to talk to and keep me positive. My parents who have always been so supportive of my education. And to all the many other family and friends who have helped guide and shape me in innumerable ways. This is in part for you.

Most of all I am thankful for my wife Kelli. To say that without her I would simply not be where I am today is an understatement to an almost criminal degree. Thank you for helping me to achieve my goals and stay sane in the interim.

ACKNOWLEDGEMENTS

I would like to thank Dr. Sheila Baker for the opportunity I was provided to work in her lab.

I would also like to thank all my fellow lab members, Josh McNeely, Ian Siercks, Ryan Hoerr and Alex Carney all of whom I've learned from and were important throughout my work here. I would also like to thank the many other graduate students who I have worked alongside, learned, and gotten assistance from.

And finally, I would also like to thank the Department of Chemistry and the University of Missouri for providing the facilities and resources to complete this body of work.

TABLE OF CONTENTS

LIST OF FIGURES

LIST OF TABLES

LIST OF ABBREVIATIONS

AA	Activating Agent		PC	Porous Carbon
AC	Activated Carbon		PCM	Porous Carbon Materials
BC	Bacterial Cellulose		PEAS	Polyethyoxyamine Sorbents
BET	Brunauer-Emmett-Teller Equation		PFO	Pseudo-First Order
BJH	Barrett, Joyner, and Halenda Equation		PSD	Pore Size Distribution
CCS	Carbon Capture and Sequestration		PSO	Pseudo-Second Order
CV	Crystal Violet		PV	Pore Volume
Dc	Diclofenac		RTIL	Room Temperature Ionic Liquid
DI	Deionized Water		SEM	Scanning Electron Microscopy
eV	Electronvolt		SSA	Specific Surface Area
GAA	Gas Adsorption Analysis		Tc	Tetracycline
His	Histidine		TEM	Transmission Electron Microscopy
IL	Ionic Liquid		TGA	Thermogravimetric Analysis
IPD	Intra-Particle Diffusion		TPV	Total Pore Volume
IR	Infrared Radiation		TSIL	Task-Specific Ionic Liquid
Lv	Levofloxacin		UV-Vis	Ultra-Violet Visible
MB	Methylene Blue		V_{me}	Mesopore Volume
MG	Methylene Green		V_{mi}	Micropore Volume
MO	Methylene Orange		V_{sp}	Single Point Pore Volume
MOF	Metal-Organic Framework		XPS	X-ray Photoelectron Spectroscopy
M.W.	Molecular Weight		XRD	X-ray Diffraction
NOHM	Nanoparticle Organic Hybrid Material			
NLDFT	Non-Local Density Functional Theory			

The Adsorption of Environmental Pollutants in

Gas and Aqueous Media Utilizing Nano-Scale Materials

Nathan R. Bays

Dr. Sheila Baker, Dissertation Supervisor

ABSTRACT
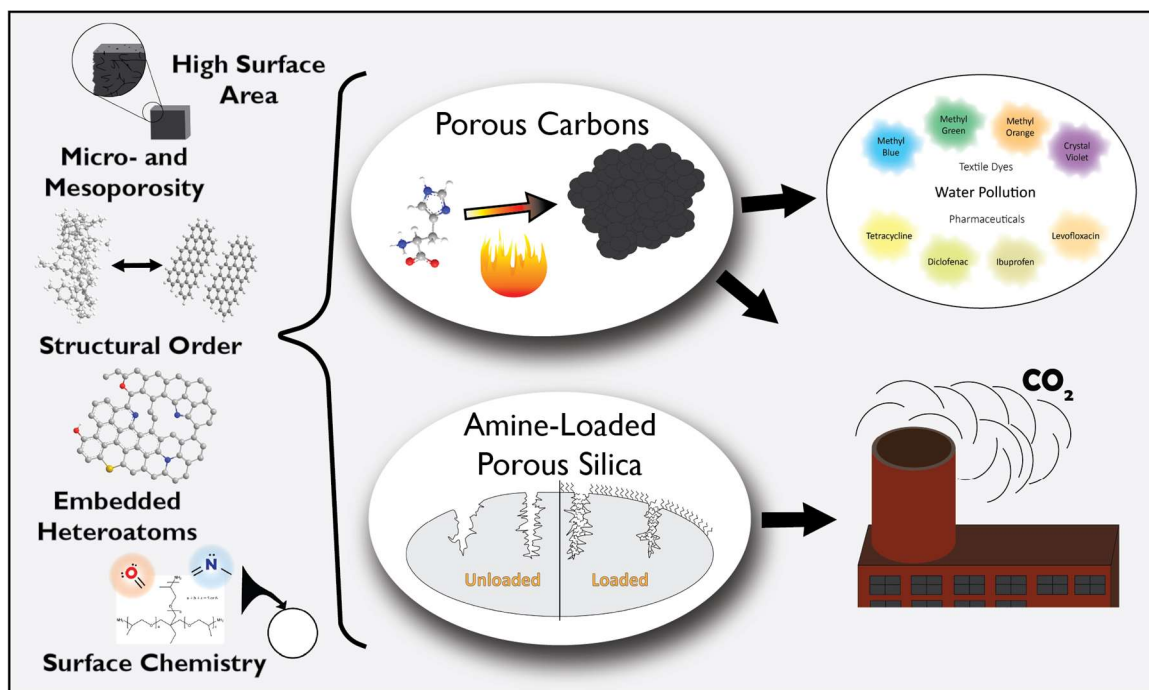
In this body of work, the synthesis and characterization of several nanoporous materials have been described, as well as the application of these materials towards environmentally positive means. Largely, this work involves porous carbon materials produced from the amino acid L-histidine, a porous carbon precursor high in nitrogen and oxygen. Although pyrolysis of this precursor alone produces a non-porous foam, the

introduction of any of a number of activating agents is shown here to produce a variety of amorphous and highly porous carbon materials. While applications of these materials have a very wide range, in this body of work the adsorption of pollutants is emphasized.

Among the aqueous pollutants, both textile dyes and pharmaceuticals were investigated for their abilities to be taken up by these porous carbon materials. Individually, many of the porous carbons were capable of the uptake of noteworthy quantities of various pollutants. Yet, a broader finding in this work was that it appears the 'tuning' of properties on a porous carbon is required to target each different adsorbate; no single property is universally linked to higher capacities.

Apart from aqueous pollutants, the adsorption of CO_2 was thoroughly investigated on many porous carbons. Given their high nitrogen content, it was expected that these materials would do well for CO_2 uptake. And indeed, it was found that several histidine-derived porous carbons were capable of noteworthy capacities, such as 8.30 and 5.57 mmol g^{-1}. Through investigation of the porous carbon textural and chemical properties, these capacities are ascribed to a mixture of physisorption and chemisorption processes.

Finally, the adsorption of CO_2 was investigated on an amine-coated porous silica. With the purpose of making such nano-scale materials more feasible, immobilization inside a bacterial cellulose framework is investigated. Ultimately, it was found that after fine-tuning the loading process, a functional hybrid material can be made that successfully immobilizes the adsorbent material without sacrificing the capture abilities.

1. Introduction

As my time doing research has progressed, I found myself more and more interested and involved in porous carbon materials. With that, the bulk of my research turned towards the synthesis, characterization, and application of these chars. Herein, I will begin by providing a solid introduction into porous carbon materials and then more specifically those that are produced by similar means to my own.

However, my time here has not been solely dedicated to this research. Related in application, I have also conducted considerable research pertaining to loaded porous silica materials and their characterization and functionalization. A separate introduction for these materials is located at the beginning of chapter 4.

1.1 Introduction to Related Porous Carbon Materials

Porous carbons are widely implemented throughout society, having utility in filtration, energy storage, pollutant capture, and medicine to name just a few examples. Porous carbon materials have long been understood to have useful properties; the first documented case of activated charcoal use dates to 3750 B.C.[1] Later, it became commonplace to cleanse or store water with char with the knowledge that this can remove impurities that would otherwise lead to ailment. By the 1700s, these properties began to be more formally described for their applications in medicine.[2] Of course, it was not until

much more recently that the advent of sophisticated instrumentation capable of probing molecular detail that it became fully understood that much of their intrinsic abilities stem from their nano-scale structures.[3]

Among the useful intrinsic abilities of porous activated carbons, their proclivity for adsorption is probably their best appreciated quality and is, in part, the result of incredible specific surface areas (SSAs) which sometimes exceed 3,000 m^2 per gram of material! **Figure 1.** Overall, the wide range of utility in these materials gives way to a perpetual demand for research.
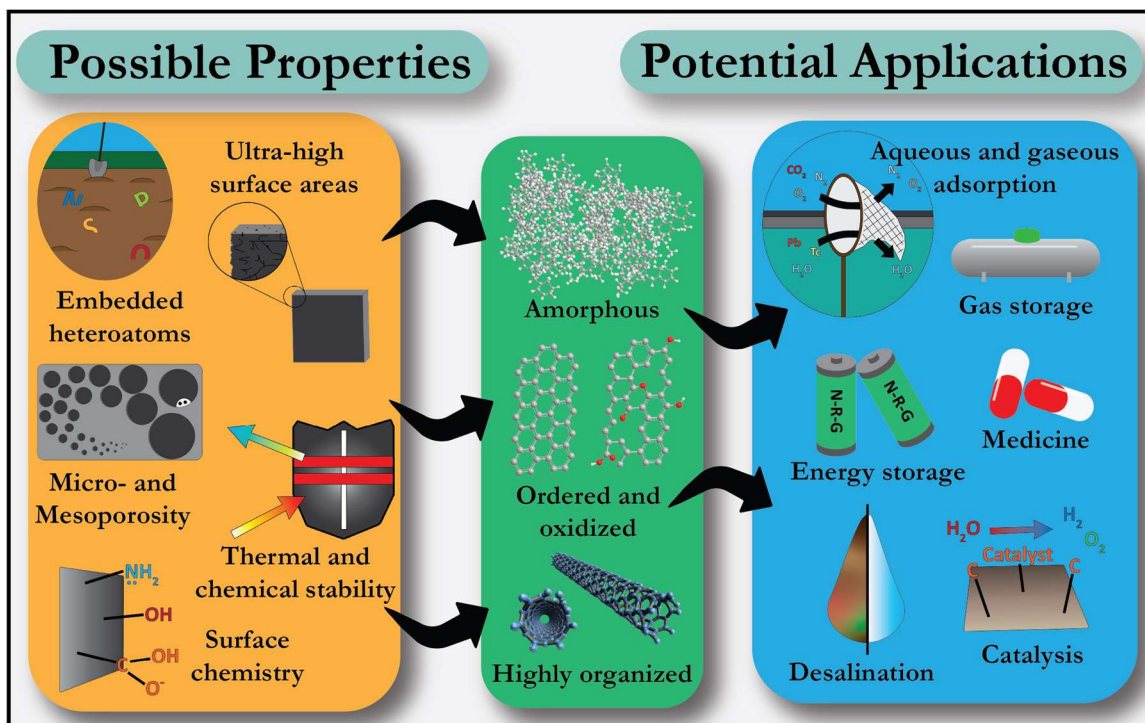
Figure 1. Overview of possible features of and uses for porous carbon materials.

Porous carbon materials also come in a wide range of material types. Because of this, there exist several ways to organize and group these materials. One common way to do so is to consider the degree of disorder in the crystal structure. Highly ordered materials

2

(such as graphite, graphene, fullerenes, nano-onions, single or multi-walled carbon-nanotubes, and related materials) can be seen as clearly distinct with their nearly pure sp^2 hybridized structures. In contrast, materials with disordered structures, such as amorphous carbons, tend to be a blend of sp^3 hybridized carbons that connect, fringe, and pock partially formed, short-range sp^2 structures and lattices. Some methods, such as chemical activation or heat treatment, can lead to a blending of these two classes. For example, highly ordered materials can be chemically or physically activated and lose some or most of their structure. Alternatively, when some amorphous carbons are subjected to sufficient heat, or certain compounds, their structure can be heavily rearranged to form a more organized material.
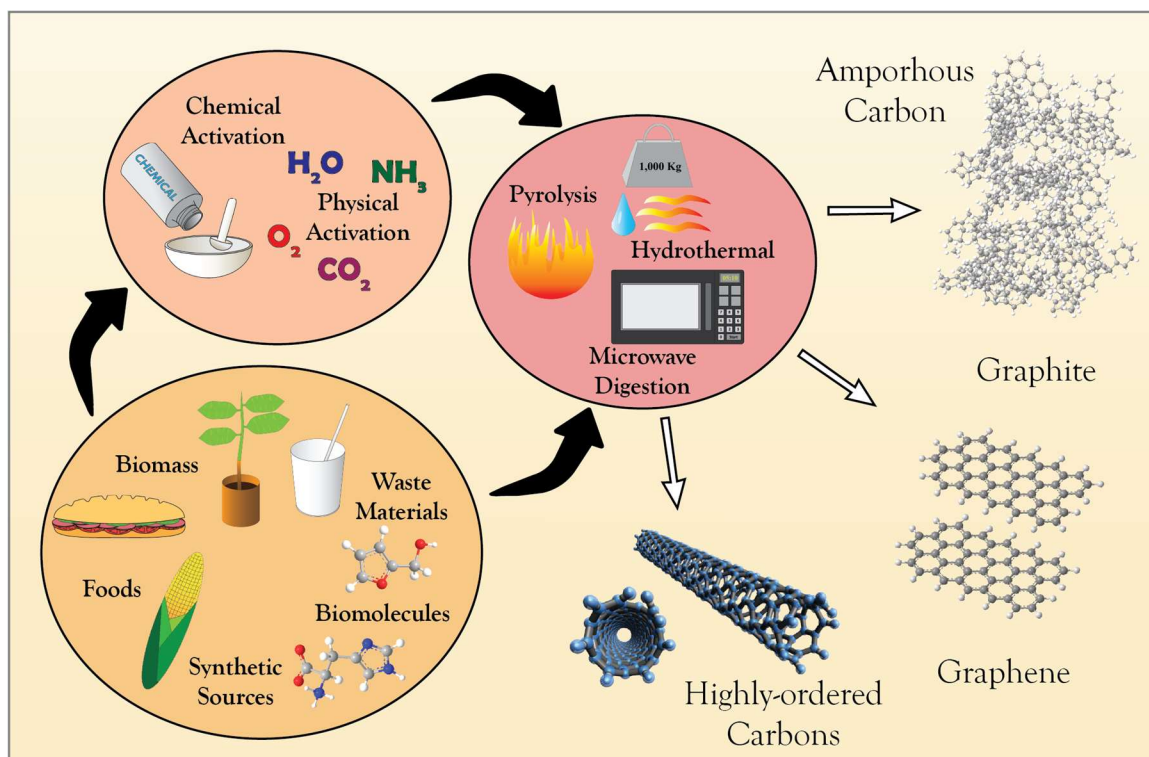
Figure 2. Generalized synthetic route for common allotropes of carbon.

3

Amorphous carbons are highly prized for their porous functionality despite possessing an unorganized structure. This is especially true when one considers that they are often less energy and resource intensive to produce as moderate and alternative activation conditions and inexpensive precursors can often be utilized. They are comprised of the unorganized agglomeration of residual bits and pieces of the precursor material; this results in the tendency of the porous structure to be randomly dispersed and interconnected.

Detecting an amorphous carbon and assessing the extent of its disorder is a relatively simple matter. The lack of highly ordered crystal structure in amorphous carbons means that these materials tend to exhibit broad X-ray diffraction (XRD) peaks at 25° and 43° (implying 002 and 100 lattices) and twin Raman peaks at 1588 cm^{-1} and 1320 cm^{-1} (the so-called 'G' and 'D' peaks, respectively) which are respectively representative of graphitic lattices and the edges and breaks in these lattices (double check this when citing it).[4-6] If the amorphous structure is transformed into a more graphite-like material, these characteristic peaks transform with it. In this case, XRD peaks will become sharper, representing a more organized crystal structure, and the 'G' peak begins to become significantly larger than the 'D' peak. **Figure 3.** Additionally, a 2D peak may emerge around 2700 cm^{-1} - this is affected by the crystallinity, number of layers, and size of the graphitic lattice. Clearly, various types of carbon materials such as amorphous carbon, graphite, graphene, carbon nanotubes, and related structures are at least partially distinguishable using a combination of XRD and Raman spectroscopy.
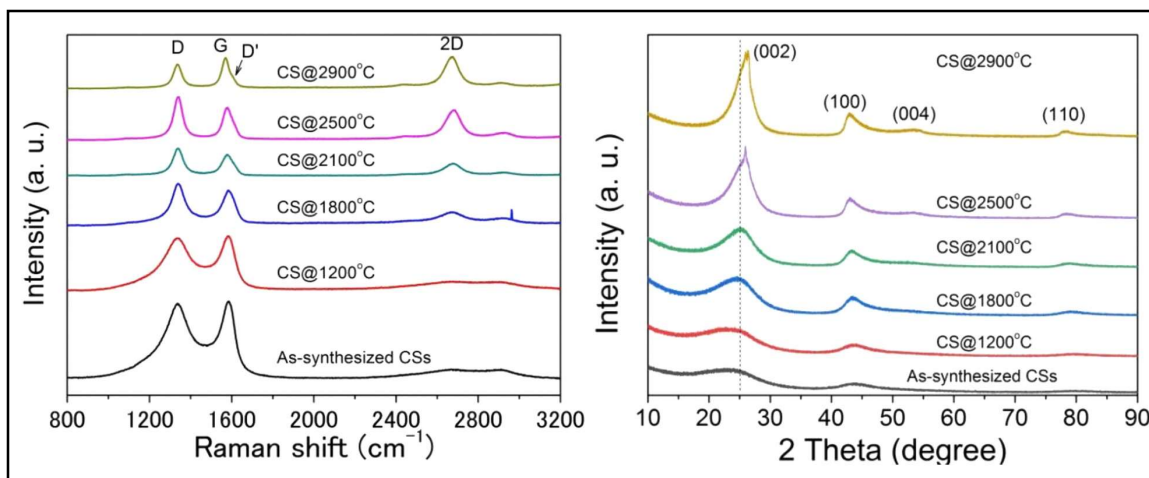
Figure 3. Raman (a) and XRD (b) analysis of PCMs as they are transformed from a more amorphous (CS@1200°C) to a more graphitic (CS@2900°C) structure. From Z. Wang et al. / Carbon 121 (2017), 431.

Porous carbons are generally produced through the pyrolysis of a carbon-containing precursor under an inert gas (often N_2 or Argon) although the specific steps can vary considerably. The classic, and most often used, method of production includes pyrolysis inside a horizontal tube furnace with an inert carrier gas being passed over the precursor material throughout pyrolysis. In the presence of only inert gas, no combustion reaction can proceed. Instead, high-temperature reactions involving the breaking and recombination of the carbon-containing precursor are seen. During this process there will also be many small, volatile molecules swept away by the carrier gas. Still, one will typically end up with a char of significantly larger mass than you would expect from the same precursor undergoing a combustion reaction.

Of course, there are variations upon this standard method, including completely different forms of heat exchange and carbonization. One simple variation upon the previous method has the chamber sealed with no flowing carrier gas, though the increase in pressure because of heightened temperatures and off-gassing of the reaction must be considered.

Increasingly common, however, are alternative methods of carbonization, such as hydrothermal reaction inside a sealed vessel or the use of microwave irradiation to drive pyrolysis. In this introduction some focus is placed upon traditional pyrolysis methods although alternative methods are occasionally considered where relevant.

Pyrolysis often includes both carbon-containing precursor and an activating agent, typically chosen to enhance the final porous carbon material by increasing specific surface area (SSA), modifying porosity, or altering surface chemistry. Activating agents may increase SSA and porosity through several methods, including pore formation and pore expansion. Oxidation of the carbon structure is typical for pore development and leads to the production of structural defects and the outgassing of a variety of small volatile molecular species whose identities are dependent upon the precursor and activating agent used, although CO_2 and CO are always among them. Intercalation, leading to distortion (expansion) of the carbon layers is also common with certain activating agents.

Additionally, activating agents can often append or alter the surface chemistry of the porous carbon materials (PCMs). Specifically, the surface chemistry of carbons can have varying degrees of wettability, be acidic, basic, or neutral, and have a variety of functional groups. Doping agents, such as urea or thiosulfate can be useful for incorporating nitrogen or sulfur into the resultant activated carbon and is common practice when those moieties are deemed useful. Thus, the desired surface chemistry is also a consideration when selecting an activating agent.

While there are a wide variety of activating agents used, some are highly prevalent in the production of porous carbons. There are several good reviews available specifically discussing activating agents, still, it will be beneficial for our purposes here to briefly

discuss the most common ones.[7, 8] The most frequently employed activating agents are simple hydroxides, chiefly KOH, which is also considered to be the most well understood activating agent. KOH is thought to interact directly with the surface carbon structure to produce K_2CO_3 which can further react with the carbon structure to produce CO and metallic potassium. **Equations 1-5.** Metallic potassium can then penetrate deep into the structure and subsequently deform or intercalate the structure from within.

$$2\ KOH \rightarrow K_2O + H_2O \tag{1}$$

$$K_2O + CO_2 \rightarrow K_2CO_3 \tag{2}$$

$$4\ KOH + C \rightarrow K_2CO_3 + K_2O + 2H_2 \tag{3}$$

$$K_2O + C \rightarrow 2\ K + CO \tag{4}$$

$$K_2CO_3 + C \rightarrow 2\ K + 3\ CO \tag{5}$$
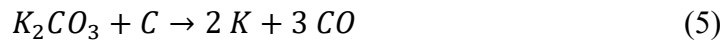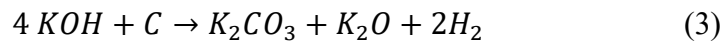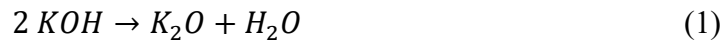
Acidic and neutral activating agents are also used to help activate and/or functionalize the surface of porous carbons. Strong acids, such as H_3PO_4 and H_2SO_4, are common activating agents, though the wide use of these could lead to concerning have environmental implications.[8] Broadly, acidic activating agents tend to result in dehydration, elimination, and oxidation reactions. Neutral activating agents, often employing heavy metals, are common as well, e.g., $ZnCl_2$ and $FeCl_3$. These often activate by oxidation and gasification but can be used as templating agents; some metal ions can even reduce the carbon structure. Again, these are simplifications, and it should be noted

7

that all activating agents are unique in their chemistry and will react differently depending on many factors including temperature, the nature of the precursor, and activating agent-precursor specific reactions.

The type of porous carbon material produced is also necessarily dependent upon the precursor used to synthesize the carbon. Often, high carbon content precursors are used, such as biomass or waste plastics. The presence of heteroatoms such as oxygen, nitrogen, or sulfur are critical to determining the surface chemistry or overall structure of the resultant porous carbon. Utilization of waste biomass, such agricultural byproducts or seasonal debris, is a common and environmentally friendly means of producing porous carbon materials. Upcycling unwanted materials has the potential to decrease waste and reduce the costs associated with porous carbon production. Furthermore, no extra energy or chemicals need be used to produce the precursors. However, due to the natural complexity of these precursors, it can be hard to study and understand the carbonization and activation processes.

On the other hand, simple precursors, often synthetically produced, can provide valuable insight into the carbonization and activation processes. The focus of this introduction is to compare some of these 'simpler' activation systems, with emphasis on the chemical and textural properties of the porous carbons in relation to their precursor components.

1.2 Amino Acid-Derived Porous Carbons

Thanks in part to their natural diversity, several simple biomolecules have been selected and used as PC precursors due to their inherent features. Often, biomolecules are carbon-rich and can also contain heteroatom species, such as nitrogen or oxygen, that are often sought after when looking for precursors. Furthermore, many biomolecules can be produced inexpensively (though not as cheap as waste biomass).

1.2.1 Amino acids

Generalized amino acid

Amino acids as precursors for ACs account for a small but growing number of publications. Amino acids, or, as I am obligated to say, *the building blocks of life*, always consist of three parts: an amino group, a carboxyl group, and an R' group which can take many forms. It is the R' group that differentiates one amino acid from another. This the simplest amino acid is glycine which has a proton as its R'. Generally, amino acids tend to be relatively inexpensive, if not as cheap as waste biomass, are not considered hazardous, and can have relatively high heteroatom ratios (e.g., glycine: NH_2CH_2COOH). For scientific, industrial, and consumer use, amino acids are often produced using microbes or

via protein hydrolysis though ongoing research continues to develop cheaper, more efficient modes of production.[9] Furthermore, considering the application there is not thought to be reason to place reservations on using racemic mixtures that might not be biocompatible. This means amino acids potentially constitute a diverse class of precursors for carbon materials.

Glycine, the simplest amino acid, was the subject of a study by C. Zheng *et al.* who used NaCl as the activating agent and NH_3 as the carrier gas and heated to 790 °C.[10] The produced carbons contained a decent surface area of 741 m^2 g^{-1} that was primarily comprised of micropores though not completely devoid of mesoporosity. The produced carbon also contained very low levels of graphitization, as indicated by broad peaks from both XRD and Raman analysis. Moreover, significant quantities of nitrogen (17.7% via X-ray photoelectron spectroscopy; XPS) were detected in the final product and in cyclized forms. This nitrogen was distributed between pyridinic and pyrrolic forms alone, with a slightly favoring towards pyridinic. Furthermore, tri-s-triazine was detected in the sample via IR. Altogether, this suggests that glycine can form significant porous carbon structures, but that the intrinsic nitrogen played a key role in the formation of the overall carbon structure.

Similarities can be seen in the porous carbons produced by J.-J. Cai *et al.*, who used glycine with and without a templating/activating eutectic mixture of $ZnCl_2$/NaCl at 1000 °C.[11] The resultant carbon, composed of ~1 μm 'beads', was completely microporous and found to have a good BET characteristic surface area of 1548.6 m^2 g^{-1} when subjected to the templating mixture while displaying a respectable surface area of 982.8 m^2 g^{-1} when produced alone. Again, both carbons were shown to be primarily disordered, particularly

when templated (I_D/I_G = 1.81). Though not as prevalent as in the C. Zheng study, nitrogen was still found in significant quantities in the final product. Again, pyridinic nitrogen was the most abundant, with graphitic and pyrrolic being the next most common in the templated and non-templated carbons, respectively.

Thus far, glycine appears to favor disordered structures. In fact, other studies by J. Yan *et al.*, J. Kang *et al.*, and I.-A. Choi *et al.* all further indicate a preference for amorphous carbon products.[12-14] Indeed, the overall crystallinity of the carbons tend to be low. The exception here comes from the study by I.-A. Choi *et al.* who produced carbons with and without $FeCl_3$. In the presence of $FeCl_3$, enlarged (002) XRD peaks are present, and the relative intensity of the Raman spectra is increased when compared to carbons produced without $FeCl_3$. Still, even in this exception, disordered graphitic structures appear to be slightly more predominant.

Another exception in the carbons produced by I.-A. Choi *et al.* is that these are the only glycine-derived porous carbons to contain significant mesoporosity. However, in several samples this is only because of a 20 nm silica template that was used. Still, in other samples, a wide range of mesoporous were present, both with and without the presence of the activating agent $FeCl_3$. Overall, the carbons produced in this study contained low to modest surface areas, ranging from 214 to 740 m^2 g^{-1}. This low BET characteristic surface area could be the result of interactions with the larger 500 nm silica template that was used in every sample produced.

J. Yan *et al.* also used sub-micrometer silica spheres to produce their porous carbons from glycine.[12] Their work showed similar results, with respect to the specific surface area, achieving 451 m^2 g^{-1}. It is worth noting that some macropores appeared to be

present, though this is attributed to dissolution of the silica template. Another interesting deviation in the carbons in this work is the dominant presence of graphitic nitrogen. This is somewhat stifled by the low overall nitrogen content of 3.1-3.8% (XPS). Even so, pyridinic still constituted the second most abundant type of nitrogen.

In another work, J. Kang *et al.* produced their glycine-derived carbons with KCl and KMnO$_4$ in a two-step process that ultimately pyrolyzed at 800 °C. Weak, but present, (002) XRD and Raman I$_D$/I$_G$ bands were detected. What was present suggested a preference for a disordered structure. XPS analysis showed that once again, pyridinic nitrogen was the most prevalent although graphitic and pyrrolic nitrogen were also significant.

This result helps to conclude that carbons produced with glycine as a precursor tend to result in fairly amorphous materials, with moderate surface areas that occasionally peak above 1000 m^2 g^{-1}, and contain significant, if modest, nitrogen contents. However, these conclusions are drawn from the relatively small quantity of research that has been performed on glycine. For a more thoroughly studied amino acid carbon precursor, we must move on to histidine.

Precursor	Template	Activating Agent	Soak °C	SSA m² g⁻¹	V_{total} cm³ g⁻¹	V_{micro} cm³ g⁻¹	V_{meso} cm³ g⁻¹	I_D/I_G	C* %	O* %	N* %	Other %	Ref.
Histidine		-	1000	455	0.232	0.130	0.102	~0.95			3.97, 5.7		15
		-	1500	9	0	0	0	>0.9			1.64, 3.2		
Histidine		-	1000	27				0.98			4.0, 5.7		16
		H_3PO_4	1000	1418				1.14			2.3, 4.3		
		H_2SO_4	1000	1036				1.11			2.6, 3.0		
		HNO_3	1000	534				1.08			5.0, 8.8		
		HCl	1000	504				0.99			4.0, 9.2		
		HBr	1000	464				1.07			3.4, 6.3		
		HI	1000	222				1.06			3.7, 8.2		
Histidine		$KHCO_3$	700	3209	1.66	0.67	0.99	<0.97		16.5	14.5		17
		$KHCO_3$	800	2305	1.52	0.39	1.13	>0.97		13.4	10.0		
		$KHCO_3$	900	2634	1.83	0.46	1.37	0.97		8.0	6.3		
Histidine		phytic acid	800	455	0.24	0.22	0.02	1.07					18
		phytic acid	700	345	0.19	0.17	0.02	1.04					
		phytic acid	800	787	0.43	0.40	0.03	1.19					
		phytic acid	900	571	0.32	0.30	0.02	1.12					
		phytic acid	800	582	0.29	0.28	0.01	1.09					
Histidine		-	200					0.70	46.36	24.32	23.12		19
		-	200						45.47	22.55	26.13		
		-	200						32	42.72	18.5		
Histidine		KOH	800	3083	1.67	1.18	0.49		87.25	10.24	2.51		20
Histidine	SBA-15	$Fe(NO_3)_3 * 9 H_2O$	900	1242	1.4	0.13	1.27		82.0		5.42	Fe% 0.65	21
	SBA-15	$Fe(NO_3)_3 * 9 H_2O$	900	1156	1.2	0.17	1.03		80.7		6.48	0.79	
	SBA-15	$Fe(NO_3)_3 * 9 H_2O$	900	1071	0.7	0.29	0.41		81.1		3.19	0.49	
	SBA-15	$Fe(NO_3)_3 * 9 H_2O$	700	1184	1.2	0.14	1.06		67.5		11.4	0.78	
	SBA-15	$Fe(NO_3)_3 * 9 H_2O$	850	1085	0.7	0.29	0.41		79.9		5.51	1.81	
	SBA-15	$Fe(NO_3)_3 * 9 H_2O$	950	1442	1.7	0.21	1.49		85.5		2.37	0.52	
	SBA-15	-	900	1254	1.7	0.15	1.55		85.8		0	0	
	SBA-15	-	900	1283	1.4	0.13	1.27		82.2		9.4	0	
	SBA-15	Fe	900	653	0.7	0.13	0.57		79.3		0.44	1.07	
	SBA-15	$Fe(NO_3)_3 * 9 H_2O$	900	249	0.3	0.04	0.26		97.8		1.05	0.78	

Table 1. Summary of properties for amino acid derived porous carbon materials. *Data sourced from XPS, elemental analysis, or both.

Precursor	Template	Activating Agent	Soak °C	SSA m²g⁻¹	V$_{total}$ cm³g⁻¹	V$_{micro}$ cm³g⁻¹	V$_{meso}$ cm³g⁻¹	I$_D$/I$_G$	C %	O %	N %	Other %	Ref.
Glycine		1:1 NaCl:ZnCl$_2$	1000	1549				1.81					11
Glycine		-	1000	983									
Glycine		KCl, KMnO$_4$	800					1.15					13
Glycine		KCl	800					1.14					
Glycine		NaCl	790	741				0.99					10
Glycine	Si bead 500	-	900	214							5.57		14
Glycine	Si bead 500	-	900	324							5.85		
Glycine	Si bead 500	FeCl$_2$*4H$_2$O	900	455							3.21		
Glycine	Si bead 500	FeCl$_2$*4H$_2$O	900	740							4.37		
Glycine	Si spheres	-	900	451				1.24	85.88		3.82		12
Lysine		KOH	800	3354	2.5	1.16		0.91		12.52	1.6		20
Lysine		-	900	900	0.378	0.342	0.036	0.96	78.54	16.52	3.82	S% 1.12	22
Lysine		K$_2$CO$_3$	900	2959	1.999	0.55	1.449	1.03	88.9	9.01	1.07	0.99	
Lysine		KOH	900	2370	1.475	0.70	0.775	0.99	85.09	11.05	2.77	1.09	
Lysine		NH$_4$Cl	900	1109	0.504	0.431	0.073	0.98	84.3	7.71	4.8	1.51	
Lysine	CTAB	-	800	1782	4.87			0.81					23
Lysine	Si Spheres	-	900	469				1.23					12
Lysine	Si	FeCl$_3$*6H$_2$O	900	807.6				1.12					24
Asparagine		-	240	177	0.074	0.066	0.008	0.9524	87.78	6.82	3.94	S% 1.45	25
Asparagine		-	240	760	0.326	0.278	0.048	0.9709	90.4	4.9	3.07	1.61	
Asparagine		NaHCO$_3$	900	1300	0.716	0.558	0.158	0.8929	93.2	3.46	2.05	1.28	

Table 1. continued.

14

Table 1. continued.

Precursor	Template	Activating Agent	Soak °C	SSA m²g⁻¹	V_{total} cm³ g⁻¹	V_{micro} cm³ g⁻¹	V_{meso} cm³ g⁻¹	I_D/I_G	C %	O %	N %	Other %	Ref.
Glutamic acid		CuCl₂ * 2 H₂O	900	527	0.24	0.20	0.04	1.85	79.87	16.34	2.77		26
		CuCl₂ * 2 H₂O	900	1358	0.57	0.54	0.03		78.67	15.88	3.64		
		CuCl₂ * 2 H₂O	900	2051	0.88	0.85	0.03	1.72	73.31	21.56	3.22		
Glutamic acid		ZnCl₂	910	1203	0.62	0.55	0.07		79.03, 91.05	14.79, 5.57	4.52, 3.38		27
		ZnCl₂	910	989	0.47	0.45	0.02		77.46, 92.05	17.34, 4.96	3.88, 2.99		
		ZnCl₂	910	761	0.37	0.35	0.02		86.06, 93.31	10.45, 4.91	2.59, 1.78		
		-	910	39	0.023	0.01	0.013		83.72, 86.14	6.35, 11.87	6.06, 1.99		
Glutamic acid		-	700	415	0.23				72.6		10.4		28
		ZnCl₂	700	699	0.37				73.1		7.0		
		ZnCl₂	700	861	0.48				62.6		5.8		
		ZnCl₂	700	1007	0.57			0.72	70.7		7.1		
		ZnCl₂	700	1013	0.59				74.8		7.0		
Proline		Fe(acac)₃, KCl	750	280				0.91	69.98	16.5	1.51	Fe% 12.01	29
Tyrosine		H₃PO₄	800	908	1.08	0.05	1.03	2.6	81.85	11.95	3.70	P% 2.50	30
		KOH	700	1375	1.14	0.43	0.71	2.8	89.07	7.06	2.46	1.41	
		KOH	800	1294	1.75	0.08	1.67	2.7	86.83	8.08	2.19	2.90	
		KOH	800	1877	1.73	0.44	1.29	2.9	90.64	6.59	1.21	1.56	
		KOH	800	1176	1.98	0.23	1.75	3	92.31	5.89	1.47	0.33	
		KOH	900	2024	1.99	0.53	1.46	3.1	91.24	7.37	0.86	0.53	
Proline		Zn(NO₃)₂	900	923	0.80	0.18	0.62	1.0-1.2			3.51		31
Phenylalanine		"	"	1204	1.10	0.34	0.76	"			6.94		
Threonine		"	"	1297	1.25	0.13	1.12	"			6.71		
Tyrosine		"	"	554	0.27	0.22	0.05	"			3.89		
Histidine		"	"	829	0.39	0.31	0.08	"			8.23		
Tryptophan		"	"	183	0.09	0.07	0.02	"			7.91		
Lysine		"	"	765	0.58	0.22	0.36	"			6.53		
Arginine		"	"	62	0.3	0.25	0.05	"			7.64		
Glutamine		"	"	619	0.29	0.25	0.04	"			7.77		
Asparagine		"	"	784	0.47	0.29	0.18	"			5.67		
Aspartate		"	"	989	0.48	0.36	0.12	"			5.93		
Glutamate		"	"	1680	1.00	0.21	0.79	"			4.16		

15

Precursor	Template	Activating Agent	Soak °C	SSA m² g⁻¹	V_{total} cm³ g⁻¹	V_{micro} cm³ g⁻¹	V_{meso} cm³ g⁻¹	I_D/I_G	C %	O %	N %	Other %	Ref.
												S%	
Alanine		-	900					0.93	74.8, 74.9	23.2	2.13, 1.9	0	32
Cysteine		-	900					0.95	64.24, 62.8	35.5	2.69, 1.3	2.74	
Glycine		-	900					1.22	59.39, 49.5	48.2	8.23, 2.3	0	
Niacine		-	900					0.94	85.09, 82.9	15.8	0.83, 1.3	0	
Valine		-	900					0.91	83.23, 85.7	12.8	1.19, 1.5	0	
Lysine		KOH	800	3354	2.50	1.16		0.91	85.88	12.52	1.6		20
Tyrosine		KOH	800	3302	1.87	1.20		0.91	90.34	8.66	1.0		
Histidine		KOH	800	3083	1.67	1.18		0.91	87.25	10.24	2.51		
Histidine	SBA-15	-	900	1225	1.48	0.16	1.32				9.4		33
Tryptophan	SBA-15	-	900	1224	1.47	0.21	1.26				5.4		
Tyrosine	SBA-15	-	900	1392	1.90	0.057	1.843				4.5		
Phenylalanine	SBA-15	-	900	744	1.85	0.026	1.824				6.1		
Glycine	SBA-15	-	900	1280	2.26	0.014	2.246				8.0		
Alanine	SBA-15	-	900								5.6		
Proline	SBA-15	-	900								4.7		
Threonine	SBA-15	-	900	694	1.27	0.05	1.22				4.9		
Serine	SBA-15	-	900	820	0.89	0.11	0.78				4.2		
Glutamic acid	SBA-15	-	900	893	1.59	0.089	1.50				3.6		
Lysine	SBA-15	-	900	862	2.48	0.047	2.43				5.7		
Arginine	SBA-15	-	900	682	0.89	0.096	0.794				7.9		
												Fe%	
Glycine		Glucose	1000	389					97.21	2.15	0.54	0.1	34
Tryptophan		Glucose	1000	318									
Asparagine		Glucose	1000	211									
Glutamine		Glucose	1000	196					95.76	3.51	0.64	0.08	
Lysine		Glucose	1000	175									
Histidine		Glucose	1000	185									
Arginine		Glucose	1000	221					94.69	4.15	0.99	0.17	

Table 1. continued.

1.2.2 Histidine
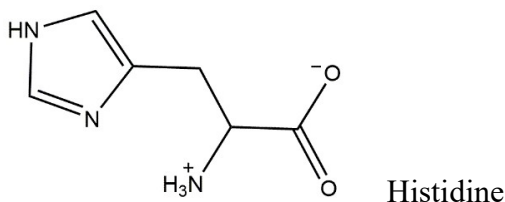
Histidine

Histidine (His) is a nitrogen-rich amino acid containing an imidazole ring as its R'
side chain, produced through biosynthetic pathways in nearly all forms of life.[35, 36] As with
all amino acids, nitrogen and oxygen are present in the amino and carboxyl groups attached
to the α-carbon. In His, the nitrogen content is increased significantly by the presence of
an attached imidazole ring. The side chain is also aromatic, which could assist in the
formation of some carbon structures. These properties have resulted in several publications
utilizing His as both a precursor and an N-doping agent for the production of N-rich porous
carbons.

For example, M. Zhou *et al.* produced PCs activated with $KHCO_3$ that had ultra-
large surface areas while maintaining high nitrogen content.[17] Their sample's SSA peaked
at 3209 m^2 g^{-1} and maintained a 14.5% nitrogen content (wt.%), when activated at 700 °C
with a 1:2 molar ratio. As expected, the nitrogen content was diminished when higher
activation temperatures were used; when the same molar ratio was activated at 900 °C, the
nitrogen content was lowered to 6.3%. Interestingly, despite the His precursor having less
oxygen than nitrogen, the oxygen content is universally higher in all the resultant carbons.
However, this could be resultant of $KHCO_3$ reacting with the carbon structure and leaving
residual oxygen moieties.

Yet, a larger quantity of oxygen than nitrogen appears to be typical of histidine-derived carbons. In fact, one of the largest amounts of nitrogen relative to oxygen appears in the work of M. Zhou *et al.* who used K_2CO_3 as an activating agent and produced nine carbons which had an average of 1.5 times the quantity of oxygen as compared to nitrogen.[17] M. Wang *et al.* produced a study with both experimental and computational methods to further elucidate this outcome.[20] In their work, their histidine derived carbon contained over four times the oxygen content than nitrogen when activated with KOH. The computational work suggested that initially NH_3, CO_2, and H_2O are the most common pyrolytic fragments, but while CO_2 and H_2O production decreases rapidly, NH_3 production increases throughout the pyrolysis process. This suggests that nitrogen is far less stable under such activating conditions.

Graphitic N
Pyrrolic N
Pyridinic N
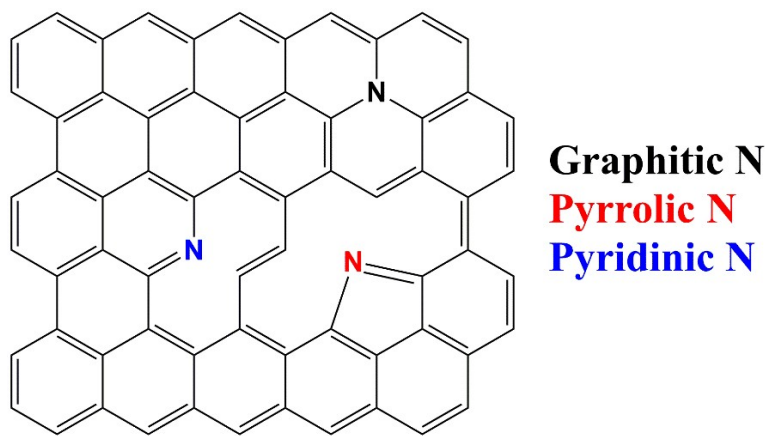
Figure 4. Illustration of some common nitrogen types found via XPS.

Despite typically being smaller than oxygen, the nitrogen content of histidine derived carbons is quite good. As previously mentioned, in their work, M. Zhou *et al.* produced multiple carbons with 14.5+% nitrogen.[17] The nitrogen content in their samples

was primarily associated with pyrrolic and pyridinic structures; however, graphitic nitrogen was also present particularly in the sample activated at the cooler temperature of 700 °C. The nitrogen content and types appear to be heavily influenced by activating agents and do not stay consistent from carbon to carbon. For example, unlike in M. Zhou *et al.*'s work, the work of T.-N. Tran *et al.* produced carbons with a variety of inorganic acids and found that the resultant material's nitrogen content was mostly graphitic nitrogen, with pyridinic, pyrrolic, and oxidized nitrogen also being present in various proportions.[16] Again, histidine-derived carbons produced in studies by C. Peng *et al.* and H. Jeong *et al.* also show inconsistencies in the types of nitrogen present, with the former being comprised primarily of pyrrolic and pyridinic nitrogen, and the latter containing primarily graphitic nitrogen.[15, 18] It is worth noting, that the ratio of graphitic nitrogen does increase with the overall graphitic character of the carbon.

Broadly, histidine-derived carbons appear to favor amorphous structures. This is consistently indicated in the literature by several features, including in the presence and ratios of D and G bands in Raman spectra, as well as TEM imaging. For example, in the work of Thanh-Nhan Tran *et al.* carbons activated with H_3PO_4, H_2SO_4, and HNO_3 had I_d/I_G values of 1.14, 1.11, and 1.08, respectively.[16] Still, it is common to see some ordered structures within the overall amorphous structure. Clear examples of this are the carbon dots produced by H. Huang *et al.*, which are largely amorphous with scattered regions of high order ($I_d/I_G = 0.7$), and the carbons produced by H. Jeong *et al.* which appear amorphous but with frequent random striations occurring throughout.[15, 19]

His-based carbons have, thus far, been found to be primarily microporous. An exception is when His is activated with H_3PO_4, for example in the study by T.-N. Tran *et*

al..[16] Yet, even then the primary source of surface area and pore volume comes from the microporous structure. Indeed, another phosphate-based activating agent was used in a study by C. Peng *et al.* with phytic acid being the activator, and the result was a series of completely microporous materials.[18]

In order to find significant mesoporous character in a His-based carbon, a template must be used, such as in the work of Z. Chen *et al.* who templated with SBA-15, a mesoporous silica while in the presence of iron nitrate.[21] However, the mesoporosity can be attributed to the silica scaffolding rather than the natural development of the His. Indeed, SEM also reveals a structure akin to SBA-15, the template. However, nature of the carbon itself appears to be similar to that of other histidine-based carbons, where the Raman spectra contained relatively even I_D/I_G bands and no graphene peak. Additionally, the nitrogen quantity (9%, E.A.) and type (primarily graphitic nitrogen with additional pyrrolic nitrogen) are similar to other chemically activated His-based PCs, such as those activated with strong acids or $KHCO_3$.

As microporous materials, these carbons tend to have good surface areas and occasionally ultra-high surface areas such as in the work of M. Zhou *et al.* who produced nine carbons with specific surface areas above 2000 m^2 g^{-1} - one having 3209 m^2 g^{-1}.[17] Furthermore, the largest surface areas occurred when the lowest activating temperatures were used, with the peak SSA being achieved at 700 °C. A similar trend was also found in the work of H. Jeong *et al.* who produced two carbons, one at 1500 and 1000 °C, and found that the porous network collapses as you increase the temperature as such.[15] This did come with an increase in the structural order of the material, as indicated by Raman spectroscopy and TEM imaging.

1.2.3 Lysine
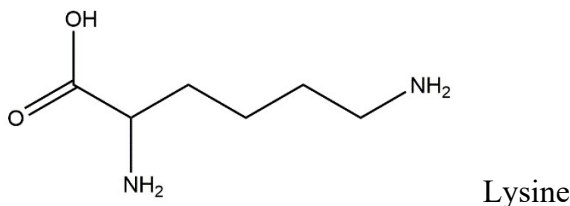
Lysine

Another amino acid with extra nitrogen can be found in Lysine. After lysine's failure as Dr. Wu's contingency plan, life found a way for this little molecule as the precursor of choice in a small but growing number of studies. Lysine is an aliphatic amino acid with an additional terminal amine group. It is an important and common amino acid. In 2015, an estimated 2,200,000 tons were produced commercially on an annual basis.[37] This suggests sufficient supply lines are already in place for the mass production of any lysine-derived porous carbon materials that are deemed worth producing.

Similar to most of the histidine structures previously discussed, electron microscopy and Raman analysis show the structure of lysine-based carbons to be overall amorphous though only a limited set of literature surrounds the production of lysine-based carbons.[20, 31] Even when produced in the presence of a silica nanostructure, they still remain almost completely amorphous in their crystal structure, though they can be observed to partially take up the overall silica structure.[12, 24, 33]

Importantly, the amorphous structures tend to result in ultra-high surface areas. Among the larger surface areas are 3354 and 2959 m^2 g^{-1} for M. Wang *et al.*'s KOH-

activated and H. Zhou *et al.*'s K_2CO_3-activated carbons.[20, 22] The smallest reported surface areas for lysine-based carbons when no silica template is used. It is often seen that lysine-based carbons produce mostly type 1 isotherms but with an extensive uptake after the isotherm 'knee' and minimal amount of type H4 hysteresis. These factors suggest that an extensive range of micropores and small mesopores coexist on these carbons and could be a result of the amorphous nature of lysine-derived carbons. Carbons produced with silica still exhibited microporous isotherms but with additional features resultant of the specific mesoporous silica template used.

Unlike histidine-based carbons, lysine derived carbons were not found to be as effective at maintaining their nitrogen content. For example, in the work of M. Want *et al.*, carbon was produced from both precursors and lysine maintained only a 1.60% (wt.%) nitrogen content compared to histidine's 2.51% nitrogen.[20] X. Gao *et al.* also produced carbons from both precursors (among others) and although the lysine-derived carbon in their study maintained a more significant 5.7% (wt.%) nitrogen content, the histidine derived carbon maintained 9.4%.[33] Still, in that study lysine-derived carbon had around the median nitrogen content compared to other amino-acid derived carbons produced.

Interestingly, the oxygen content of lysine-derived carbons was always larger than the nitrogen content, despite the lysine molecule containing equimolar amounts of each heteroatom. In some cases, this could be a result of the inclusion of oxygen-containing activating agents used. Yet, in H. Zhou *et al.*'s study it can be seen that when carbonized alone or activated with ammonium chloride, the oxygen content is still 4.3 and 1.6 times greater than that of nitrogen.[22] When activated with KOH and K_2CO_3, the oxygen content is 4.0 and 8.4 times greater than nitrogen. Similar oxygen-nitrogen ratios can be seen in

22

other literature, as well. Overall, this would suggest that the carboxyl content is more stable, but wherever O 1s analysis is available for these carbons, a diverse set of oxygens are indicated. Therefore, this might instead suggest that oxygen is simply more adaptable than nitrogen under such conditions, regardless of the initial chemical orientation.

Other Amino Acids

The use of other amino acids as precursors for porous carbon materials is inconsistent, but most amino acids have been used at least once. Often, this comes in the form of surveys, such as those by Y. Wang *et al.*, J. Maruyama *et al.*, and X. Gao *et al.*, where only one method and activating agent is applied with nearly all the amino acids.[28, 33, 34] Yet, some amino acids such as glutamic acid (and its anion Glutamate) have seen increased usage.

In fact, glutamic acid was the study of multiple papers by X.-L. Dong *et al.* and G. Ma *et al.*, who found that as a precursor it is capable of producing high surface area materials while maintain good nitrogen content.[26-28] All three studies applied inorganic metal chlorides (Zn- and Cu-based) as activating agents and found that the resultant carbons were amorphous and primarily microporous in nature. This is contrary to the survey collected by Y. Wang *et al.*, which found that when activated with $Zn(NO_3)_2$ glutamate (glutamic acids anion) produces a high surface area material with 1680 m^2 g^{-1} but with most of its pore volume resulting from mesopores.[31]

Regarding the chemical properties of glutamic acid-based carbons, both Y. Wang *et al.* and X. Gao *et al.* found in their surveys that the oft sought-after nitrogen content was

among the lowest of the tested amino acids, at 4.16 and 3.6%, respectively.[31, 33] Most likely, this is in part due to the low nitrogen content in the precursor, having only one nitrogen. Even more, X.-L. Dong *et al.* found that the nitrogen content determined by XPS was reduced even further than when determined by elemental analysis.[27] This suggests that some of the nitrogen was only retained because it is trapped and is therefore not accessible for application.

The nitrogen content in other amino acid derived carbons can be compared in the survey-like studies. Perhaps unsurprisingly, wherever it was tested, histidine-derived carbons contained the largest residual nitrogen content (2.5 – 9.4%). Though, of course, none contained as high a nitrogen content as the microwave-pyrolyzed carbons produced by H. Huang *et al.* which were up to 26.1% nitrogen.[19, 20, 33] No doubt this is due to its high initial nitrogen content, but it also could be a result of the initial orientation of nitrogen and lack of other functional groups. As noted in their study, Y. Wang *et al.* pointed out that there was not a good linear relationship between precursor nitrogen content and resultant nitrogen content.[31] Instead, they note that other functional groups seem to have an important impact and that the least decomposable functional groups are more often maintained. For example, they found that despite proline having a much larger nitrogen ratio, phenylaniline produced a carbon with twice the nitrogen (6.94 vs. 3.51%) and attributed this to the benzyl group being much more decomposable than the simple carbon chain.

Other carbons were also found to have high residual nitrogen contents across multiple studies, such as glycine- (8 – 8.2%), phenylaniline- (6.9 – 6.1%), tryptophan- (7.9 – 5.4%), lysine- (6.5 – 5.7%) and asparagine-based carbons (5.7 – 3.9%).[22, 31-33] Separately,

tyrosine was also used as a nitrogen doping agent by Y. Ma *et al.*, though the resultant amorphous carbons contained only 0.86 – 2.46% nitrogen after a three-step carbonization/activation process.[30] Similarly, proline was used as a nitrogen doping agent by J. Zhang *et al.* and the resultant carbon contained only 1.51% nitrogen, although large quantities of residual iron nanoparticles might be underinflating nitrogen value in the carbon structure.[29]

Another common thread between amino acid-based carbons is their tendency to produce highly amorphous materials. Indeed, rarely was an I_D/I_G value below 0.9. A notable example of is the glutamic acid-based carbon produced by G. Ma et al., which had an ID/IG value of 0.72. Even this value does not indicate a highly ordered carbon material, and HRTEM revealed a primarily amorphous material with possible small, scattered regions of structure. Largely, I_D/I_G values were around 1 and several authors noted the consistency in the crystal structure between the various carbons.[20, 31, 32]

It has also been noted that amino acids have the ability to polymerize at temperatures approaching 200 °C.[38] This has been suggested to play an important role in the production of these PCMs.[23] This even might impact the preference for amorphous structure development as unorganized and free polymerization at the beginning of treatment are likely to impact the intermediate and final molecular arrangement.

2. Capturing aqueous pollutants using porous carbon materials

Emerging contaminants (ECs) are compounds that are either completely or partially unregulated and pose risk to the health of the environment and humans. Of these, pharmaceuticals and personal care products (PPCPs) are a class of ECs that have been gaining increased attention over the past decade. Among these, tetracycline (Tc) one of the most frequently studied pollutants, though a widening array of compounds are being studied every year. Additionally, textile dyes have been a focus of pollutant capture for quite some time now, in both the capacity of environmental pollutant and model adsorbent for other more pernicious pollutants. Among dyes, methylene blue (MB) is far and away the most commonly studied, and has many reviews dedicated solely to its capture.[39] Still, other dyes such as methyl orange (MO) or crystal violet (CV) are becoming more frequently studied.[40, 41] With the large variety of pollutants introduced into the environment every day, it is important we develop technology to combat this issue.

Among possible techniques that might be implemented to capture these pollutants, porous carbons (PC) are materials that are always highly considered.[42, 43] Large surface areas, active micro- and mesopore structures, and scattered surface functional groups are just three potential reasons for why PCs have potential to be outstanding small-molecule pollutant adsorbents. Indeed, PCs have been shown to be capable of capturing large quantities many different adsorbents. For example, Wang et. produced an activated carbon from distiller's grain and with a massive maximum monolayer adsorption capacity of 934.6

mg g^{-1}.[44] Still, it is not always clear which of the many properties that PCs have is responsible for their large capture capacities.

PCs tend to be high surface area materials with nanoscale features, produced from the pyrolysis of high carbon content materials under inert atmosphere. This process typically results in a carbonaceous material that can come in a variety of structural forms such as graphite, amorphous carbon, carbon nanotubes, and more. Furthermore, structural defects can also be useful in increasing surface area and pore volumes. Chemical features can also be found in the form of surface functional groups, heteroatoms such as nitrogen or oxygen embedded in the carbon structure, or metals or ions intercalated between layers. All structural and chemical features are a result of both the precursor and pyrolysis conditions, as well as the inclusion of any activating agent used to impart or improve specific features.

As mentioned, activating agents are useful in acquiring high-achieving carbon materials. A large number of different compounds have been applied as activating agents and some reviews comparing and contrasting their efficacy and feasibility are available.[7] It can be seen that although some trends do exist, no activating agent produces the same result with every precursor or system. Indeed, activating agents can produce a wide variety of compounds, as they interact differently with every precursor in conjunction with a high energy environment.

The variety of activating agents, activating conditions, and precursors lead to a plethora of different carbon materials with tunable properties. Similarly, the unique characteristics of each pollutant molecule mean that their adsorption is not uniform from pollutant to pollutant. This study was designed to address this problem systematically and
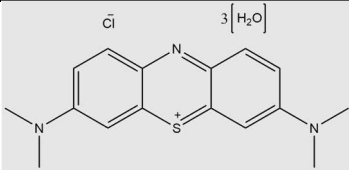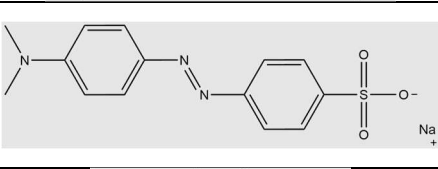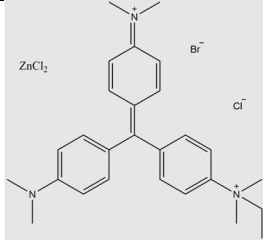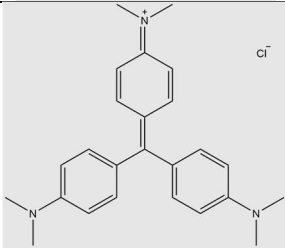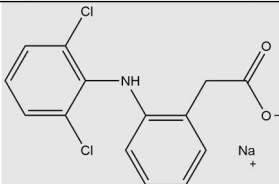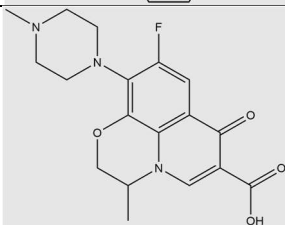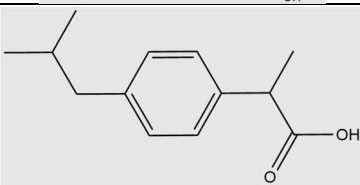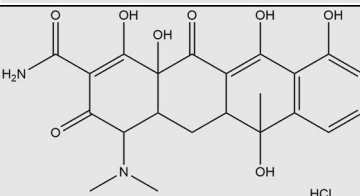
help understand which characteristics are most important for a carbon adsorbent when adsorbing any particular adsorbate. To this end, a series of activated carbon materials were produced using seven different activating agents in conjunction with the precursor histidine, which produced a series of amorphous carbon materials with a variety of unique properties. These porous carbons were next thoroughly evaluated using a variety of instrumental and wet-chemistry techniques to better understand their unique characteristics. Then, equilibrium and kinetic pollutant uptake studies were performed using eight different common environmental pollutants to investigate how different structural and chemical features impacted the adsorption of each adsorbate.

2.1 Chemical and textural analysis

2.1.1 Adsorbates

Adsorbates were selected based upon their prevalence in the environment, their various properties, and their prevalence in the literature to provide comparison to other works. A commonly applied feature when comparing aqueous adsorption is the Log K_{OW} of the adsorbates, which is a measurement (or computational estimation) of their preferential solubility in water or octane. A small or negative number implies a strong preference for a more polar environment, whereas larger values suggest nonpolar solutions are preferred. Chemical moieties should also be considered, though these can often only be abstractly considered as they can be difficult to individually quantify and compare. Varying

molecular weights from 206.3 to 653.2 g mol^{-1} is also a commonly considered parameter

and was likewise considered here.

Name: Methylene Blue Molecular Weight: 373.90 Est. Log K_{ow}: 0.75[45]	
Name: Methyl Orange Molecular Weight: 327.33 Est. Log K_{ow}: -0.66[45]	
Name: Methyl Green Molecular Weight: 653.2 Est. Log K_{ow}: -2.42[45]	
Name: Crystal Violet Molecular Weight: 408.2 Log K_{ow}: 0.51[46] Est. Log K_{ow}: 0.98[45]	
Name: Diclofenac Sodium Salt Molecular Weight: 318.13 Est. Log K_{ow}: 0.57[45]	
Name: Levofloxacin Molecular Weight: 361.37 Log K_{ow}: -0.39[47] Est. Log K_{ow}: -0.20[45]	
Name: Ibuprofen Molecular Weight: 206.29 Log K_{ow}: 3.97[48] Est. Log K_{ow}: 3.79[45]	
Name: Tetracycline Hydrochloride Molecular Weight: 480.90 Log K_{ow}: -1.37[47] Est. Log K_{ow}: -1.33[45]	

Table 2. Summary of data and structures for all eight adsorbates used in this study.

2.1.2 Textural properties

Gas adsorption analysis (GAA) using nitrogen at 77 K was used to determine the BET characteristic surface area, pore volume, and pore size distribution (PSD). The specific surface areas of our carbons ranged from $7.5 - 1300+$ cm^2 g^{-1} and the pore volumes ranged from $0.0077 - 0.6620$ cm^3 g^{-1}. These data are summarized in **Table 3**. Summary of GAA data for all activated carbons used in this study. All high surface area carbons were of type 1 and had fully reversible isotherms, apart from H_3PO_4-HAC which had a type I + IV isotherm and contained a non-symmetrical hysteresis loop (H2). This type of hysteresis can be indicative of disordered, non-uniform mesopores. Still, the quantity of mesopores found in this carbon are quite small. When K_2HPO_4 is used, significant surface area is not achieved. These carbon materials have a type II isotherm with very low total surface area. Thus, it appears that histidine-derived porous carbons most frequently produce microporous materials.
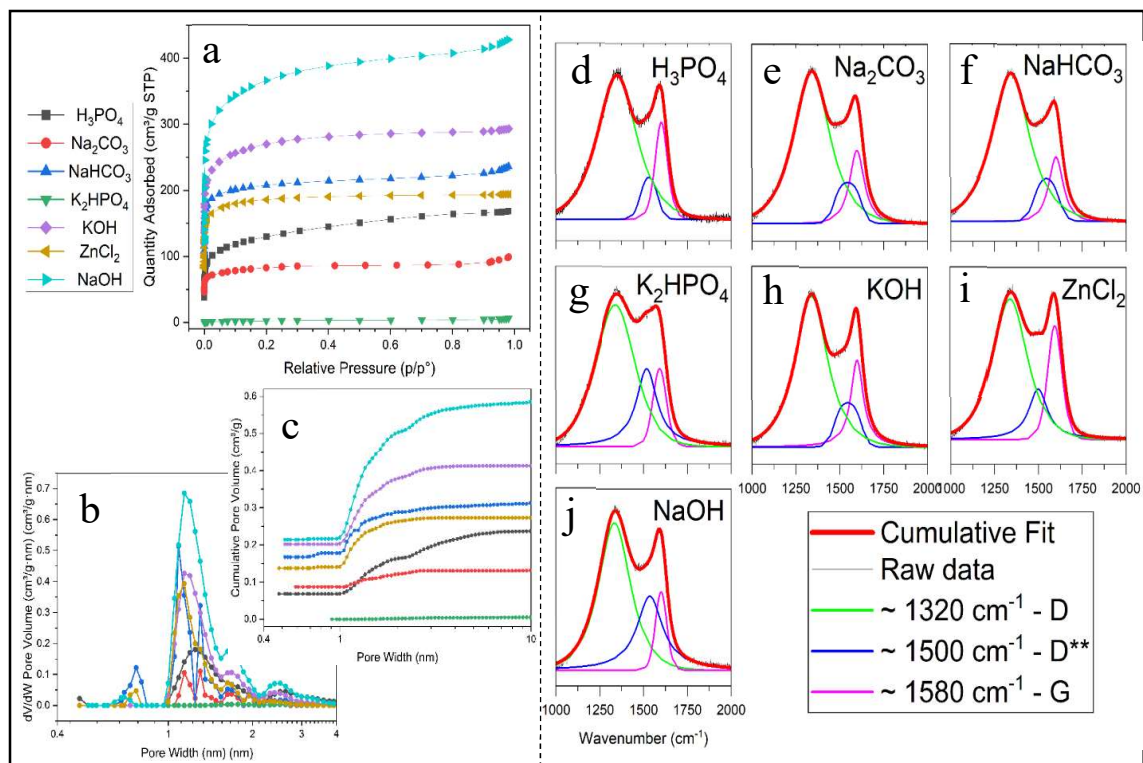
Figure 5. Textural analysis of the porous carbons used in this study including gas adsorption analysis, including N_2 isotherms at 77K (a) and dV/dW and cumulative pore size distribution plots (b and c) which reveal a diverse set of surface areas and pore volumes, as well as Raman analysis (d-j) focusing on the D and G bands, which suggest that all porous carbons are highly amorphous (I_D/I_G ranges from 1.50 – 3.58) with only small graphene lattices present throughout.

Beyond the summary properties, GAA can also provide some information regarding the pore size distribution (PSD) of these carbons. **Figure 5.** It seems that overall, most of the pore volume in our carbons occur in pores whose width is between 1-2 nm. Notably in the PSDs NaOH, KOH, NaHCO$_3$, ZnCl$_2$, and Na$_2$CO$_3$ ACs all have their largest peak around 1.2 nm and their second largest around 1.7 nm. The carbons activated with NaHCO$_3$, ZnCl$_2$, and NaOH, are the only carbons which have sub-nanometer pores, centered around 0.7-0.8 nm. Overall, there are strong similarities in the PSDs of all the

produced ACs, yet a few key differences in the magnitude and location of some pores in the PSD could result in the increased uptakes of various adsorbates.

It might be expected that similar activating agents would produce similar textural properties, however, this is not always the case. The two alkali-hydroxide activated carbons provided the largest surface areas, at $1,026.6 \pm 3.9$ and $1,369.8 \pm 4.0$ for KOH and NaOH ACs, respectively. Both ACs also contained the largest total- and micro-pore volume. Yet, this can be juxtaposed with to the two carbonates or the two phosphates, which produced drastically different surface areas in both cases. Histidine-derived carbons activated with sodium carbonate contained $310.0 \ cm^3 \ g^{-1}$, yet when activated with the slightly more acidic sodium bicarbonate, the surface area increases drastically, to $813.3 \ cm^3 \ g^{-1}$. However, the PSD of these two carbons is remarkably similar, each containing two distinct peaks around 1.1 and 1.3 nm. Overall, all carbons used had a good distribution of surface areas and pore volumes, which should provide good reference information for looking at trends in molecular uptake information.

Activating agent	Gas adsorption analysis					Raman analysis
	BET characteristic surface area	Total pore volume $P/P° \geq 0.98$	t-plot micropore volume	NLDFT micropore volume	BJH mesopore volume	I_D/I_G
	$m^2 \ g^{-1}$	$cm^3 \ g^{-1}$	$cm^3 \ g^{-1}$	$cm^3 \ g^{-1}$	$cm^3 \ g^{-1}$	
H_3PO_4	470.4	0.2600	0.1220	0.1640	0.58	3.18
Na_2CO_3	310.0	0.1530	0.1021	0.1172	-	2.77
$NaHCO_3$	813.3	0.3653	0.2834	0.2940	-	3.09
K_2HPO_4	7.5	0.0077	-	0.0018	-	1.77
KOH	1026.6	0.4533	0.3763	0.3788	-	2.18
$ZnCl_2$	723.3	0.3003	0.2595	0.2660	-	1.77
$NaOH$	1369.8	0.6620	0.4395	0.5022	-	1.50

Table 3. Summary of gas adsorption analysis and Raman data for all activated carbons used in this study

Raman spectroscopy on the porous carbons reveal obvious bands around 1320 cm^{-1} (D) and 1580 cm^{-1} (G), typically associated with disordered and ordered graphitic lattices, respectively.[5, 49] However, the inclusion of a third peak, loosely centered at ~1500 cm^{-1} (D**) produced the best peak fits. This third band is associated with finite graphite crystals, C-H vibrations, and amorphous carbon.[6, 50] Universally, the D band, had the largest intensity. G and D** bands were present in varying ratios, with $ZnCl_2$-HAC and H_3PO_4-HAC containing the most G to D** ratio. In order to assign typical I_D/I_G ratios, the G and D** bands are summed to determine I_G, as these can both be ascribed, at least partially, to graphitic character. Even with this assumption, all carbons have I_D/I_G ratios greater than 1, with only $ZnCl_2$-, NaOH-, and K_2HPO_4-HAC having values below two. Altogether, this suggests that the carbon materials produced in this study are primarily amorphous in nature, and to varying degrees.

As SEM imaging reveals, on a larger scale there are several types of carbons present, including those that are comprised of larger particles with semi-smooth faces ($ZnCl_2$-HAC, H_3PO_4-HAC, $NaHCO_3$-HAC), particles with very irregular shapes and semi-smooth faces (KOH-HAC, K_2HPO_4-HAC, NaOH-HAC), and particles with very rough textures (Na_2CO_3-HAC, NaOH-HAC). Frequently, the carbons have multiple types of structural features present, such as NaOH-HAC who has both smoother surfaces and rough completely irregular surfaces. On closer inspection, more variation can be seen between the porous carbons, and often within a single porous carbon sample. For example, although both H_3PO_4-HAC and $ZnCl_2$-HAC are comprised of larger geometric structures that appear semi-smooth, a closer inspection reveals that H_3PO_4-HAC have obvious texture on a micro-

meter scale that is not present in the ZnCl$_2$-HAC. KOH-HAC represent a middle ground between the highly smooth surfaces on ZnCl$_2$-HAC and the very rough H$_3$PO$_4$-HAC surfaces. Yet, it is worth noting here that H$_3$PO$_4$-, ZnCl$_2$-, and KOH-HACs had 470.4, 723.3, and 1,026.6 m^2 g^{-1} BET characteristic surface areas, respectively, which suggests that this level of texturing does not appear to be solely responsible for the carbon's SSA.

Carbons activated with NaOH and KOH exhibited some interesting similarities and some striking differences. Both KOH and NaOH activated carbons exhibited a 'swiss-cheese' like character. This character was prevalent throughout the entirety of the KOH activated sample, while co-existing with very textured particles in the NaOH-HAC samples. It is worth noting that in the NaOH-HAC structures, the more textured particles do have some embedded 'swiss-cheese' structures, so it could be that these larger backbone structures are formed inside the highly irregular textured structures and as the more textured structures are etched away, they leave behind the smoother structure underneath. It could be that further activation with NaOH will yield particles that appear completely akin to KOH activated particles, however, the product yield of NaOH-HAC is very low (much lower than any other carbon) and further activation by increasing the time, temperature, or activating agent mass ratio becomes rapidly impractical.

Comparing Na$_2$CO$_3$-HAC and NaHCO$_3$-HAC images shows two very different particle appearances. Na$_2$CO$_3$-HAC produced larger structures with leaf-like tatters. Holes of various sizes were scattered throughout all the particles, and a very slight sub-micrometer surface texture can be detected. This is exactly opposite for NaHCO$_3$-HAC, which on a larger scale seems to have smoother particle surfaces, but these entire particles are covered with dense, easily visible sub-micron pores.
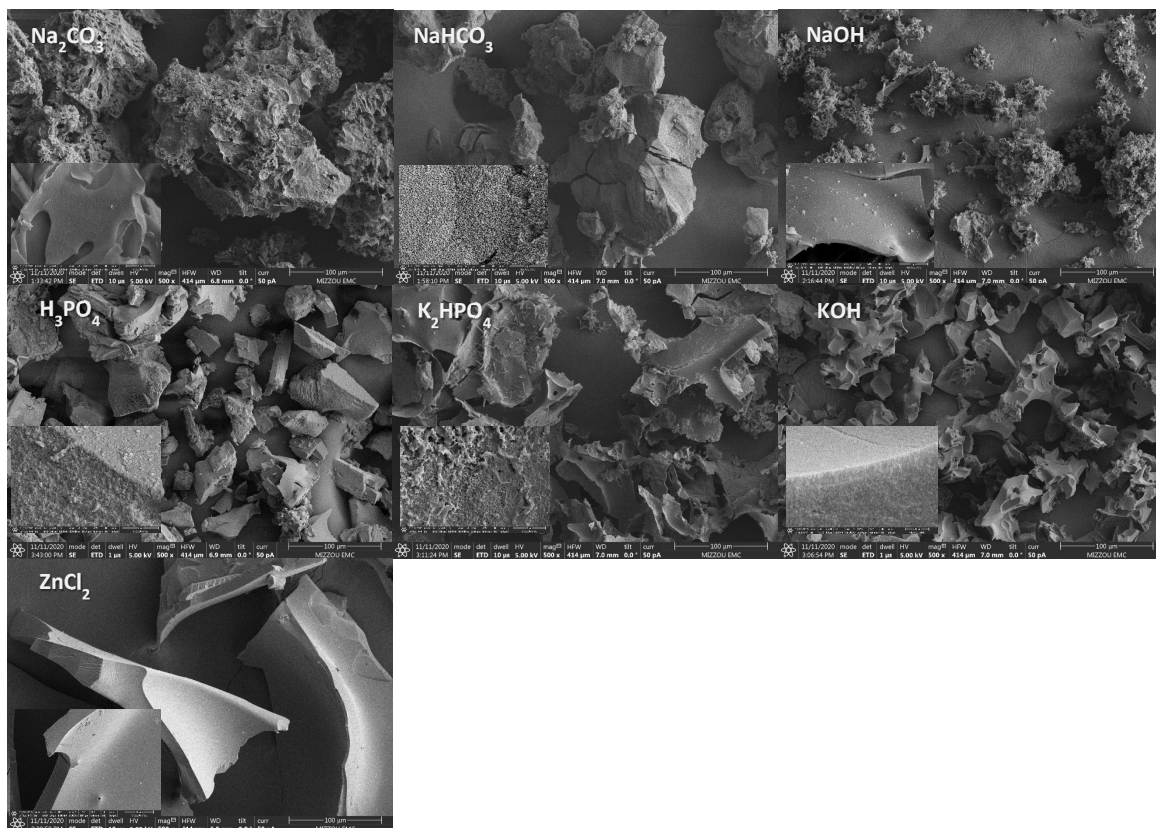
Figure 6. SEM micrographs of all seven histidine-derived activated carbons used in this study which reveal a good degree of morphological variety.

SEM imaging revealed a wide variety in the larger textural properties of these carbons. **Figure 6.** Many, such as NaOH-, KOH-, NaHCO$_3$-, ZnCl$_2$- and Na2CO$_3$-HACs, produced plate-like particles or features, often with irregular overall geometry. Not all carbons were uniform, such as the H$_3$PO$_4$-HACs, who had both three-dimensional particles of irregular geometry, but also contained "fluffy" looking particles. The K$_2$HPO$_4$ AC particles appear to be comprised of small, cubic crystalline shapes.

Looking closer, it appears that many of these carbons are comprised of sheets. This is indicated by the possible appearance of stacked layers along the edges of NaOH-, KOH-, Na$_2$CO$_3$-, NaHCO$_3$-, and possibly even H$_3$PO$_4$-HAC, though the overall irregularity of its

36

surface makes that hard to determine. Porous carbon produced with K_2HPO_4 also has rough edges, however, considering the low surface area of this carbon ($\sim$7 m^2 g^{-1}), if it is made up of discrete sheets, they are compressed far too tightly to permit access within the molecule.

Of the carbons that do appear to be at least partially comprised of sheets, there are several differences in textural properties that can be seen. One such example is the overall uniformity of the edges, which are often fairly smooth as seen with NaOH-, KOH-, and Na_2CO_3-HAC, but can be highly irregular as with $NaHCO_3$-HAC or H_3PO_4-HAC (again, if it is in fact comprised of sheets). The overall homogeneity of the sheets can also be considered. Although $NaHCO_3$ produced highly irregular edges, the carbon itself appears highly uniform. This is distinct from the KOH activated carbon, which is speckled with many irregularities, visible along the plane of the carbon surface. NaOH-HAC and Na_2CO_3-HAC represent a blend of these two particles with the NaOH-HAC appearing mostly smooth, similar to $NaHCO_3$-HAC, and the Na_2CO_3-HAC appearing to contain some faint irregular specks, though not as many or as strongly as KOH-HAC.
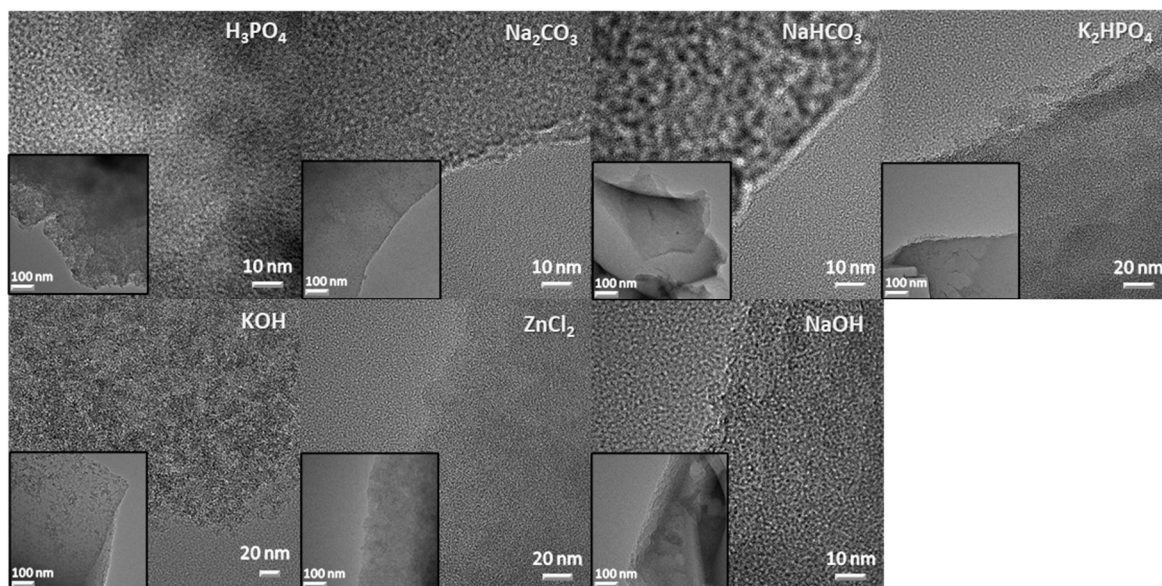
Figure 7. TEM micrographs of all seven histidine-derived activated carbons used in this study which suggest a principally amorphous organization and only occasional, small, scattered regions of order.

The carbons used in this study were further analyzed with TEM. **Figure 7.** This revealed some textural differences between the various carbons. For example, NaHCO$_3$-AC, NaOH-HAC, and K$_2$HPO$_4$-HAC all appeared with quite homogenous surfaces on a scale of hundreds of nanometers, whereas KOH-HAC and Na$_2$CO$_3$-HAC appear similarly homogenous but with the inclusion of impurities or imperfections scattered throughout the structure. On a similar scale, ZnCl$_2$-HAC appears to have a somewhat roughened texture (which is in contrast to its highly smooth surface in SEM imaging) and H$_3$PO$_4$-HAC has a very heterogenous texturing. But on the scale of tens of nanometers, H$_3$PO$_4$-, Na$_2$CO$_3$-, NaHCO$_3$-, and NaOH-HAC can be seen to have similar micro and small mesoporous structures, dispersed and randomly oriented throughout the carbon structure. KOH-HAC also appears to have a heterogenous microporous structure throughout its surface, but these appear markedly different from the structures on other carbons, such as NaOH-AC. K$_2$HPO$_4$-HAC expectedly does not have apparent features that might indicate significant

porosity. Unexpectedly ZnCl$_2$-HAC also showed no apparent microporosity, despite having a significant SSA of 723 m^2 g^{-1} and a PSD that indicates the presence of supermicropores.

2.1.3 Chemical properties

To evaluate active surface chemistry on the porous carbons a number of spectroscopic and analytical techniques were implemented. To begin, XPS was used to determine the atomic concentrations of the various carbons. **Figure 8.** It was determined that the majority of the produced carbons contain 70-78 % carbon, and 10-20 % nitrogen, and 6-15 % oxygen.

. This is a relatively high heteroatom concentration and is possibly due in part to both the moderate activating temperatures used in this study (650 °C) and the fact that both nitrogen and oxygen are initially embedded into the carbon structure of histidine, possibly making it more likely to remain embedded in the final carbon structures. This would contrast with using a nitrogen dopant, such as urea, to try and incorporate non-native nitrogen into the carbon structure.

H$_3$PO$_4$-HAC was in contrast, regarding the relative atomic abundancies, as it is over half oxygen (51.62 %) and contained 14.21 % phosphorous as well. One possibility is the presence of residual phosphates. Yet, if that is true, then they must be embedded into the overall structure, since excessive rinsing after activation was not able to remove them. The relative concentration of carbon was about a third of the other carbons, being 26.14 %. It

contained only 2.34 % nitrogen. Above all, this suggests that the average chemical signature of H_3PO_4-HAC was significantly different than that of the other carbons.
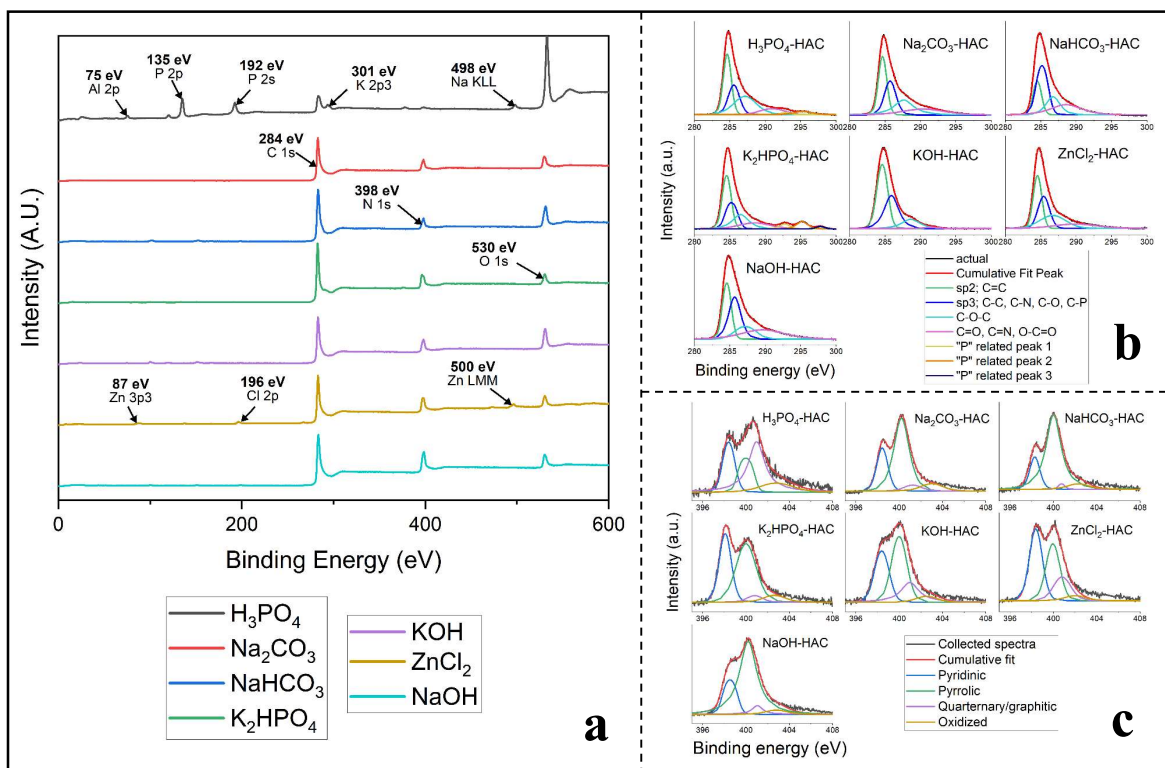
Figure 8. Annotated XPS surveys for all seven histidine-derived activated carbons used in this study (a) revealing all structures are primarily composed of carbon, nitrogen, and oxygen, with occasional alternate species following the nature of the activating agent. Additionally, fitted C1s (b) and N1s (c) fine scans are shown revealing variation (or lack of) in the nature of the species.

Carbon, nitrogen, and oxygen were the primary components of all but H_3PO_4-HAC. K_2HPO_4-HAC also contained some residual phosphorous (0.43 %), though this carbon did not incorporate phosphorous into the structure to the extent H_3PO_4-HAC did. $ZnCl_2$-HAC also contained traces of its activating agent, with 0.73 % of the carbon structure being Zinc. Chlorine was also only detected in the $ZnCl_2$-HAC sample (0.93 %), despite the histidine precursor containing HCl. The only instance where significant quantities of impurities were detected was in the instance of H_3PO_4-HAC, which contained sodium and aluminum (1.8 and 3.9 %, respectively). The only likely source of aluminum are the ceramic boats used

in this study, which could have been etched by the phosphoric acid and heat during the activation process.

Fine scan analysis of C1s, N1s, and O1s peaks was also undertaken **Figure 8b, c.** For C1s analysis, peak fitting suggested four primary peaks around 284.5 (1), 285.7 (2), 287 (3), and 289 (4), which typically correlate to C=C (1), C-C, -N, -O, -P (2), C-O-C (3), and C=O, =N, or O-C=O (4) functional groups. Additional phosphorous-related groups can be seen in both H_3PO_4-HAC and K_2HPO_4-HAC, though these are small in quantity. A mixture of sp^2 and sp^3 hybridized bonds were the primary components in all of the carbons, together comprising of 67.9 – 90.4% of the total carbon. **Table 4**. They all also contained a significant quantity of carbons related to ether linkages, ranging from 8.6 -17.2 %. There were not typically large quantities of C=O, =N, or carboxylic groups present, which is surprising given the quantity of carboxylic groups determined via modified Boehm titrations. It is possible that the bulk of these groups are housed internally in the amorphous structure and therefore might be harder to detect using XPS analysis. Still, this peak correlates to 14.8% of $ZnCl_2$-HAC's carbon content, the largest among the set of carbons, and $ZnCl_2$-HAC also contained the largest quantity of carboxylic groups.

C1s fine scan (%)							
	284.5	285.7	287	289	292.8	295.2	297.7
Carbon	C=C	C-C,N,O,P	C-O-C	C=O,N or O-C=O	P_1	P_2	P_3
H_3PO_4-HAC	50.8	24.8	15.4	4.9	1.6	2.6	0.0
Na_2CO_3-HAC	51.7	30.0	13.2	5.2	0.0	0.0	0.0
$NaHCO_3$-HAC	30.3	44.2	16.4	9.2	0.0	0.0	0.0
K_2HPO_4-HAC	46.5	22.9	12.4	5.3	4.4	6.3	2.2
KOH-HAC	59.6	30.8	8.6	1.1	0.0	0.0	0.0

ZnCl$_2$-HAC	37.4	30.6	17.2	14.8	0.0	0.0	0.0
NaOH-HAC	46.8	35.0	10.5	7.7	0.0	0.0	0.0

Table 4. C1s peak fitting data for histidine-derived activated carbons in this study that show principally sp^2 and sp^3 carbons present, with a variety of others.

N1s fine scan (%)				
Carbon	398.4 Pyridinic	400 Pyrrolic	401 Graphitic	402.8 Oxidized
H$_3$PO$_4$-HAC	34.9	23.7	35.2	6.2
Na$_2$CO$_3$-HAC	33.3	56.5	4.6	5.6
NaHCO$_3$-HAC	27.4	63.5	4.5	4.5
K$_2$HPO$_4$-HAC	49.0	41.7	4.6	4.8
KOH-HAC	36.0	46.0	13.9	4.2
ZnCl$_2$-HAC	45.5	36.2	15.1	3.1
NaOH-HAC	28.7	60.6	7.2	3.5

Table 5. N1s peak fitting data for histidine-derived activated carbons in this study that show pyridinic and pyrrolic constitute most of the nitrogen, with both graphitic and oxidized also being present.

O1s fine scan (%)			
Carbon	531 O=C, P	532.5 O-H, C, N, C-O-C	534.8 O-C=O
H$_3$PO$_4$-HAC	15.7	44.3	40.0
Na$_2$CO$_3$-HAC	42.8	48.6	8.5
NaHCO$_3$-HAC	22.2	70.6	7.2
K$_2$HPO$_4$-HAC	5.9	73.7	20.4
KOH-HAC	1.7	95.1	3.2
ZnCl$_2$-HAC	26.7	55.1	18.2
NaOH-HAC	35.4	59.2	5.4

Table 6. O1s peak fitting data for histidine-derived activated carbons used in this study which shows a wide variety of oxygen functional groups present, varying with the activating agent used.

Peak fitting the N1s analysis revealed the four typical nitrogen peaks found in porous carbon materials. **Figure 4.b**. These are pyridinic (1), pyrrolic (2), graphitic or quaternary (3), and oxidized (4), which correlated to eV values around 398.4 (1), 400 (2), 401 (3), and 402.8 (4), respectively. Overall, pyridinic and pyrrolic nitrogen comprised between 81.7 and 90.9% of the overall nitrogen content, except for H_3PO_4-HAC, whose nitrogen content contained approximately 35.2% graphitized nitrogen. **Table 5**. KOH- and $ZnCl_2$-HACs also contained 13.9 and 15.1% graphitic nitrogen, respectively, significantly higher than the remaining carbons (4.5 – 7.2%). The graphitic nitrogen content correlated well with the Raman G-band, suggesting that the graphitized nitrogen is influenced by the overall graphitic character of the carbon. Oxidized nitrogen appears to have been present in low concentrations ($\leq 6.2\%$), regardless of the sample.

Boehm titrations and pH of zero charge (pH_{pzc}) can be very informative when probing active surface chemistry in aqueous solution.[51-53] Still, it should be noted that Boehm titrations are intended to account for oxygen- and carbon-based functional groups and does not consider the possibility of nitrogen functional groups or address other heteroatoms. Still, Boehm titrations indicated a good variety of active surface functional groups on the carbons. **Table 3**. The ratio of these groups varies from carbon to carbon, but in all instances where a significant quantity of surface functional groups was found, phenols were always the most prevalent, even if only by a little.

2.2 Pollutant Adsorption Studies

2.2.1 Equilibrium studies

All dye and pharmaceutical capture capacities were determined for the seven carbons by producing isotherms and collecting data until the capacity leveled off. Figure 9. Given our method, the data collected for ibuprofen resulted in an incomplete isotherm due to the very low solubility of ibuprofen. Yet for the other 49 adsorbate-adsorbent datasets, this 'levelling off' was achieved.
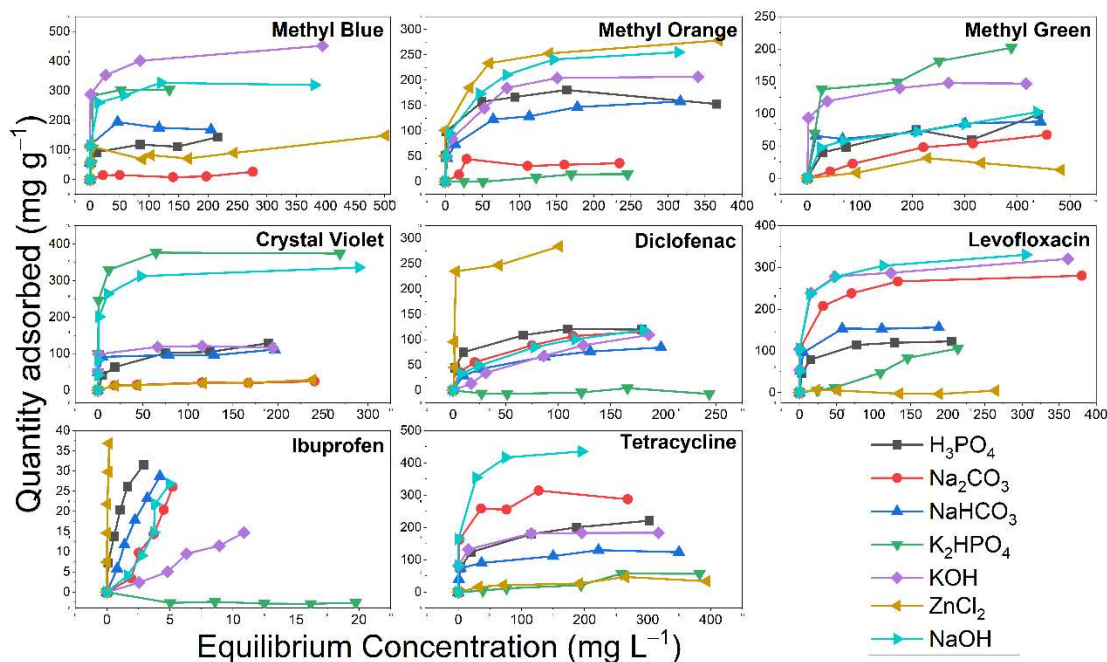
Figure 9. Equilibrium isotherms obtained in this study at 25 °C, sorted by adsorbate. Full isotherms were observed with a plateau for each adsorbate-adsorbent pair, except for isotherms of ibuprofen, which reached the solubility limit given the experimental parameters. To see these sorted by adsorbent, refer to **Figure S2.**

Immediately, we can begin to see that variations in the carbons textural and chemical properties drastically effect these carbon's abilities to capture different adsorbates. **Table 7.** Furthermore, there does not appear to be an immediate and clear association with any aspects of the carbons or adsorbates that justifies these trends. For example, carbons activated by NaOH and KOH have the best SSA, yet only sometimes are they the top capturing carbons. Carbons activated with $ZnCl_2$ and K_2HPO_4 were often

44

either the best at capturing any particular adsorbate or the worst, and sometimes but not always did their rank coincide with one another. Clearly, there is no universal trend that can be readily determined when considering all the isotherms together.

Capture Capacities (mg g^{-1})								
	Methyl Blue	Methyl Orange	Methyl Green	Crystal Violet	Diclo-fenac	Levo-floxacin	Ibu-profen	Tetra-cycline
H$_3$PO$_4$-HAC	143.5	180.8	98.8	128.5	121.2	123.0	31.6	221.1
Na$_2$CO$_3$-HAC	26.4	36.3	67.2	24.1	116.2	280.1	26.1	314.3
NaHCO$_3$-HAC	194.0	158.1	87.5	111.7	84.8	156.3	28.7	130.0
K$_2$HPO$_4$-HAC	303.8	14.7	202.1	376.1	4.3	105.7	-2.6	57.3
KOH-HAC	452.3	206.8	147.3	121.4	109.3	320.5	14.8	183.7
ZnCl$_2$-HAC	148.5	278.4	31.2	28.5	284.1	4.8	36.8	46.7
NaOH-HAC	327.0	255.1	102.5	335.5	119.2	330.4	26.8	435.5

Table 7. Reported maximum capture capacities for all eight adsorbates onto all seven histidine activated carbons.

In an attempt to find clear trends on a case-by-case basis, the maximum capture capacities for all 56 adsorbate-adsorbent combinations were correlated with the quantifiable aspects of the carbons and adsorbates. **Table 8**. When organized, it begins to become clear that every adsorbate preferentially sorbs based upon different features of the carbons. For example, surface pH of the carbon most heavily impacted methyl green's ability to be adsorbed, whereas features such as SSA and pore volume did not correlate well. This is exactly opposite for the uptake of methyl orange, which appears to be best correlated with SSA and pore volumes.

Table of Coefficient of Determinations (R^2)

		Data set							
		Methyl Blue	Methyl Orange	Methyl Green	Crystal Violet	Diclo-fenac	Levo-floxacin	Ibu-profen**	Tetra-cycline
Gas adsorption analysis	SSA	0.21, 0.68*	0.66	0.08	0.00, 0.65*	0.11	0.24	0.18	0.25
	TPV	0.19, 0.63*	0.62	0.07	0.00, 0.80*	0.08	0.28	0.18	0.33
	t-plot MiPV	0.25, 0.73*	0.64	0.07	0.00, 0.48*	0.13	0.23	0.15	0.17
	NLDFT MiPV	0.21, 0.68*	0.65	0.08	0.00, 0.64*	0.12	0.25	0.18	0.25
Raman	I_D/I_G	0.26	0.07, 0.45*	0.05	0.29	0.02	0.00	0.11	0.00
pH$_{pzc}$		0.20	0.40, 0.04*	0.81	0.68, 0.42*	0.65	0.04, 0.97*	0.89, 0.59*	0.00, 0.68*
Boehm Titrations	Carboxyls	0.05	0.39, 0.10*	0.64	0.58, 0.29*	0.82	0.01, 0.19*	0.49, 0.06*	0.00, 0.33*
	Lactones	0.00	0.00, 0.32*	0.05	0.29, 0.05*	0.00	0.34	0.05, 0.57*	0.06
	Phenols	0.01	0.37, 0.03*	0.47	0.39, 0.02*	0.44	0.13	0.41, 0.09*	0.10
	Sum groups	0.01	0.27, 0.00*	0.45	0.52, 0.15*	0.39	0.11	0.38, 0.14*	0.05
XPS - atomic concentration (%)	C	0.04	0.04	0.01	0.02	0.01	0.04	0.11	0.01
	N	0.07	0.02	0.00	0.10	0.04	0.03	0.03	0.01
	O	0.06	0.01	0.01	0.04	0.00	0.03	0.11	0.01
XPS - N	Pyridinic	0.00	0.05	0.10	0.03	0.01, 0.79*	0.39	0.21	0.49
	Pyrrolic	0.01	0.01	0.00	0.01	0.06	0.33	0.00	0.18
	Graphitic	0.01	0.14	0.03	0.06	0.09	0.08	0.14	0.00
	Oxidized	0.21	0.38, 0.55*	0.03	0.02	0.21	0.00	0.01	0.01
XPS - O	O=C,P	0.44	0.00	0.51	0.08	0.13	0.03	0.36	0.33
	O-H,C,N, C-O-C	0.70	0.00	0.37	0.06	0.13	0.09	0.36, 0.60*	0.09
	O-C=O	0.13	0.00	0.00	0.00	0.00	0.38	0.01	0.08
XPS - C	C=C	0.12	0.03	0.16, 0.37*	0.01	0.05	0.33	0.13	0.14
	C-C,N,O,P	0.00	0.12	0.16, 0.00*	0.05	0.01	0.05	0.18	0.03
	C-O-C	0.54	0.01	0.36, 0.62*	0.21	0.19	0.67, 0.82*	0.31, 0.77*	0.22
	C=O,N or O-C=O	0.17	0.19	0.44, 0.74*	0.05	0.46	0.42	0.32, 0.71*	0.09
		Data set							
		H₃PO₄	Na₂CO₃	NaHCO₃	H₃PO₄	KOH	ZnCl₂	H₃PO₄	
Adsorbate properties	M.W.	0.39	0.36	0.08	0.08	0.02	0.14	0.36	
	K_{ow}	0.40	0.16	0.19	0.03	0.09	0.00	0.17	
	Charge	0.05	0.05	0.00	0.57	0.03	0.41	0.00	

Table 8. Summary of the R^2 values produced by correlating the found maximum capture capacities with various quantitative-determined properties of the histidine-derived porous carbons and adsorbates used in this study. *Significant correlation changes for when the K₂HPO₄ dataset is excluded are shown here. **Ibuprofen did not produce a full isotherm.

However, before further discussion, it is important to discuss the impact of K_2HPO_4-HAC on these residuals. This carbon has a few features that give it the ability single-handedly skew the correlation of a dataset, such as virtually no SSA (or pore volume) and a markedly different surface pH. The dataset used here is relatively small, thus even if the K_2HPO_4-HAC is truly a unique outlier, then its inclusion will inevitably hide or produce fallacious correlations. For example, MB has no strong correlation with any textural carbon feature while including the K_2HPO_4-HAC dataset, yet when this potential artifact is excluded, a good correlation can be found between the carbon's uptake of MB and its SSA. This will be kept in mind throughout the remainder of the discussion.

Overall, the textural properties of the carbons, such as their SSA and PVs and degree of graphitization, correlated much less strongly than anticipated. Methyl orange was the only adsorbate whose adsorption was found to be best correlated with increased surface area and pore volume, though both methyl blue and crystal violet were found to also correlate well upon the exclusion of K_2HPO_4-HAC. It was also noticed that no significant differentiation was found between the SSA, total pore volume, or micropore volume, as these correlations all tend to be closely grouped together. Raman analysis was largely found to be uncorrelated throughout all the carbons.

Interestingly, the relative atomic concentrations produced no correlations the capture capacities of the carbons, whereas specific peaks associated with certain functional groups occasionally produced good correlations. A great example of this is when considering the adsorption of MB on the entire dataset, which produced virtually no good correlation except when considering peaks associated with ethers in O1s or C1s analysis. This correlation might also be associated with phenolic groups as well, yet Boehm titrations

suggest that phenols do not strongly correlate with the uptake of methyl blue. This might therefore suggest a partial link between the uptake of methyl blue and the abundance of ether groups throughout the carbons.

Surprisingly, the correlation between the adsorption of Levofloxacin and the presence of C-O-C peaks in the C1s analysis was also found to be either good or very good, depending on inclusion of K_2HPO_4-HAC related data.

The adsorption of both MG and Diclofenac can be correlated by the presence of carboxyl groups when considering data collected from Boehm titration and C1s analysis. Yet, O1s analysis in both instances suggests that there is virtually no relationship between the presence of carboxyls and the uptake of these two adsorbates.

Still, some of the strongest correlations come from the analysis of the pH_{pzc}, which relates to the surface pH of the carbons. With K_2HPO_4-HAC having such a different pH_{pzc} than the other carbons, it's influence as an outlier was very strong. Even so, MG and ibuprofen had strong positive and negative correlations, respectively. Upon the exclusion of K_2HPO_4-HAC, levofloxacin has a very strong positive correlation ($R^2 = 0.97$) with pH_{pzc}.

Finally, a critical finding in this study is the lack of dependency on any single aspect of the porous carbons. Rather, there is a uniqueness to each adsorbate-adsorbent interaction that leads to the erratic variation in the capture capacities from one carbon to another. Thus, it does not appear to be a viable strategy to simply produce and universally apply the carbonaceous materials with the largest SSA, PV, nitrogen content, etc. Instead, a broader approach could be applied to first determine which aspects are most important for any

particular adsorbent-adsorbate interactions. Altogether, this suggests that despite the promise of porous carbon materials for pollutant capture in an aqueous medium, investigation on a case-by-case basis might be necessary to achieve desired functionality.

The trials were also fitted using several isotherm models. **Figure S3**. Though there are a large number of data sets and many exceptions, broadly it was observed that the Freundlich isotherm often fit well and the Langmuir isotherm model did not. **Tables S1 and S2.** Even when the Langmuir isotherm model fit well, it was usually the case that the Freundlich isotherm model fit better. Overall, this might suggest that the adsorption process occurred heterogeneously across the surface of the carbons, possibly influenced by active sites or scattered microporosity, rather than homogenously and smoothly across the surface of the carbons. This is important as it suggests that the inclusion of large quantities of heteroatoms and functional groups is critical to the effectiveness of a carbon sorbent.

Still, there are a decent number of exceptions, such as the adsorption of levofloxacin on $NaHCO_3$-HAC, which favored the Langmuir model in the given dataset. In fact, several isotherms involving $NaHCO_3$-HAC were fit better by the Langmuir isotherm model. Though the Freundlich isotherm model is more frequently the better fitting model, the lack of uniformity throughout the modelling can be seen as a further indication of the uniqueness between the interactions of each adsorbate-adsorbent pair.

The Sips isotherm model, which combines the Langmuir and Freundlich models, and the Toth isotherm model, which is an empirically adjusted version of the Langmuir model designed to account for more heterogenous systems over a wider concentration range, were also used to try and model the collected data. Frequently, both fits were like each other and comparable to the Freundlich isotherm model on its own.

Of course, it should be noted that with the wide scope of this project (and COVID restrictions occurring during the data collection phase) a large quantity of data was not able to be collected for each of the 56 adsorbate-carbon combinations. Thus, although many correlations can be suggested, there is a somewhat tenuous nature to the isotherm modelling presented here.

2.2.2 Kinetic studies

Kinetic studies are often useful, as they can sometimes give insight into the adsorption process itself. This kinetic information was modelled using four common models for liquid-solid adsorption systems. **Figure 10**. Broadly, the pseudo second order model (PSO) frequently produced good fits with the kinetic data and almost without exception produced better fits than the pseudo first order model (PFO). **Tables S3 and S4**. This could be a result of the low concentration ranges that were used, which are suggested to be better represented by the PSO.[54] Despite their frequent application in such studies, it is difficult to draw conclusive physical meanings from a good fit with either the PSO or PFO. Thus, although much of our data can be modelled well using the prior two models, little else can be definitively said. Still, it is possible that the part of the good agreement with the PSO broadly across the carbons is a result of well dispersed and abundant active sites.
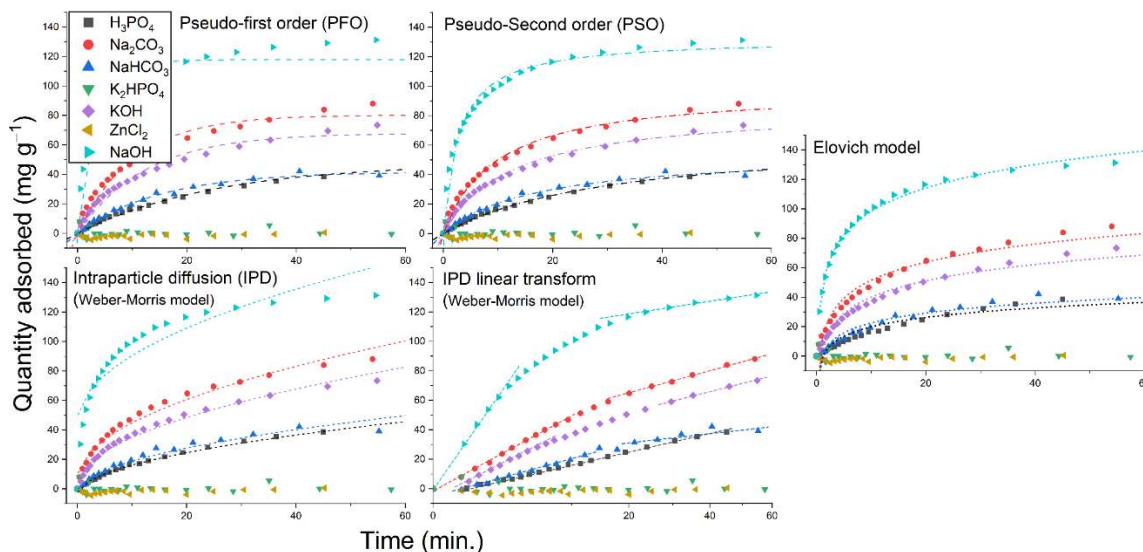
Figure 10. An example of data fitting for all four kinetic models used in this analysis, showing different models produce better fits, depending on the carbon. (Adsorbate: tetracycline)

Perhaps more usefully, the Elovich model also frequently produced good fits across all the carbon-adsorbate combinations. This model assumes that activation energy increases with time and heterogenous active sites, thus a good fit can be attributed to the adsorption process occurring at scattered active sites, rather than homogenously across the surface. This fits in line with the general heterogeneity and plethora of functional groups present in our activated carbons.

The intraparticle diffusion model (IPD) is intended to help identify several stages of the adsorption process and does not generally produce fits across the entire adsorption process. **Figure S5.** When the kinetic data is replotted accordingly (q_t vs $\sqrt{t}$), it can quickly be seen that the stages of adsorption are not constant from carbon to carbon, but some trends can be identified when looking at how each carbon adsorbs each adsorbate. For example, Na_2CO_3-, $NaHCO_3$-, and KOH-HAC all have only one easily discernable linear region. Closer inspection tends to reveal multiple linear regions, but with a small inflection

51

point. This might suggest that only one mechanism is responsible for the rate of adsorption throughout most of the adsorption process for these carbons, regardless of the adsorbate. This is opposed to the NaOH-HAC and K_2HPO_4-HAC, which tend to have multiple obvious linear regions. This suggests that the adsorption process goes through several rate-limiting mechanisms. In most instances the initial linear region (or entire if only one region) goes through the origin (0, 0), which suggests that intraparticle diffusion is the rate limiting step for the first period of the adsorption process (typically < 10 min.). Notable exceptions to this are the adsorption of diclofenac onto $ZnCl_2$-HAC, MG onto KOH-, H_3PO_4- and $NaHCO_3$-HACs, and CV onto H_3PO_4-HAC.

2.3 Conclusions

In this work, a series of diverse but linked porous carbons were produced from a simple precursor and seven different activating agents. Furthermore, these carbons were used as adsorbents for a diverse set of common aqueous pollutants. The primary conclusions from this work are as follows: 1. A diverse (in both form and function) set of porous carbons can be produced from a simple, small molecular weight precursor. 2. A resultant carbon could be selected from this set that is capable of adsorbing significant quantities of pollutant, even at low concentrations. 3. No single feature of the porous carbons could be universally linked to better adsorption across the entire range of adsorbates. Rather, the data collected here suggests that adsorption should be considered on an adsorbate-to-adsorbate basis, to produce the most efficient capture capacities and

rates. 4. For most of the adsorption processes, the initial rate-limiting step (the first < 10 min.) appears to be intraparticle diffusion into the amorphous framework.

The implications of the third conclusion are that the adsorption process of dyes and pharmaceuticals is complex. In a more realistic system where a wide variety of pollutants might have to be scrubbed from the water, a variety of carbons might have to be implemented to successfully purify the water. Furthermore, the most prevalent adsorbates should be screened individually first to best determine which carbons and features are most impactful in removing them from aqueous media.

2.4 Materials and Methods

Materials

All materials were used as purchased without further purification or alteration. L-Histidine HCl monohydrate (≥ 99%), potassium hydroxide, sodium hydroxide (≥99.8%), anhydrous $ZnCl_2$ (≥98%), concentrated o-phosphoric acid, sodium carbonate anhydrous, sodium bicarbonate, methylene blue trihydrate, methyl orange, and crystal violet were all purchased through Fisher scientific (Fair Lawn, NJ). Methyl green was purchased from Sigma (St. Louis, MO). Diclofenac sodium salt, levofloxacin, 2-(4-Isobutylphenyl) propionic acid, and tetracycline hydrochloride were all purchased from TCI chemicals (all are ≥98.0%) and used as purchased.

2.4.1 Preparation of activated carbons

In order to limit the scope of this study to a manageable body of work, a single activation temperature was selected. A temperature hot enough for all reagent combinations to have undergone pyrolysis is desired. A temperature where no significant mass loss is occurring was also desired, to maximize reproducibility. This was determined using thermogravimetric analysis (Q50, TA instruments) under nitrogen, shown in Figure S1. Synthesis analysis was performed by combining precursors in the same manner as during regular synthesis, then around 5-15 mg of the mixture is placed on a clean, tared pan for analysis. Analysis was performed under nitrogen at 65 mL min^{-1} and all ramping rates were 10 °C min^{-1}. The procedure then consisted of heating to 100 °C for 1 hour, then ramping to 650 °C and holding the temperature for 2 hours. It is worth noting that the internal temperature of this oven may differ from the internal temperature of the tube furnace used during synthesis, due to differences in the structure of the furnace and relative positioning of the thermocouples.

Thermogravimetric analysis (TGA) was also performed, testing the synthesis. **Figure 11**. The synthesis analysis here was used to determine the activation temperature used during this study, but. Activation in porous carbon materials tends to be a unique process for every combination of precursor, activating agent, temperature, etc. In order to reproduce consistent samples from a large variety of activating agents, some compromises were necessarily made. A consistent temperature hot enough for strong porosity to have developed, but where all the carbons are not still undergoing mass loss was sought. This is intended as a means to maximize reproducibility for the synthesis and partly to ensure full activation at the temperature selected. After around 500 °C all carbons except H_3PO_4 activated histidine have slowed or levelled off mass loss. [This may or may not be

consistent with our previous studies, depending on if they have been published, which have shown that low temperature activation is effective for producing certain highly activated histidine-derived carbons]. Around 650 °C, histidine activated with H_3PO_4 has just finished a significant mass loss from 65% to 20% and begins to slow its decomposition. Based upon the dTGA data, 650 °C was chosen as the activation temperature.

This decomposition data may be useful for future studies, revealing possible optimal temperatures for individual carbons. This is because we can look at approximate temperatures where the activation process might occur, signified by significant loss of mass or even a slight increase in mass. For example, $NaHCO_3$ activated histidine has a mass increase around 800 °C that could suggest high pore development at such temperatures.
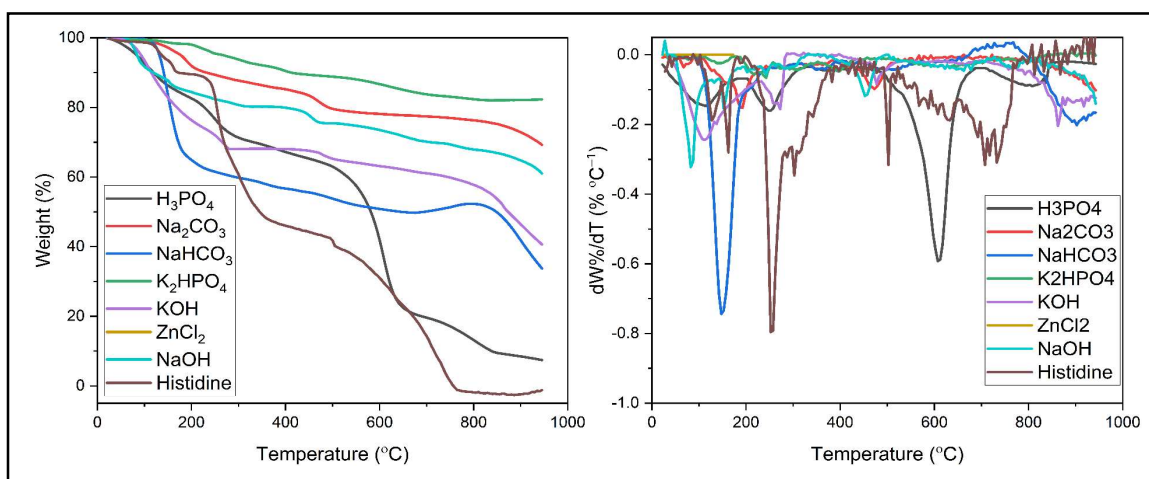
Figure 11. TGA (a) and dTGA (b) for the seven carbon precursor mixtures in this study and L-histidine alone.

All ACs in this study were prepared from the precursor L-histidine HCl with an activating agent (AA) in a 1:7 (His:AA) molar ratio. Activating conditions and ratios were

selected based upon previous studies, preliminary analysis, and the need to keep some simplicity in this study. Activating agents used in this study include KOH, NaOH, H_3PO_4, Na_2CO_3, $NaHCO_3$, K_2HPO_4, and $ZnCl_2$. The tube furnace used for AC synthesis was an across international STF1200 with a 4 in. ceramic tube. The synthesis procedure begins by grinding carefully measured amounts of precursors using a mortar and pestle until homogenous. Next the mixture was transferred to a ceramic boat, placed at the center of the furnace tube and sealed in. The heating process consisted of heating to 100 °C for one hour, followed by ramping to 650 °C and holding that temperature for two hours. The ramping rate was 10 °C min^{-1} and the nitrogen flow rate set to 100 mL min^{-1}. Activated materials were then allowed to cool naturally and were preliminarily rinsed with around 500 mL of ultrapure water before being added to 1 L of 0.1 M HCl solution (except for H_3PO_4 activated His which was added to 0.1 M NaOH) and stirred for 24 hours. Next, samples were filtered and rinsed with ultrapure water until the eluent reached neutral pH. The samples were then dried at 100 °C for ≥ 12 hours prior to characterization or use. Carbons produced in this study were named according to the following scheme: [activating agent]-HAC (e.g., NaOH-HAC).

2.4.2 Physiochemical characterization

Considering the mission of this research, characterization of the carbons employed several techniques in order to ascertain which structural and/or chemical features have the best correlation to uptake.

Gas adsorption analysis (ASAP 2020, Micromeritics) with nitrogen (airgas, >99.999%) at 77 K was used to define total surface area and pore volume, as well as probe the pore structure. All resulting data was analyzed using Micromeritics ASAP 2020 Plus software, version 2.00. The single point total pore volume was determined at relative pressures of ≥ 0.985 P/P°. Brunauer-Emmett-teller (BET) theory was used in conjunction with a Rouquerol BET plot to determine the total surface area of the carbons. The t-plot method, using the carbon black STSA statistical thickness equation, was used to determine micropore volume. NLDFT using N_2 at 77 K on carbon black slit pores was used to determine micropore size and pore volumes.

Raman analysis was performed using a Renishaw inVia Raman microscope with a 614 nm excitation source. Peaks were fitted using the Gaussian-Lorentzian Cross Product Function. Scanning electron microscopy (SEM) was performed on a Scios Analytical Dualbeam. Transmission electron microscopy (TEM) was performed using a FEI Tecnai F30 Twin 300kV TEM. A Formvar/Carbon 400 mesh, Copper was used as the support for analysis. Elemental analysis was performed using X-ray photoelectron spectroscopy (XPS) with a Physical Electronics 5000 VersaProbe II Scanning ESCA Microprobe. Infrared spectroscopy was performed on a Nicolet Summit PRO FTIR spectrometer (thermoscientific).

The pH at zero charge (pH_{pzc}) was determined based on literature precedent.[55-57] The process consisted of first adjusting ultrapure water to a series of different pH's (2, 3, 4, 6, 8, and 10) using stock NaOH and HCl solutions, followed by pipetting 20 mL of each solution into a series of small scintillation vials. The initial pH of each vial was then taken and subsequently 10 mg of AC was added. The suspension was then stirred for 24 hours

before the pH was again tested. The pH_{pzc}, is the pH at which point $pH_i - pH_f = 0$. Plotted

initial pH versus final pH, this where the series crosses the line y = x. **Figure 12.**
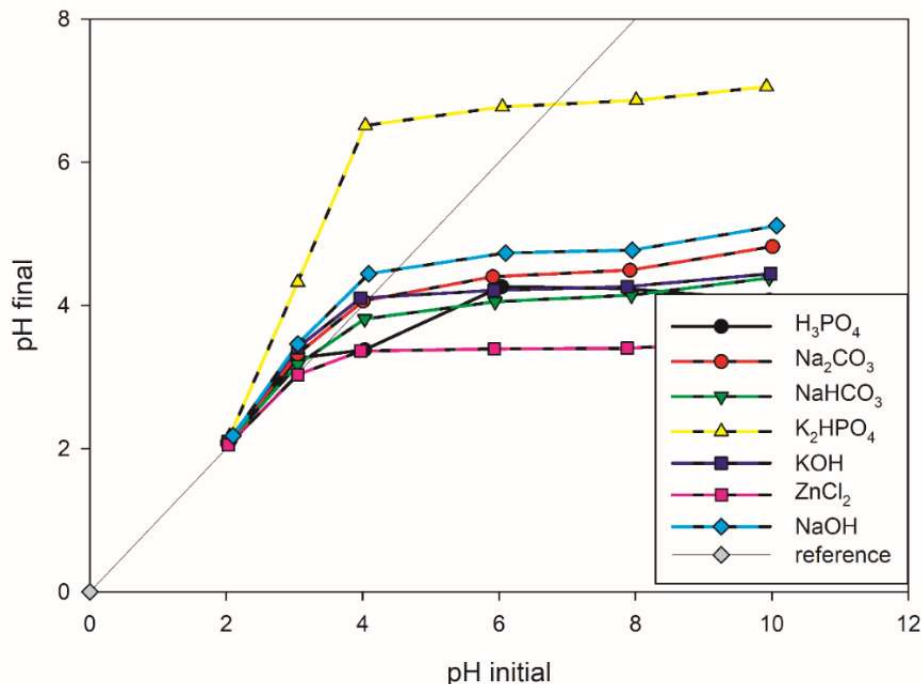
Figure 12. pH_{pzc} plot used for determining the average surface pH for the seven histidine-derived activated carbons used in this study.

Boehm titrations were completed, following the recently revised procedural

recommendations by Schönherr et al.[51] Broadly, 40 mg of each carbon was introduced to

separate 40 mL solutions of Na_2CO_3, $NaHCO_3$, and NaOH (all 0.01 N), then allowed to

react for one day on a mixing table, after which point it is assumed that at least 99+% of

the acidic surface oxygen functional groups will have reacted, if the respective base was

strong enough to deprotonate them. The supernatant was then decanted and 10 mL of it

was combined with 20 mL of 0.01 M HCl solution. Finally, a pH-based back-titration was

performed on the HCl solution using Na_2CO_3 as the titrant.

2.4.3 24-hour adsorption equilibrium studies

The total adsorption capacity for pharmaceuticals and dyes varies with the concentration of the adsorbate. All trials occurred in fresh 50 mL centrifuge vials, used 10 mg of carbon, and were shaken for 24 hours on an Excella E25 shaker table at 100 rpm. In order to vary the concentration used in each trial, a stock solution of each adsorbate was made and then placed in a clean, sealed, foil-wrapped bottle. Ultrapure water and stock solutions of adsorbate were then pipetted in appropriate ratios in order to produce a series of concentrations, ranging around (0.1 – 100 mM, depending on the system at hand). After the carbons are added and the samples stirred for 24 hours, the carbon settled for 1-2 hours before an aliquot was pipetted out of the supernatant and diluted to concentrations appropriate for measurement in a UV-Visible spectrometer.

Several common isotherm models were used to characterize the adsorption processes in this study.[58, 59] These include the Langmuir, the Freundlich, the Toth, and the Sips (Langmuir-Freundlich) isotherm models. The Langmuir isotherm model reflects homogenous surfaces, with only monolayer coverage, and no adsorbate-adsorbate interactions along the plane of the surface. Eq. 6. Where q_e is the quantity adsorbed per gram carbon (mg g^{-1}), Q^o is the monolayer adsorption capacity (mg g^{-1}), b is a constant related to the enthalpy of adsorption, and C_e is the equilibrium concentration (mg L^{-1}). The Freundlich equation is frequently, and historically, a good model for adsorption on activated carbons at low to moderate relative concentrations, but often fails as the

adsorption limit is approached. Eq. 7. A good fit can suggest high degrees of surface heterogeneity. Where q_e is the quantity adsorbed per gram carbon (mg g^{-1}), K_F is related to the relative adsorption capacity of the adsorbent (mg g^{-1}), C_e is the equilibrium concentration, and n is a constant related to the adsorbate-adsorbent attraction. The Sips isotherm model is a three-parameter combination of the Freundlich and Langmuir isotherm models. Eq. 8. It is intended as an upgrade to the Freundlich isotherm model, which tends to not fit well at high concentrations. Where q_e is the quantity adsorbed per gram carbon (mg g^{-1}), K_{LF}, a_{LF}, and n_{LF} are the Sips constants and C_e is the equilibrium concentration (mg L^{-1}). The Toth equation is another empirical modification of the Langmuir model. Eq. 9. It can describe heterogenous systems with a wide boundary range. Where q_e is the quantity adsorbed per gram carbon (mg g^{-1}), C_e is the equilibrium concentration (mg L^{-1}), and finally B_T, β_T, and K_T are all unitless parameters.

Eq. 6.	The Langmuir isotherm equation	$q_e = \dfrac{Q^o b C_e}{1 + b C_e}$
Eq. 7.	The Freundlich isotherm equation	$q_e = K_F C_e^{1/n}$
Eq. 8.	The Sips isotherm equation	$q_e = \dfrac{K_{LF} C_e^{n_{LF}}}{1 + (a_{LF} C_e)^{n_{LF}}}$
Eq. 9.	The Toth Isotherm equaiton	$q_e = \dfrac{K_T C_e}{\left(1 + B_T C_e^{\beta_T}\right)^{1/\beta_T}}$

2.4.4 Kinetic studies

The adsorbate uptake rate varied not only from carbon to carbon, but with each adsorbate per carbon. To study the individual kinetic systems the mass of carbon used (50 mg), solution temperature (25 °C), solution volume (100 mL UP H_2O + 1 mL adsorbate solution), initial adsorbate concentration (typically 15 mM stock used) and stirring rate (300 rpm) were all kept constant. To begin a trial a timer was started, and small aliquots were periodically taken throughout the course of each experiment by pipetting 1 mL of solution and filtering it through a syringe filter (fisher, nylon 0.2 µm pore). Each aliquot was subsequently diluted directly into a cuvette for UV-Vis analysis. Aliquots were taken periodically over the course of an hour or more.

Kinetic data was then modelled using several selected kinetic models, including the pseudo-first order and pseudo-second order models.[60-62] The modelling only uses data prior to approaching equilibrium to avoid unwarranted bias toward the pseudo-second order.[63] A good fit to the pseudo-first order model (Lagergren model, Eq. 10) could suggest that the adsorption procedure is primarily influenced by the adsorbate concentration. Where q_e $(mg \cdot g^{-1})$ represents the equilibrium capacity, q_t $(mg \cdot g^{-1})$ represents the adsorbate uptake at time t (min), and K represents the first order adsorption rate $(L \cdot min^{-1})$. The pseudo-second order model (Eq. 11) can suggest that the rate of adsorption is proportional to the adsorbate concentration and the available sites on the adsorbent. Where q_e $(mg \cdot g^{-1})$ represents the equilibrium capacity, q_t $(mg \cdot g^{-1})$ represents the adsorbate uptake at time t (min), and k_2 represents the second order adsorption rate constant. The Elovich model (Eq. 12) is an empirical model based upon the assumption that activation energy increases with time on a heterogeneous surface. Where q_t $(mg \cdot g^{-1})$ represents the adsorbate uptake at

time t (min), α is related to the initial adsorption rate (mg $\cdot$ g^{-1} $\cdot$ min^{-1}) and β_e is the desorption constant. The intraparticle diffusion model (Weber and Morris model, Eq. 13) is used to try and elucidate the rate limiting step during the adsorption process. Where q_t (mg $\cdot$ g^{-1}) represents the adsorbate uptake at time t (min), k_{id} is the intraparticle diffusion constant, and C (mmol/g) is a constant related to the boundary layer effect. When $C \approx 0$, interparticle diffusion is the rate limiting process. When $C \neq 0$, multiple processes are controlling the adsorption rate.

Eq. 10	The pseudo-first order model	$\log(q_e - q_t) = \log q_e - \dfrac{K}{2.303}t$
Eq. 11	The pseudo-second order model	$\dfrac{t}{q_t} = \dfrac{1}{k_2 q_e^2} + \dfrac{t}{q_e}$
Eq. 12	The Elovich model	$q_t = \dfrac{1}{\beta_e}\ln(\alpha\beta_e) + \dfrac{1}{\beta_e}\ln t$
Eq. 13	The intraparticle diffusion model	$q_t = k_{id}t^{0.5} + C$

3. Capturing CO_2 using porous carbon materials

As will soon become apparent (if the table of contents did not give it away), the precursor of choice in these studies is L-Histidine HCl. This decision was largely made based upon empirical evidence. When it came to the capture of CO_2, histidine-derived porous carbons simply proved best in our surveys. This isn't to say that other precursors, amino acid or otherwise, were not strongly considered. For example, both arginine and lysine produced competitive chars. Ultimately, surveys continued to suggest that histidine produced the most consistent and highest achieving CO_2 capacities. Therefore, as you have already seen and will continue to see, histidine-derived porous carbons form the basis of this body of work.

3.1 NaOH-activated histidine porous carbons

Anthropogenic CO_2 release is a prominent cause of several global crises including rising global temperatures and the disruption of the oceanic $CaCO_3$ system that has led to increase acidification of marine waters and to the consequent death of coral reefs. Thus, CO_2 capture and remediation are pressing issues motivating copious amounts of research [64-66]. Carbon Capture and Sequestration (CCS) technologies aim at reducing the CO_2 emissions at large emitting sources, as thermoelectrical power plants. These technologies cover the separation of carbon from an effluent gas stream, and its transport to geological storage sites (saline aquifers, the ocean) or to plants for mineralization [67].

Pipes are the most cost effective method of transport to permanent storage sites [67], but most suitable and reusable technologies to separate and temporarily store CO_2 from air

and post-combustion streams are still being investigated. Monoethanolamine (MEA) has been proposed for CO_2 separation, but it is very corrosive and volatile [67]; non-volatile room temperature ionic liquids (RTIL) have also been proposed as alternatives to MEA [68]. The latter, however, have low adsorption capacity as compared to most solids, mostly due to the high viscosity and density of RTIL. Thus, RTIL are more efficient for gas separations when immobilized on a porous support, for which high gas permeance and solubility are achieved [69, 70]. Pores are classified according to size by the IUPAC, as micropores (widths < 2 nm), mesopores (widths between 2 nm and 50 nm) and as macropores (widths > 50 nm) [71]. While such nanocomposites are substantially more effective for the CO_2 separation than bulk RTIL [69, 70], major drawbacks of supporting IL onto porous supports include added cost of the sorbent and the decreased CO_2 gravimetric capacity.

Thus, functional porous materials appear as more promising and inexpensive alternative to supported IL and to MEA. Just as there are assorted strategies to capture or eliminate CO_2, such as selective membrane diffusion [72], physisorption [73], chemisorption [74-76] and metal-catalyzed conversion [77], so are there diverse materials utilized in these strategies, e.g., activated carbons [72, 73, 78-80], metal organic frameworks (MOF) [73], nanoparticle organic hybrid materials (NOHM) [74, 75], zeolites, mesoporous silicates, and various membranes [81].

Among all aforementioned materials, functional activated carbon sorbents appear as more inexpensive and readily available candidates for reversible carbon capture technologies to be deployed. The reasons include the availability of raw precursors (including agricultural waste) [82], good thermal and chemical stability, and methods to tailor pores the amounts of ultramicropores (pores smaller than 0.7 nm) and supermicropores

(pores with widths between 0.7 and 2 nm) for optimum CO_2 adsorption properties [83]. Moreover, N-doping in porous carbons is another effective way to introduce polar surface groups for CO_2 separations, which can be attained by use of N-containing precursors [84-88].

Some natural compounds have abundant N-containing sites, e.g., chitin and chitosan [89-91]. But compared to natural precursors, synthetic compounds and polymers have better defined carbon to nitrogen ratios, and yield materials with more predictable properties. Among synthetic precursors, room temperature ionic liquids (RTIL) and task specific ionic liquids (TSIL) emerged as precursors to high surface area carbons with high nitrogen contents [85, 92-97]. Similarly, polyacrylonitrile (PAN)[98], polypyrrole (PPY), and formaldehyde based resins [99] yield carbons that are rich in nitrogen. Despite the many advantages of such TSIL, polymers and resins, most compounds and precursors are not readily available [100], release toxic pyrolysis byproducts [101] or are cost prohibitive for large scale CCS implementation. Consequently, more readily available and environmentally benign compounds to microporous carbons and that are rich in nitrogen groups are of interest for large scale uses.

Such precursors include amino acids (AA) that have unique compositions with primary, second and tertiary amines [102]. Among the twenty AA taking part in protein synthesis, L-Histidine has one primary amine plus an aromatic imidazolium ring [102], making this a valuable source of different and abundant N-sites in final carbon materials. Given the rich variety of N-groups in amino acid precursors, especially in L-His to prepare functional carbons and of L-His as a N-rich raw material, it is important to develop recipes to obtain carbons using non-volatile L-His TSIL and in optimizing the final yields, chemical and adsorption properties. And while these materials have been used to produce

carbon quantum-dots [103], they have not been extensively investigated as solo components for carbonization towards activated carbons. In this work, inexpensive and readily available L-His was tested as precursor to high surface area activated carbons. The ratios of L-His to NaOH as activating agent and the carbonization temperature were investigated. Final materials were tested for their CO_2 adsorption properties and these correlated to calculated adsorption parameters. Results indicate that CO_2 adsorption capacity is more strongly correlated to nitrogen contents of carbons than to specific surface areas.

3.1.1 Material analysis for NaOH activated histidine porous carbons

The TG and DTG profiles under flowing N_2 for the L-His·HCl compound are shown in **Figure 13**. The L-His compound has a well-defined decomposition step below 200 °C and 3 overlapping steps between 200 and 600 °C. Previous study on amino acid L-Lysine pulps containing excess HCl investigated the formation of hyperbranched polymers via thermal polymerization route. The primary mechanism for the polymerization involved the reaction between the carboxylic acid group with the protonated primary amine of a second molecule, thus forming a polyamide oligomer at 150 °C [104]. In case of L-His, besides the primary amine tethered to the alpha carbon (Cα), this molecule has a less sterically hindered secondary amine in the imidazole side chain. The presence of crystallization HCl in L-His ensures that the carboxylate remains protonated, and no tautomeric forms found above pH 6 occur. These tautomeric forms have a deprotonated carbonyl and a protonated primary amine, or a protonated imidazole ring [102]. Besides the carbonyl group, a second proton source is that of the C2 imidazole ring, as it has been

found that this proton in imidazolium cations has a weak acidic character [105]. Hence, the C2 amine and imidazole proton as less reactive sites may explain subsequent condensation reactions between 200 and 400 °C forming a denser carbonaceous compound. At temperatures above 400 °C, the densification of the carbonaceous phase potentially includes the elimination of N-containing fragments, as higher carbonization temperatures yield carbons with lower N-contents.
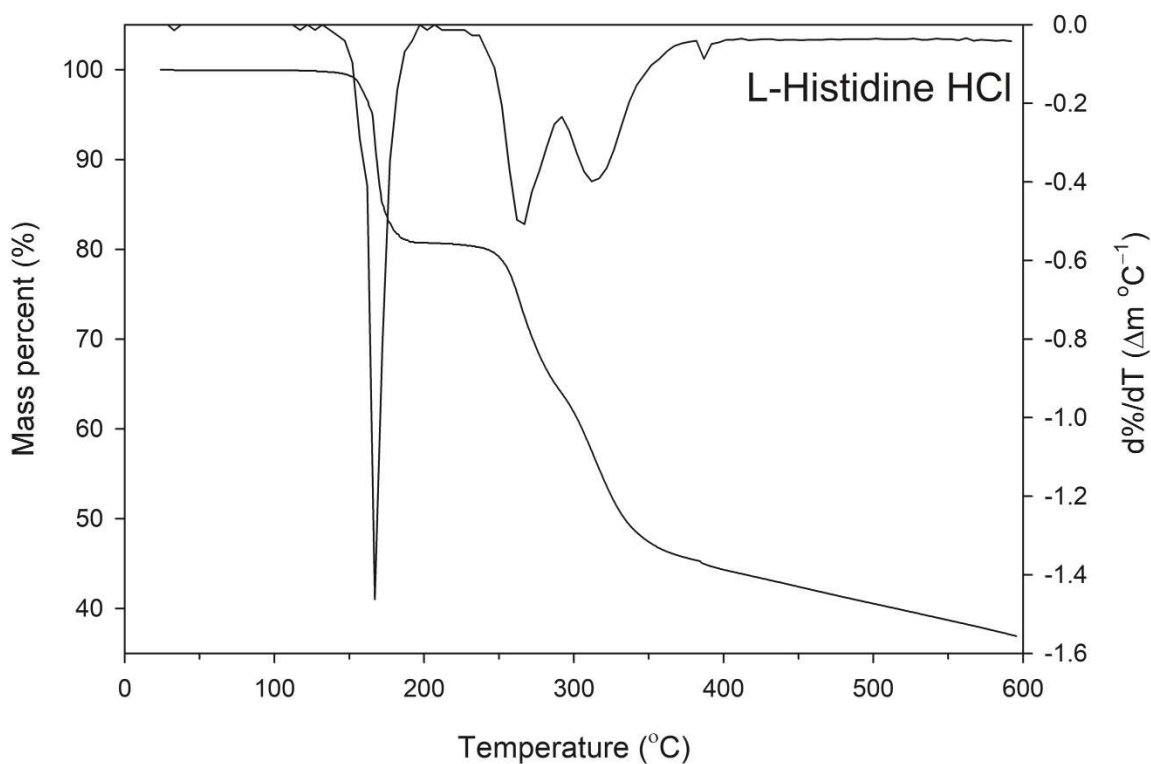
Figure 13. TG profiles under N_2 atmosphere for histidine HCl revealing three significant mass losses around 165, 275, and 320 °C.

The N_2 at -196 °C sorption isotherms, **Figure 14 (a)**, for obtained carbons prepared with NaOH are type I, which is characteristic of microporous materials [71]. The non-

activated compounds have a type II isotherm and with very low gas uptake, indicating that these are non-porous [71].
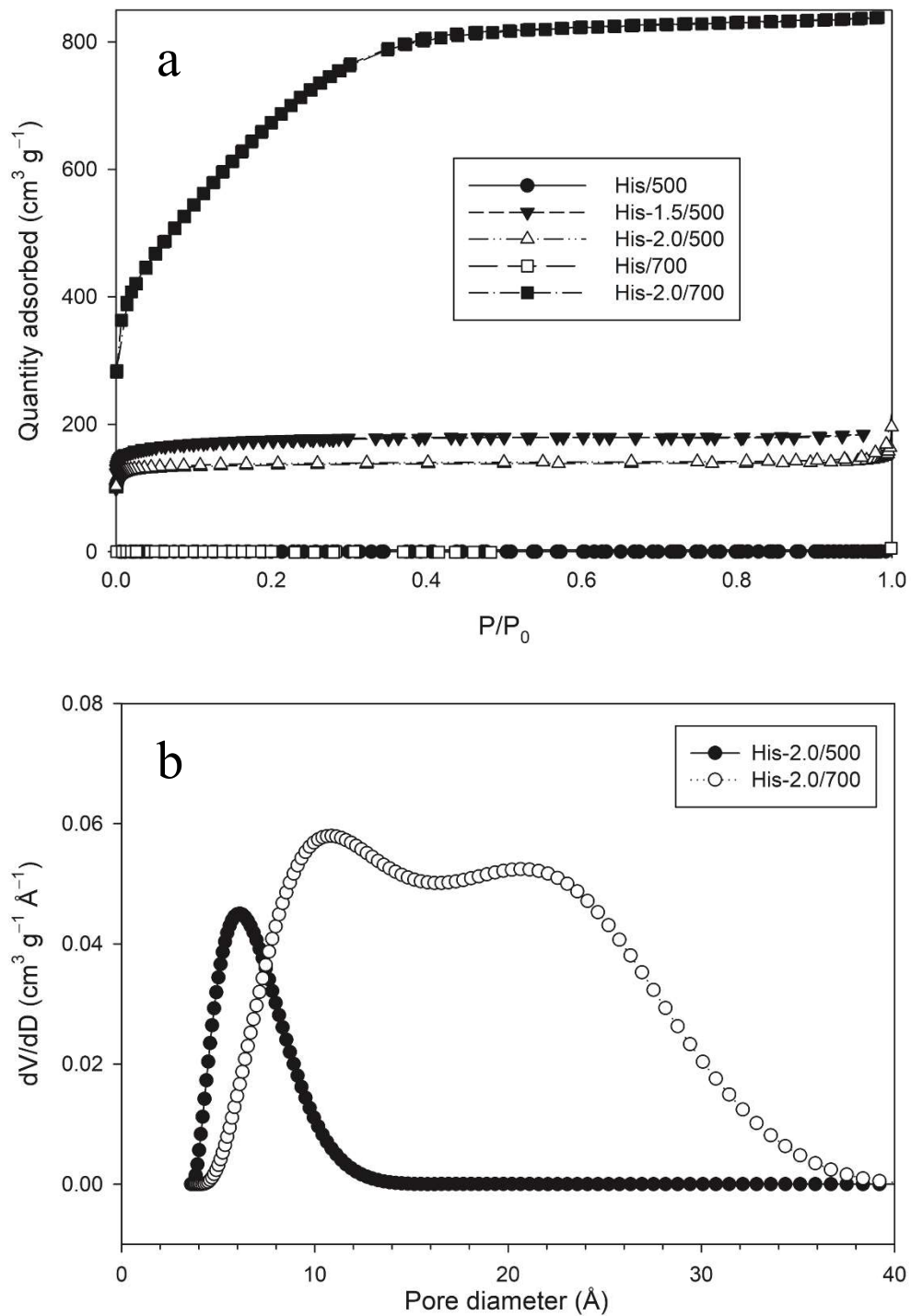
Figure 14. Gas adsorption isotherms for non-activated and activated porous carbons (a) and representative

NLDFT pore size distributions for His-2.0/500 and His-2.0/700 (b).

The calculated adsorption parameters are summarized in **Table 9**. Comparing the specific surface areas for these materials, this parameter increased significantly with the NaOH activation. The most substantial increase in surface area was found when histidine was activated with NaOH and carbonized at 700 °C, resulting in a surface area of 2500 m^2/g. Comparable changes were also observed for the single point pore volume (V_{SP}) and micropores volumes from NLDFT computations (V_{mi}).

Sample	S_{BET} (m^2/g)	V_{mi} NLDFT (cm^3/g)	V_{SP} (cm^3/g)
His/500	0.597	0.00	-
His-1.0/500	409	0.1530	0.1704
His-1.5/500	626	0.26	0.28
His-2.0/500	548	0.19	0.23
His/700	0.835	0.00	-
His-1.0/700	-	-	-
His-1.5/700	1151	0.33	0.61
His-2.0/700	2533	0.74	1.30

Table 9. Summary of calculated parameters from N_2 at -196 °C adsorption isotherms.

Overall, V_{SP} values taken at p/p_0 ~0.98 are slightly greater than calculated V_{mi} as the former contains additional contribution from textural pores. Ratios of NaOH to L-His above 2.0 were not investigated as these yielded no carbon. The mechanism for NaOH activation involves reduction of Na^+ at the expense of carbon oxidation (leading to additional burn-off), and with intercalation of Na^0 into graphene-type domains in the framework of the carbons. By raising the carbonization/activation temperatures, these reactions occur to a larger extent and consequently, the higher the surface areas of the final materials [106]. This has implications in the pore structure of resulting carbons, as seen in the calculated PSD for these materials. For instance, while the calculated PSD for the material His-2.0/500 indicates strictly microporous material with maximum at ~0.6 nm, that for His-2.0/700 is bimodal with maxima at ~1.0 nm and ~2.2 nm, see **Figure 14 (b)**. Similar behaviour was observed for other NaOH ratios and temperatures investigated.

Textural properties of the ultimately top performing carbon, His-2.0/500, were studied using SEM and TEM. The resulting SEM images suggest several stages of activation are present within the sample. **Figure 15**. The bulkier pieces have many small pores approximately 5 μm in diameter dispersed throughout. The overall appearance suggests that these smaller pores expand as the bulk material decayed and eventually break down into a framework-like structure. Further analysis along the edges using TEM suggest that many of these structures are comprised of multiple sheets. **Figure 16**. Yet, the overall material still appears to be amorphous in nature, as very little structural order in the bulk carbon can be identified.

71
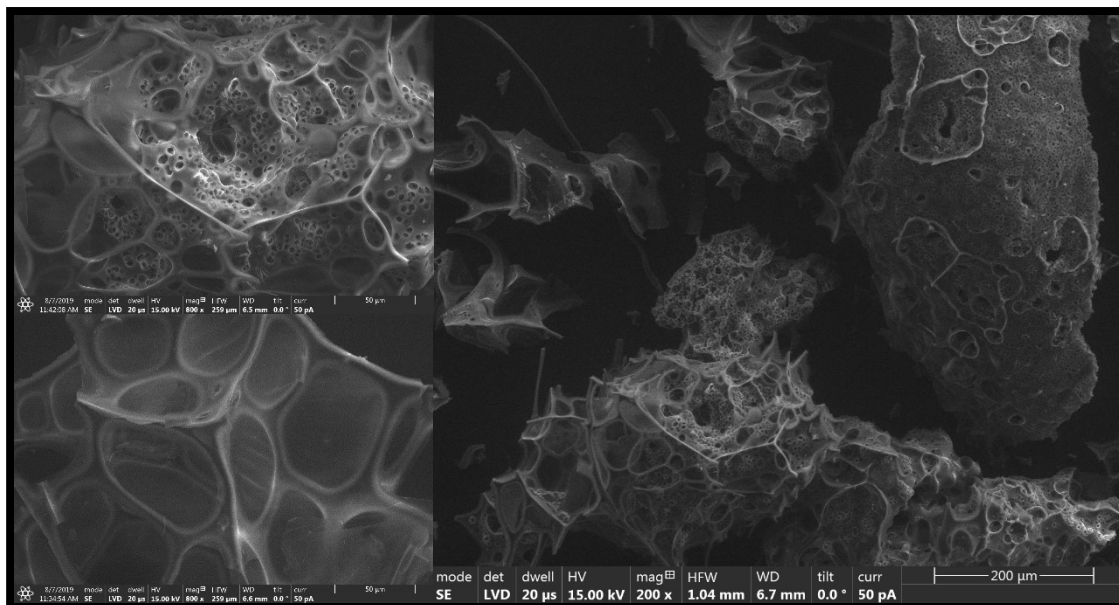
Figure 15. Representative scanning electron microscope images of His-2.0/500 which suggest significant pore formation in the presence of NaOH.
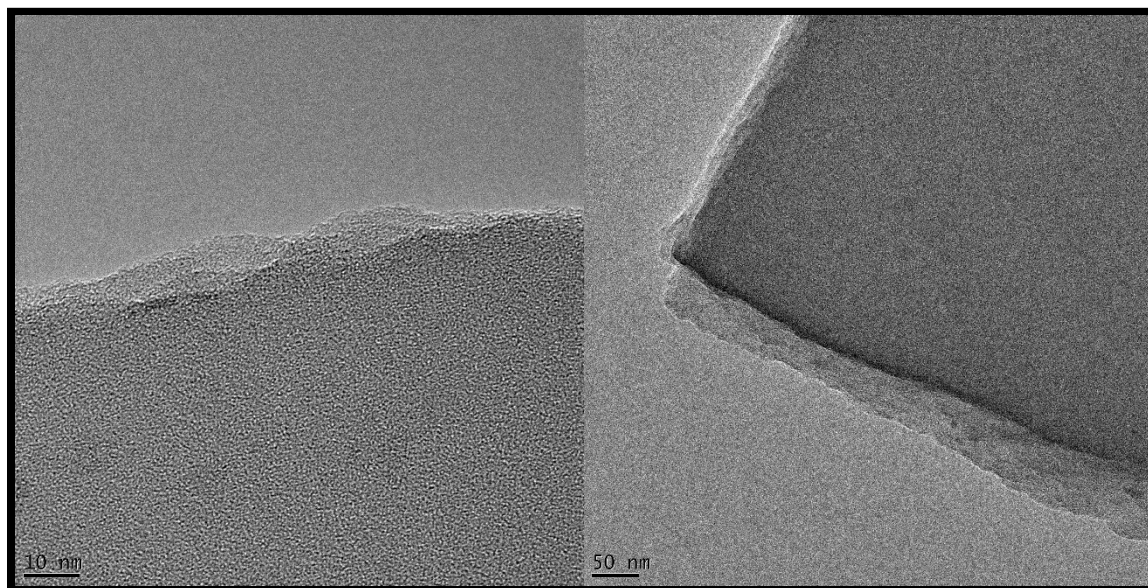
Figure 16. Characteristic TEM images of the edges of His-2.0/500 that appear to show layering of the carbon material.

The elemental composition of the carbon materials was investigated using XPS. **Figure 17**. To determine the impact of activation temperature on relative abundance, His-2.0 samples activated at 500 °C and 700 °C were both analysed. Both activated materials were primarily composed of carbon, oxygen, and nitrogen, however, both products also contained minute quantities of other impurities that were consistent with the composition of the combustion boat. **Figures S6 and S7**. Given their relative abundance, the impurities are considered negligible, and the resultant features of the carbon materials are not attributed to them.
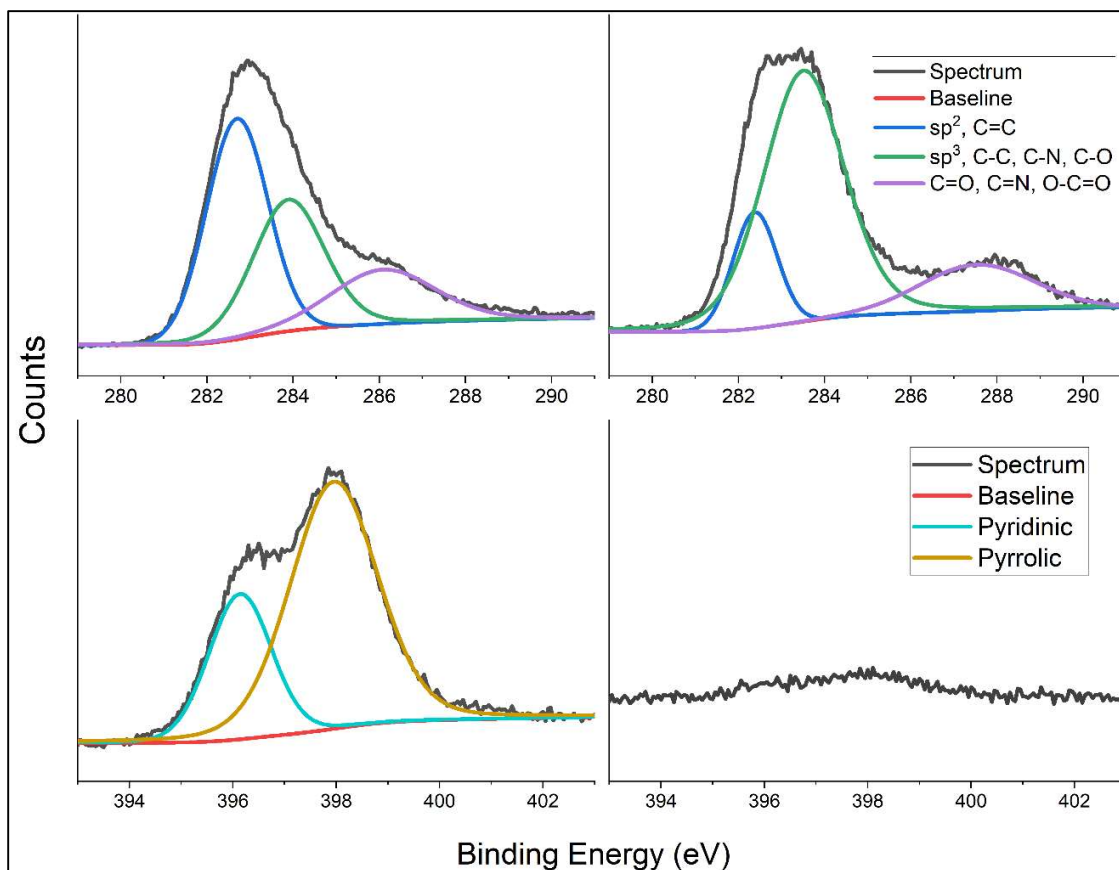
Figure 17. XPS peaks for carbon (A and B) and nitrogen (C and D) for His-2.0 activated at 500 °C (A and C) and 700 °C (B and D) that suggest higher temperature activation results in the loss of nitrogen while carbon content shifts from primarily sp^2 to sp^3 hybridization.

73

Peak fitting on the XPS C1s data from L-His-2.0/500 and L-His-2.0/700 suggest that at increased activating temperatures sp^2 carbons tend to be converted to sp^3 hybridization. More importantly, the overall lack of uniformity within the C1s data lends credence to the amorphous nature of these carbon materials.

When considering CO_2 capture, relative abundancies of carbon and nitrogen are often of primary interest. XPS analysis shows that as the soak temperature increases to 700 °C, the nitrogen abundance diminishes drastically. This can easily be seen when comparing this to the nitrogen remaining under milder activating temperature (500 °C). **Figure 17**. Peak fitting L-His-2.0/500 suggests two predominant peaks around 396.1 and 398 eV. These are primarily attributed to pyridinic and pyrrolic nitrogen, respectively. The possibility of a smaller peak around 400 eV (typically attributed to graphitic nitrogen) can be seen but is inconclusive. Overall, this suggests that the nitrogen content is primarily associated with aromatic or electrically conductive regions of the carbon. Furthermore, determining that pyrrolic nitrogen represents most of the total nitrogen suggests that the initial orientation of the nitrogen within the pyridinic ring present in histidine is not stable during the carbonization process.

3.1.2 Uptake of CO_2 in NaOH-activated histidine PCs

The resulting activated and nonactivated carbons were analysed for CO_2 capture using a thermogravimetric method, see Supporting Information for the method and an example thermogram in **Figure S8**, and **Table 18** for the calculated CO_2 uptakes at various

temperatures. As seen in these results, the non-porous carbons obtained from direct carbonization of the acidic form of L-His possess significant CO_2 adsorption capacities. The activated L-His-2.0/500 yielded a carbon having greater sorption capacities than its acidic analogue (3.382 mmol/g) at a sorption temperature of 25 °C. Notably, this sample has both the highest sorption capacity determined in this study and the fastest kinetics for CO_2 adsorption (see time to reach 90% capacity at 45 °C). All carbons obtained after heat treatment at 700 °C exhibits lower CO_2 sorption capacity.

Sample	n_{CO2} (mmol g^{-1})		Time to capture 90% capacity at 45 °C
	45 °C	25 °C	
His/500	0.471	0.871	99.41
His-1.0/500	1.877	2.984	14.88
His-1.5/500	1.875	3.128	9.74
His-2.0/500	1.954	3.382	3.71
His/700	0.880	1.283	15.15
His-1.0/700	1.104	1.952	4.30
His-1.5/700	0.745	1.401	5.20
His-2.0/700	0.884	1.576	4.96

Figure 18. Summary of gravimetric CO_2 adsorption data for NaOH-activated His-PCs.

The increased CO_2 uptake for carbons produced at 500 °C could be attributed to several features of the carbon. The lower activation temperature resulted in carbons having almost exclusively ultramicropores, the latter being recognisably instrumental for high CO_2 uptakes, as in the present His-2.0/500 sample [83]. Additionally, the high nitrogen content as a result of the lower temperature activation can be implicated as a potential source of capacity.

3.1.3 Conclusions

This study reports the preparation of non-activated and activated carbons from the amino acid L-His for the first time. N-doped activated carbons having well-defined having almost exclusive ultramicropores were obtained from the direct carbonization of L-His neutralized with excess NaOH at various mass ratios. Carbons having specific surface areas near 500-700 m^2/g after carbonization/activation at 500 °C demonstrated more than twice the CO_2 adsorption capacities as compared to their analogues carbonized at 700 °C and having surface areas exceeding 1200 m^2/g. Results indicate the synergistic effect between N-content in low temperature carbonized samples and ultramicropores in carbons prepared at 500 °C. Future studies will investigate the effect of other activating agents, amino acids and the nature and contents of the N-sites in these carbons.

3.1.4 Materials and Methods

Chemicals and reagents.

Unless otherwise noted, all reagents were used as received without further purification. All aqueous solutions and rinses used ultrapure Millipore 18.2 MΩ cm water (referred to herein as refined water). L-Histidine (L-His, ≥99%, H8000) and NaOH (trace metals basis, 99.99%) were purchased from Sigma-Aldrich (St. Louis, MO). Carbon dioxide gas (CO_2, ≥99.9%) was purchased from Airgas.

Neutralization of amino acids.

Neutralization was performed by mixing NaOH/L-His at the mass ratios of 1.0/1.0, 1.5/1.0 and 2.0/1.0 and then grinding them in a pestle and mortar to create a homogenous powder. The resulting fine powders were carbonized at either 500 or 700 °C under flowing N_2 using a programmable Thermo Scientific Lindberg/Blue horizontal quartz tube furnace (Model TF55035A) and quartz crucibles. Activated samples were washed with copious amounts of water, and then dried at 100 °C. Final carbon materials were labeled as His-*w*/T, where *w* is the NaOH/L-His ratio of 1.0, 1.5 or 2.0, and T the carbonization temperature (500 or 700 °C). The nonactivated samples were labeled as His/T.

Thermogravimetric analysis of CO₂ capture and reversibility.

Approximately 5-15 mg of carbonized material was weighed on a tared Pt sample holder contained within the furnace of a TA Instruments Q50 TGA. Prior to the start of analysis, a drying step was performed wherein samples were heated to 100 °C under 65 mL min^{-1} N_2 gas flow until the sample mass stabilized. The sample chamber was then cooled to 45 °C and subsequently flushed with CO_2 (65 mL min^{-1}) over several hours as the mass of the sample was monitored. Once the sample mass stabilized, the sample chamber was cooled to 25 °C and the CO_2 flush was continued until the sample mass again stabilized. A test with an empty crucible and the same temperature program and atmospheres was performed to rule out any buoyancy effects.

Surface area and pore size analysis.

N_2 adsorption at -196 °C analysis was completed using a Micromeritics ASAP 2020 volumetric analyzer. Samples were outgassed at 200 °C for at least 2h under vacuum prior to analysis. Surface area was calculated using BET method and the relative pressure range of 0.05-0.20 [71]. Single point pore volumes were taken at the relative pressure of 0.98. Pore size analysis was performed using non-local density functional theory (NLDFT) [107] and the slit-pore model for carbons applied to the adsorption branch of the isotherms.

Textural and elemental analysis.

Scanning electron microscopy (SEM) was performed on a Scios Analytical Dualbeam. Transmission electron microscopy (TEM) was performed using a FEI Tecnai F30 Twin 300kV TEM. A lacey carbon grid was used as the support for analysis. Elemental analysis was performed using X-ray photoelectron spectroscopy (XPS) with a Physical Electronics 5000 VersaProbe II Scanning ESCA Microprobe. Results are reported as found, and not charge-corrected.

3.2 ChoOH-His Ionic liquid derived porous carbon materials

The increase in the global atmospheric concentration of greenhouse gasses, such as CO_2, from anthropogenic sources has resulted in a changing climate that has been linked to many unwelcome outcomes, such as a rise in the frequency and intensity of extreme weather events, ocean acidification, habitat loss, and more.[108] Despite these negative impacts, the release of these greenhouse gasses appears to be something that humanity will continue to do for some time to come.[109] To combat this, various carbon capture technologies exist and are being developed and implemented towards the sequestration of CO_2 and other greenhouse gasses.[110]

Among the various technologies, porous carbons (PCs) have been considered good materials for CO_2 sequestration considering their high surface areas, tunable pore sizes, and adjustable surface chemistry.[111, 112] In particular, microporosity and embedded functional groups in the surface are considered the keys to CO_2 capture in PCs. Among these functional groups, nitrogen is often considered the most important for implementing polar surface groups that are capable of interaction with CO_2. Incorporating nitrogen into the surface of these materials can be the result of 'N' being in the precursor material or adding in dopants during the carbonization and activation process. As we have shown in other works, the precursor histidine can produce high surface area porous carbon materials and has multiple nitrogens incorporated into the precursor structure.

Ionic liquids (ILs) have also proven themselves as capable precursors for high surface area carbons with high nitrogen contents.[85, 92-97] One IL that has not been tested for

such an application is the combination of choline hydroxide (ChoOH) and histidine.[113, 114] This could be of particular interest as this room temperature IL is comprised of two nitrogen-containing precursors.

Herein, we investigate PCs produced using the ChoOH-histidine IL precursor, and activated with several activating agents (KOH, NaOH, and $ZnCl_2$). The samples were labeled using the following template: Z[T]-X-Y where Z represents the AA used, T is the soak temperature, X and Y are the molar ratios of the AA and His used to ChoOH. For example, K700-7-3 is a carbon produced with KOH at 700 °C, with a molar ratio for ChoOH:AA:His of 1:7:3.

3.2.1 Textural and chemical analysis of ChoOH-His PCs

Initially, KOH was used as the activating agent and both temperature and molar ratios were optimized here for increased surface capacity. **Figure 19.** A variety of temperatures were applied; however, it was quickly found that moderate activating conditions of around 700 °C were best for producing highly porous carbon materials.
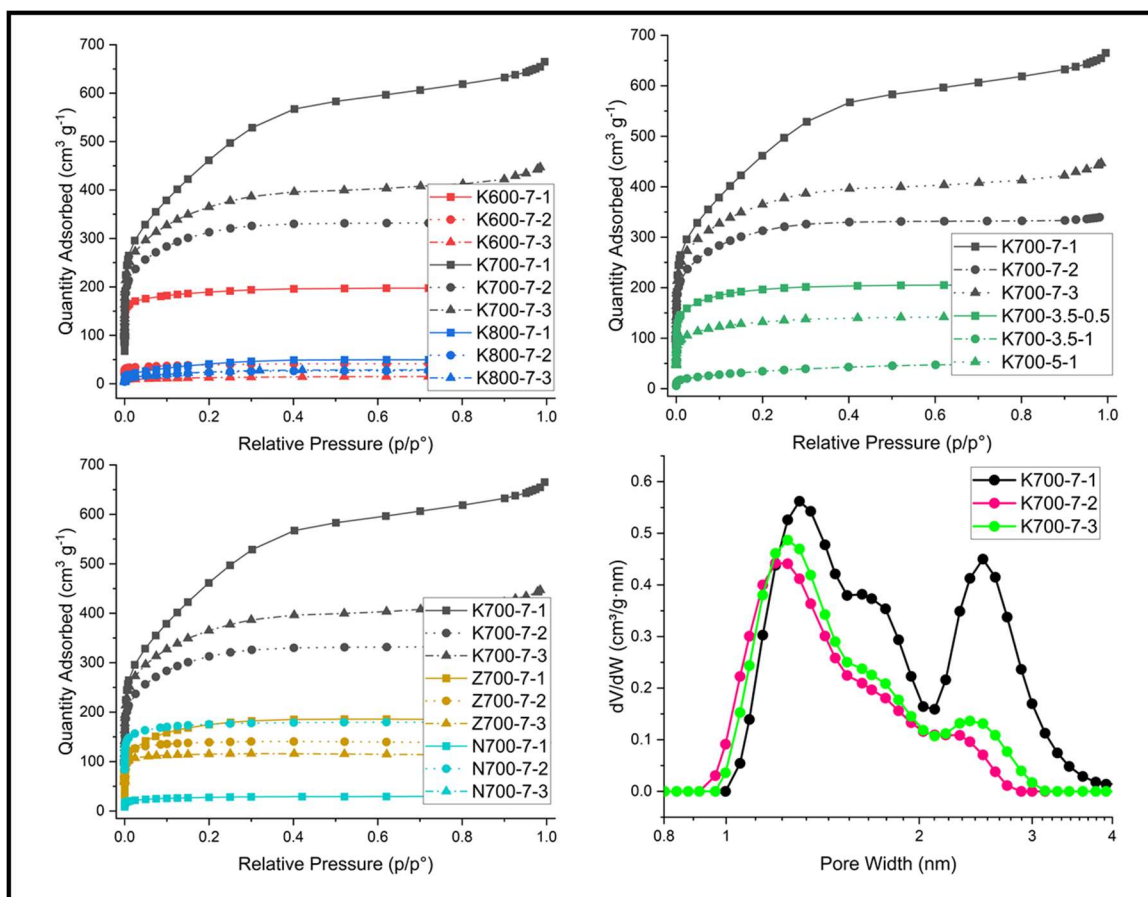
Figure 19. N$_2$ @ 77 K isotherms for select activated [ChoOH] [His HCl] porous carbons used in this study produced with varying temperatures from 600 – 800 °C (a), varying molar ratios (b), and varying the activating agent (c). Additionally, the pore size distribution plots for highest achieving porous carbons (d) can be seen to reveal three primary pore sizes at approximately 1.3, 1.7, and 2.5 nm, with magnitudes varying with the carbon.

When activated at 600 °C, only the molar ratio with the smallest quantity of histidine resulted in very large SSA (K600-7-1, 723 m^2 g^{-1}), while increasing amounts of histidine resulted in rapidly diminishing SSA and porosity. **Table 10.** One possibility is that choline hydroxide can produce a highly porous material under such conditions, but pore blocking effects are occurring with increasing quantities of histidine. Additionally, other work in our lab has shown that 600 °C is around the minimum temperature required for activated histidine materials to achieve good textural properties (see other chapters).

Sample	BET Surface area $(m^2\ g^{-1})$	t-plot Micropore volume $(cm^3\ g^{-1})$	@ p/po > 0.9 Total pore volume $(cm^3\ g^{-1})$
K600-7-1	723.7	0.249	0.311
K600-7-2	145.1	0.046	0.068
K600-7-3	43.9	0.009	0.026
K700-7-1	828.2	0.285	1.029
K700-7-2	656.4	0.229	0.525
K700-7-3	925.4	0.284	0.691
K800-7-1	142.2	0.011	0.082
K800-7-2	86.0	0.014	0.047
K800-7-3	82.4	0.011	0.084
K700-3.5-0.5	720.9	0.257	0.324
K700-3.5-1	128.7	0.005	0.075
K700-5-1	492.4	0.151	0.231
N700-7-1	100.4	0.033	0.061
N700-7-2	676.6	0.247	0.283
N700-7-3	Poor product yield		
Z700-7-1	654.1	0.283	0.290
Z700-7-2	546.2	0.200	0.219
Z700-7-3	461.2	0.170	0.176

Table 10. Summary of critical N2@77 K GAA properties for ChoOH-His activated carbons.

Activation conditions of 800 °C proved to be too hot, and all materials had significantly reduced SSA and porosity. The highest achieving among these, K800-7-1, contained a SSA of 142.2 $m^2\ g^{-1}$, with the others being less than 100 $m^2\ g^{-1}$. It is thought that after pore development occurred during the ramping period of the activation process, the high heat led to over activation of the materials (the product yield was perceptibly much smaller, though not directly measured).

When activated at 700 °C, multiple porous carbons are produced with good SSA and porosity. **Figure 19.** Interestingly as the ratio of histidine increases, the textural properties first decrease, then increase. Like the 600 °C set of carbons, this could be the result of the K700-7-1 carbon having more properties resultant of choline hydroxide, whereas in K700-7-3, histidine is the principal source of the final material's textural properties. As such, the PSD is highly impacted by this ratio. In particular, K700-7-1 has more total pore volume (TPV) than K700-7-1 or -2, but this increase in porosity is entirely the result of larger pores around 1.7 and 2.6 nm. Smaller pores around 1.2 nm were found in similar quantities in all three of these materials. The largest SSA was with K700-7-3 which contained 925.4 m^2 g^{-1} and 0.691 cm^3 g^{-1} TPV, whereas the largest TPV was K700-7-1 which contained an 828.2 m^2 g^{-1} SSA and 1.029 cm^3 g^{-1} TPV.

The molar ratio was then further investigated for its affect on the textural properties of the PCs. The initial ratios were decided upon based upon a combination of previous work which suggests that a 1:7 molar ratio between histidine and KOH is optimal and choosing molar ratios between histidine and choline hydroxide that produces an ionic liquid. It became apparent quickly that these were the optimal ratios, as variations in the molar ratios produced many products with inferior textural characteristics. **Figure 19.** Doubling the choline hydroxide ratio (K700-3.5-0.5) proved to be the least detrimental of the variations attempted. However, the most surprising result might be how sensitive the KOH ratio is, as reducing the ratio of Choline/Histidine:KOH from 1:7 to 1:5 decreases the SSA and porosity by nearly half, while increasing the ratio beyond 1:7 results in virtually no product yield, probably due to overactivation of the carbon structure.

Finally, as a last variation two alternate chemical activating agents were used, NaOH and $ZnCl_2$. While the activation processes are thought to be similar for NaOH and KOH, $ZnCl_2$ activates very differently. Still, for simplicity the peak KOH molar ratios are used for these two activating agents. **Figure 19.** Despite previous work suggesting that NaOH activation in histidine-derived carbons can lead to similar or even larger SSA and PV, here they were not as successful as KOH. N700-7-1 only contained 100.4 m^2 g^{-1} with N700-7-2 earning a more respectable 676.6 m^2 g^{-1}. N700-7-3 did not produce significant product yield, likely due to over activation of the carbon structure. These NaOH-activated carbons were almost completely microporous in nature.

Activation with $ZnCl_2$ was much more consistent, though only modest. The carbon Z700-7-1 had the best SSA and porosity, with 654.1 m^2 g^{-1} of surface area and 0.290 cm^3 g^{-1} of total pore volume, of which 0.283 cm^3 g^{-1} is micropore volume. Increasing the relative quantity of histidine provided diminishing returns for these properties, with Z700-7-2 and Z700-7-3 only having SSAs of 546.2 and 461.2 m^2 g^{-1}. Again, these isotherms suggest a primarily microporous material, with little mesoporous development.

IR spectrometry was undergone to better understand the chemical nature of the adsorbents. **Figure 20.** The IR spectra for the porous carbon material 1653 (shoulder) assigned to NH_3^+ deformation asymmetrical peaks, indicating that nitrogen functional groups were maintained in the final porous carbon product. The only place a similar peak can be found is in the His HCl H_2O IR spectra. A smaller symmetrical peak at 1474 cm^{-1} was also assigned to NH_3^+ deformation. A similar peak is only also found in the ChoOH spectra. Together, these results could suggest that the nitrogen content of the final porous carbon material is sourced from both nitrogen containing precursors.

A peak around 1579 cm^{-1} was also found in both His HCl H$_2$O and the final porous carbon product. This was assigned to COO$^-$ asymmetrical deformation. It also shows an unsurprising peak around 3411 cm^{-1}, matching the sharper peak found in His-HCl H$_2$O that is assigned to -OH and N-H stretching peaks. Similarly, a peak at 1330 cm^{-1} was assigned to O-H deformation and C-N stretching.
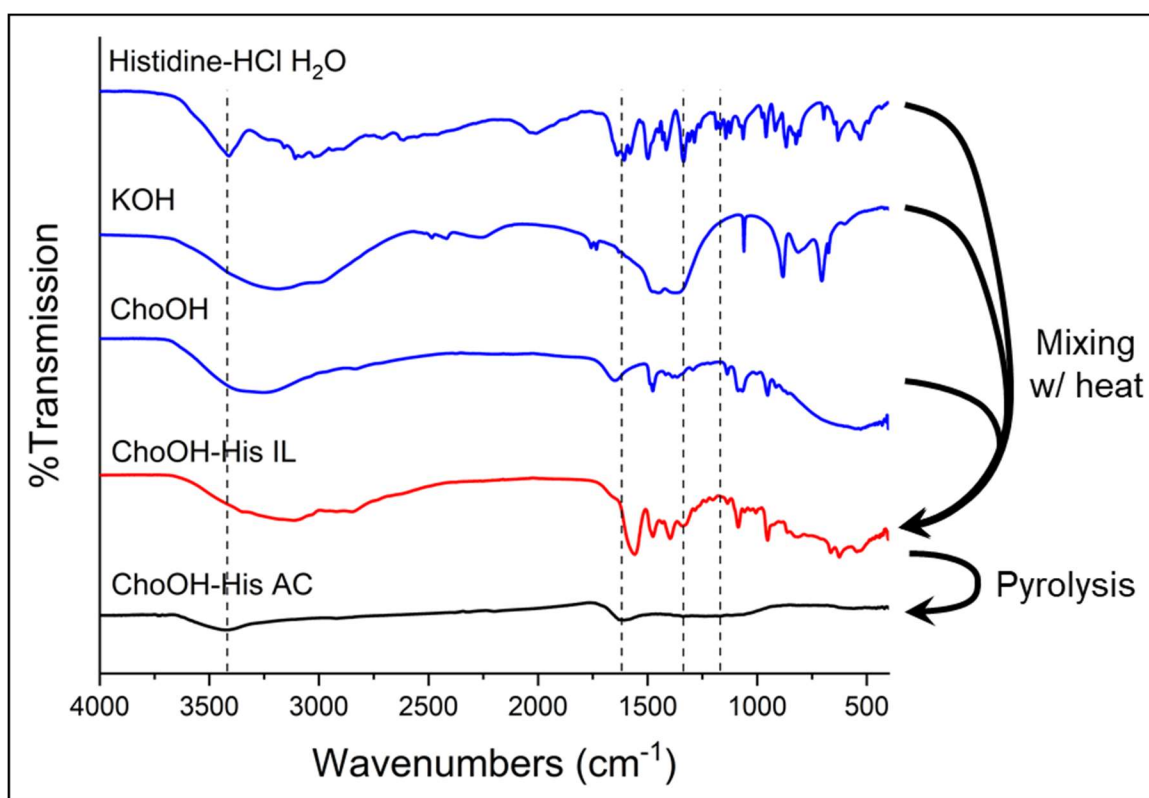
Figure 20. IR spectra for precursor materials Choline hydroxide, KOH, and histidine HCl, as well as ChoOH-His-based ionic liquid, and the resultant porous carbon material. The spectra show several peaks that seem to translate from precursor materials to final carbon product.

3.2.2 Analysis of CO_2 and N_2 isothermal data at 0 °C

The carbons were finally tested for their ability to capture CO_2 and have shown great promise. **Figure 21.** The top performing carbons were K700-7-3 and K700-7-1 which captured a very good 8.30 and 5.57 mmol g^{-1} of CO_2, respectively. However, their isotherms strongly suggest that these two carbons capture CO_2 in very different manners. Physisorption appears to be the primary source of uptake for the porous carbon K700-7-3, which has a nearly linear uptake that continues to increase rapidly as we approach atmospheric pressure. This can be seen as typical for a primarily physisorption based process. In comparison, K700-7-1 has an isotherm that increases rapidly at low pressures before the uptake slows as the pressure increases, as typically associated with chemisorption or mixed chemisorption and physisorption processes.

Despite having a smaller maximum uptake (5.57 vs 8.30 mmol g^{-1}), these results suggest that K700-7-1 might translate into better real-world CO_2 adsorbent. Since chemisorption tends to be a more selective type of adsorption, any chemisorption process that uptakes CO_2 here would likely still favor CO_2 in a system with more than one gas. Furthermore, uptake at low relative concentrations of CO_2 also favors real-world translation, as most applications for sequestering CO_2 occur at considerably smaller relative pressures than 1 atm CO_2.

This can further be evidenced by the selectivity of CO_2 over N_2, as indicated by the max CO_2 uptake divided by the max N_2 uptake. **Table 11.** At 0 °C it is always expected that the ratio of CO_2/N_2 will be greater than one. This is due to the operational temperature being much closer to the boiling point of CO_2 than that of N_2. However, this ratio can vary

depending upon how selective any adsorbent is towards CO_2. In this study K-700-1 had the highest selectivity for CO_2 with a CO_2/N_2 value of 9.47 whereas K700-7-3 had the smallest at 5.17. In combination with the isotherms shapes, this strongly suggests that in a system with multiple gasses present K700-7-3 would be much less effective at separating CO_2, while K700-7-1 shows much promise.
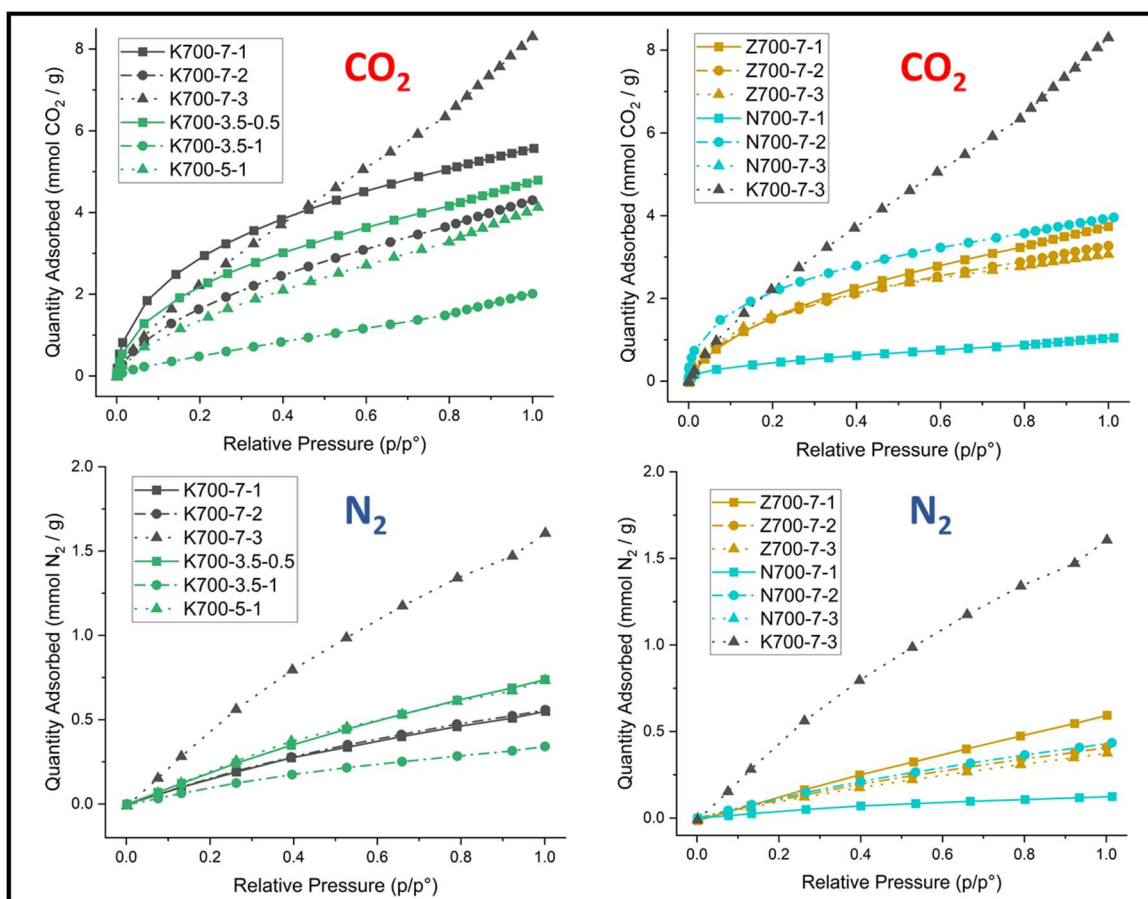
Figure 21. CO_2 (a, b) and N_2 (c, d) isotherms at 0 °C for select carbon materials used in this study with the top performing adsorbent repeated for comparison. Several isotherm shapes can be seen and suggest that different uptake mechanisms are present for different carbons.

	Max capacities at 1 atm, 0 °C		Selectivity
Sample	CO$_2$ capacity	N$_2$ capacity	CO$_2$/N$_2$
K600-7-1	3.409	0.526	6.485
K600-7-2	2.211	0.261	8.464
K600-7-3		Not tested	
K700-7-1	5.569	0.588	9.469
K700-7-2	3.349	0.403	8.314
K700-7-3	8.302	1.605	5.173
K700-3.5-0.5	4.792	0.738	6.497
K700-3.5-1	2.102	0.341	6.163
K700-5-1	4.128	0.733	5.628
N700-7-1	1.047	0.124	8.429
N700-7-2	3.959	0.435	9.101
N700-7-3		Poor product yield	
Z700-7-1	3.739	0.594	6.297
Z700-7-2	3.274	0.408	8.019
Z700-7-3	3.063	0.375	8.167

Table 11. CO$_2$ and N$_2$ 0 °C isothermal data for choline-hydroxide and histidine derived carbons produced at 700 °C.

While the carbons were optimized for their textural properties, all produced carbons were still tested for their CO$_2$ capture capacities. Unfortunately, none of the other variations were found to be as effective for CO$_2$ sequestration as K700-7-1. The next highest was found by doubling the relative amount of choline chloride, however this not only had a smaller CO$_2$ uptake (4.79 mmol g^{-1}) but also had a much poorer selectivity (6.50). Switching to a different activating agent also did not result in better CO$_2$ sorbents. The best uptake for a ZnCl$_2$ activated material was Z700-7-1 with 3.74 mmol g^{-1}. The best uptake for NaOH activation was N700-7-2 with 3.96 mmol g^{-1} CO$_2$. Additionally, this material has a very good selectivity with CO$_2$/N$_2$ being 9.10. Especially considering the lack of

product for N700-7-3, it is conceivable that further research fine-tuning the activation conditions for NaOH activation could result in porous carbons that have similar CO_2 sequestration abilities as K700-7-1.

3.2.3 Conclusion

A promising new porous carbon material was investigated here. The ionic liquid produced using a 1:1 molar ratio of choline hydroxide and histidine and activated with a 1:7 molar ratio of histidine to KOH was shown to be capable of capturing 5.57 mmol of CO_2 per gram of sorbent, with a high degree of selectivity ($CO_2/N_2 = 9.47$). Future studies applying this material should be directed towards applying mixed gas systems that resemble atmospheric or industrial conditions where this sorbent might be implemented.

When produced with a 1:3 molar ratio of choline hydroxide to histidine an outstanding 8.30 mmol g^{-1} of CO_2 was able to be taken up at 0 °C and 1 atm (100% CO_2); however, given poor selectivity and an isotherm that suggests physisorption as the key uptake mechanism, we consider this to be a poor candidate for real-world application.

Activation with KOH also proved to be the most successful under similar activating conditions and molar ratios when compared to NaOH and $ZnCl_2$ activation. However, these activating agents were not fully evaluated and further tweaking of the activating conditions and molar ratios might be undertaken, especially considering the good selectivity and uptake that this initial research suggests.

To fully ascertain the nature of the carbon capture mechanism, more information is needed regarding the chemical makeup of the surface. Elemental analysis, preferably via

XPS, should be conducted to better understand the overall chemical abundance and gain insight into the nature of each element still present on the carbon's surface. However, any form of elemental analysis would still prove beneficial. Further study of the chemical nature of the carbons using instrumentation or wet chemistry techniques could then be followed and used in conjunction with the elemental analysis to form a stronger understanding of the nature of the carbons.

3.2.4 Materials and Methods

Materials

Unless otherwise noted, all reagents were used as received without further purification. All aqueous solutions and rinses used ultrapure Millipore 18.2 MΩ cm water (referred to herein as refined water). L-Histidine (L-His, ≥99%, H8000) and NaOH (trace metals basis, 99.99%) were purchased from Sigma-Aldrich (St. Louis, MO). Carbon dioxide gas (CO_2, ≥99.9%) was purchased from Airgas.

Production of precursor materials

The preparation of the precursor materials was a simple one step process. First, the appropriate quantity of chemicals were weighed out and combined in a sealed vial with a stir bar. This vial was placed on a hot plate set to ~70 °C and stirring is initiated until a homogenous mixture is achieved. It should be noted that not every molar ratio used completely produced liquid, but residual solid was well dispersed prior to use. The

intermediate materials were named Z-X-Y, where Z refers to the AA used and X and Y were the molar ratios of the AA and His, compared to 1 mole of ChoOH. For example, K-7-3 was produced with ChoOH:KOH:His in a 1:7:3 molar ratio.

Production of PCMs

Porous carbons were produced in a STF1200 tube furnace with a 4 in. ceramic tube under the 200 mL min^{-1} N_2 flow. Prepared IL was transferred to a ceramic boat and placed in the center of the tube furnace. Initially, the temperature was raised to 100 °C for one hour, to purge the tube with N_2. After, the temperature was increased at a rate of 10 °C min^{-1} to a set value (e.g., 700 °C) and maintained at this 'soak' temperature for 2 hours. Finally, the temperature was allowed to naturally cool under flowing N_2.

The samples were labeled using the following template: Z[T]-X-Y where Z represents the AA used, T is the soak temperature, X and Y are the molar ratios of the AA and His used to ChoOH. For example, K700-7-3 is a carbon produced with KOH at 700 °C, with a molar ratio for ChoOH:AA:His of 1:7:3.

The resultant PCs were then prepared for analysis. Initially, the PCs were rinsed with 200 mL DI. Next, they were subjected to a 0.1 M HCl bath for 24 hrs to dissolve any ash and residue. Finally, the PCs were rinsed with DI until the pH of the eluent was neutral. The PCs were then dried in an oven and used as described below.

Analysis of materials

Gas adsorption analysis (ASAP 2020, Micromeritics) with nitrogen (Airgas, >99.999%) at 77 K was used to define total surface area and pore volume, as well as probe the pore structure. All resulting data was analyzed using Micromeritics ASAP 2020 Plus software, version 2.00. The single point total pore volume was determined at relative pressures of ≥ 0.99 P/P°. Brunauer-Emmett-teller (BET) theory was used in conjunction with a Rouquerol BET plot to determine the total surface area of the carbons. The t-plot method, using the carbon black STSA statistical thickness equation, was used to determine micropore volume. NLDFT using a kernel for N_2 at 77 K on carbon black slit pores was used to determine micropore size and pore volumes.

Subsequently, CO_2 (Airgas, >99.99%) and N_2 isotherms were found at 0 °C, utilizing ice baths for thermal control. Isothermal data was then taken in the range of P/P$_o$ = 0.05 to 1.0.

3.3 Histidine-derived porous carbons with seven activating agents

After determining that histidine-derived carbons have potential for CO_2 sequestration, a logical next step was to vary the activating conditions in which the porous carbon is produced. During the initial investigation KOH and NaOH were used as activating agents and tested across a variety of temperatures, times, and other variables. However, many compounds have been considered and applied towards the activation of porous carbon materials. These other chemicals each have their own sets of chemical activation processes when applied to produce PCMs.

Indeed, the diversity in chemistry between KOH and NaOH activation processes is quite minimal compared to the innate variety in chemicals that have been applied as activating agents. Common and classic activating agents, such as H_3PO_4, H_2SO_4, and $ZnCl_2$, are applied widely and their respective activation processes are thought to be somewhat understood. Though of course the nature of the carbon-containing precursor material plays an important role in the chemistry of activation. Still, many other chemicals are being applied, such as Na_2CO_3, $Na_2S_2O_3$, $KHCO_3$, or even NaCl, many of which are far more environmentally and economically sound.[8]

Previously discussed work in chapter 2 pertains to such a set of activated carbons. Several of these are activated with more classical activating agents (NaOH, KOH, H_3PO_4, $ZnCl_2$), and some are not (Na_2CO_3, $NaHCO_3$, K_2HPO_4). These same PCs, being already prepared and thoroughly characterized can serve as an excellent next step into the investigation of histidine related PCMs applied for CO_2 sequestration.

3.3.1 Textural analysis of activated histidine-derived porous carbons

Again, as all the textural and chemical characterization for this set of PCs has been thoroughly discussed in a previous chapter, a brief overview of their properties will be provided here. **Table 12.** These carbons provide a wide variety of SSA and micropore volumes. Additionally, there is one carbon with significant mesoporosity, though this is not typically considered beneficial regarding CO_2 capture.
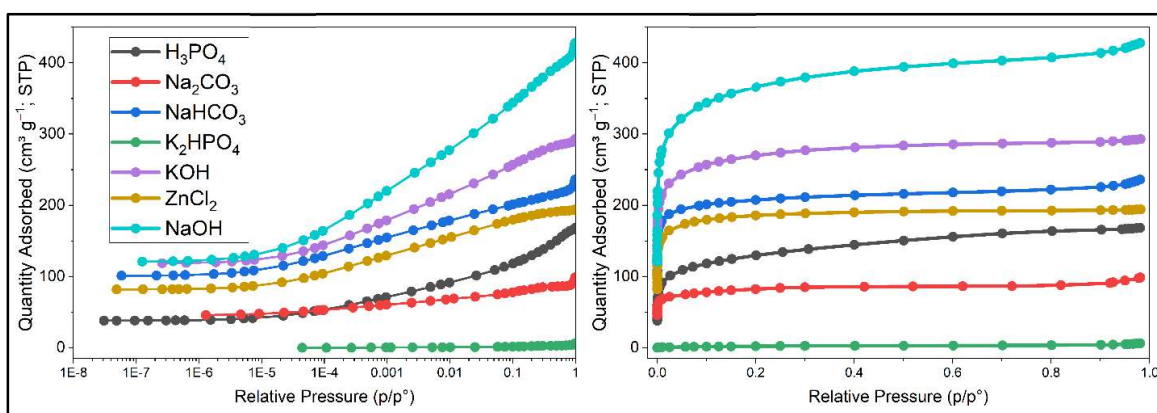
Figure 22. Gas adsorption analysis of histidine-derived porous carbons at 77 K with N2 set to log (a) and linear (b) scales that shows a wide distribution of porosity among the carbons.

The structural order of these carbons was investigated using Raman analysis and TEM imaging. Raman spectroscopy revealed that all carbons contained an I_D/I_G value greater than 1, suggesting that they have a disordered crystal structure. **Figure 5.** Furthermore, the values range from $I_D/I_G = 1.50 – 3.18$, which suggest a very high degree of disorder. TEM imaging reveals that all carbon materials contain disordered structure as well, though occasionally some potential regions of crystallinity can be seen on the scale of 1 nm. **Figure 7.** Altogether, these findings strongly support that these carbons range from amorphous to highly amorphous.

Activating agent	Gas adsorption analysis					Raman analysis
	BET	Total pore volume	t-plot	NLDFT	BJH	I_D/I_G
	characteristic surface area	$P/P° \geq 0.98$	micropore volume	micropore volume	mesopore volume	
	$cm^2\ g^{-1}$	$cm^3\ g^{-1}$	$cm^3\ g^{-1}$	$cm^3\ g^{-1}$	$cm^3\ g^{-1}$	
H_3PO_4	470.4	0.2600	0.1220	0.1640	0.58	3.18
Na_2CO_3	310.0	0.1530	0.1021	0.1172	-	2.77
$NaHCO_3$	813.3	0.3653	0.2834	0.2940	-	3.09
K_2HPO_4	7.5	0.0077	-	0.0018	-	1.77
KOH	1026.6	0.4533	0.3763	0.3788	-	2.18
$ZnCl_2$	723.3	0.3003	0.2595	0.2660	-	1.77
NaOH	1369.8	0.6620	0.4395	0.5022	-	1.50

Table 12. Summary of textural properties for histidine-derived porous carbon materials used in this study.

3.3.2 Chemical properties of the carbons

It is of course important to investigate (and revisit here) the chemical aspect of these porous carbons. As with the textural properties, only a brief overview of the chemical properties will be provided here, as a thorough analysis has been previously given. Emphasis will be given to properties that are commonly accepted to be critical to CO_2 capture, i.e., nitrogen content and type.

XPS was used to determine the atomic concentrations of the various carbons. **Figure 5.** It was determined that most of the produced carbons contain 70-78 % carbon, and 10-20 % nitrogen, and 6-15 % oxygen. **Table 13**. This is a relatively high heteroatom concentration and is possibly due in part to both the moderate activating temperatures used in this study (650 °C) and the fact that both nitrogen and oxygen are initially embedded

into the carbon structure of histidine. This last point would be in contrast to using a nitrogen dopant, such as urea, to try and incorporate non-native nitrogen into the carbon structure.

	Atomic Concentration					Boehm Titrations			pH$_{pzc}$
	C	N	O	P	Zn	Carboxyls	Lactones	Phenols	
Activating agent	%	%	%	%	%	mmol g^{-1}	mmol g^{-1}	mmol g^{-1}	approx.
_H$_3$PO$_4$_	26.14	2.34	51.62	14.21	--	0.542	0.411	0.650	3.3
_Na$_2$CO$_3$_	75.75	13.41	10.84	--	--	0.860	0.843	1.366	3.9
NaHCO$_3$	74.34	10.19	14.22	--	--	0.710	0.910	1.197	3.4
_K$_2$HPO$_4$_	77.49	15.18	6.48	0.43	--	0.166	0.150	0.042	6.8
KOH	70.97	12.65	13.87	--	--	0.908	0.970	1.53	4.2
ZnCl$_2$	72.66	17.17	8.52	--	0.7	1.324	0.363	1.533	2.5
NaOH	72.01	19.2	8.79	--	--	0.675	0.478	1.329	4.5

Table 13. Summary of chemical properties for histidine-derived porous carbon materials used in this study, including XPS atomic abundancies, approximate surface pH, and distribution of acidic functional groups.

Peak fitting the N1s analysis revealed the four typical nitrogen peaks found in porous carbon materials. **Figure 8**. These are pyridinic, pyrrolic, graphitic or quaternary, and oxidized, which correlated to eV values around 398.4, 400, 401, and 402.8, respectively. Overall, pyridinic and pyrrolic nitrogen comprised between 81.7 and 90.9% of the overall nitrogen content, except for H$_3$PO$_4$-HAC, whose nitrogen content contained approximately 35.2% graphitized nitrogen. **Table 14**. KOH- and ZnCl$_2$-HACs also contained 13.9 and 15.1% graphitic nitrogen, respectively, significantly higher than the remaining carbons (4.5 – 7.2%). The graphitic nitrogen content correlated well with the Raman G-band, suggesting that the graphitized nitrogen is influenced by the overall

graphitic character of the carbon. Oxidized nitrogen appears to have been present in low concentrations ($\leq 6.2\%$), regardless of the sample.

Carbon	N1s fine scan (%)			
	Peak 1	Peak 2	Peak 3	Peak 4
	398.4	400	401	402.8
	Pyridinic	Pyrrolic	Graphitic	Oxidized
H_3PO_4-HAC	34.9	23.7	35.2	6.2
Na_2CO_3-HAC	33.3	56.5	4.6	5.6
$NaHCO_3$-HAC	27.4	63.5	4.5	4.5
K_2HPO_4-HAC	49.0	41.7	4.6	4.8
KOH-HAC	36.0	46.0	13.9	4.2
$ZnCl_2$-HAC	45.5	36.2	15.1	3.1
NaOH-HAC	28.7	60.6	7.2	3.5

Table 14. XPS N1s data for histidine-derived porous carbons used in this study, detailing the relative abundancies of the types of nitrogen present.

3.3.3 Analysis of 0 °C CO_2 adsorption isothermal data

Comparing the CO_2 to the N_2 isotherms, several notes should be considered. **Figure 23**. First, all carbons preferentially adsorbed more CO_2 than N_2 under similar conditions. This is typical of porous carbons and is considered an outcome of 1) the operational temperature (which is much closer to the boiling point of CO_2 [-78.5 °C] than N_2 [-196 °C]), 2) the presence of a quadrupole in CO_2 that is much stronger than in N_2, leading to a smaller adsorbed state and stronger surface interactions, and 3) the possibility of functional groups that strongly and preferentially interact with CO_2. The second effect is most strongly felt in small micropores, such as ultra-micropores (those less than 0.7 nm in diameter).

The selectivity of CO_2 over N_2 was significant, but not constant throughout the samples. The selectivity, as indicated by the relative amounts of CO_2 and N_2 adsorbed at 0 °C and 760 mmHg was similar with most of the carbons adsorbing around 9 times as much CO_2 as N_2. The outliers being K_2HPO_4 and $ZnCl_2$, who adsorbed 6.54 and 10.2 times as much CO_2 as N_2, respectively.
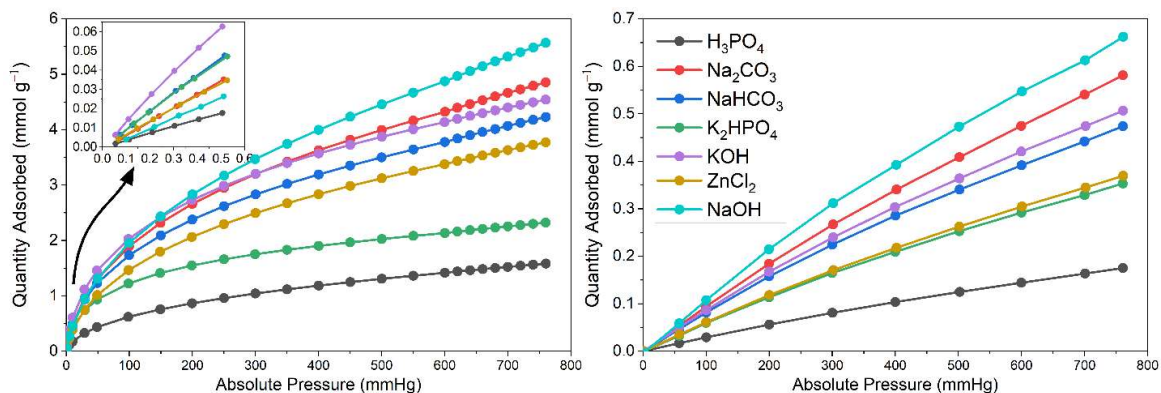
Figure 23. CO_2 (a) and N_2 (b) isotherms for the histidine-derived porous carbons used in this study, collected at 0 °C, showing the enhanced uptake in these materials for CO_2.

There could be several causes for this variation in selectivity. As already mentioned, several factors come into consideration when adsorbing CO_2, such as the types of pores and active sites. In general, any chemisorption process with adsorbates either strongly or weakly bound to the surface results in uptake of CO_2 at low pressures. In an isotherm this typically reflects an immediate uptake followed by a levelling out region as the pressure continues to increase. In contrast, physisorption processes result in isotherms that continuously increase in quantity adsorbed, though this increase is slows significantly as pore filling occurs (from smallest to largest). However, if small micropore filling exclusively occurs, the resultant isotherm can still appear like chemisorption, though this

doesn't level off to quite the same extent. Of course, when multiple mechanisms occur an isotherm can become difficult or impossible to fully deconstruct.

The isotherms produced for the PCs here suggest the presence of different uptake mechanisms being more prevalent in different carbons. For example, the isotherm of K_2HPO_4 suggests that chemisorption or the filling of ultra-micropores is primarily occurring. In contrast, the isotherms for Na_2CO_3 and NaOH appear to be highly influenced by physisorption, as they are still increasing significantly, even as the absolute pressure reaches 1 atm.

	Quantity adsorbed at 760 mmHg, 0 °C		Selectivity	Quantity adsorbed at 25 °C	
	CO_2 mmol g^{-1}	N_2 mmol g^{-1}	CO_2/N_2	100% CO_2 mmol g^{-1}	500 PPM mmol g^{-1}
H₃PO₄	1.58	0.175	9.04	0.556	0.304
Na₂CO₃	4.86	0.581	8.35	1.56	0.600
NaHCO₃	4.23	0.474	8.92	1.57	0.458
K₂HPO₄	2.32	0.353	6.58	0.941	0.720
KOH	4.54	0.507	8.96	1.68	0.889
ZnCl₂	3.77	0.370	10.2	1.67	0.299
NaOH	5.57	0.662	8.41	1.77	1.03

Table 15. Summary of gas adsorption analysis and TGA data for CO_2 and N_2 at 0 and 25 °C.

Perhaps the most surprising result is the CO_2 uptake of K_2HPO_4 activated carbon, which contains incredibly poor SSA and porosity compared to the other carbons, yet captured a significant quantity of CO_2. Given the poor surface area and porosity of K_2HPO_4 activated histidine, it is not surprising that the isotherm suggests chemisorption as a key

player in the CO_2 uptake here. It is often assumed that good surface area and porosity are key to for most carbon capture technologies, yet this carbon is clearly not reliant upon that trend as it was able to uptake 2.32 mmol g^{-1} of CO_2 on only ~7.5 m^2 g^{-1}. One important result of this, is that when correlations are made, K_2HPO_4 is a strong outlier. **Tables 16 and 17.**

It seems more important here to solely consider the carbon's nitrogen content, which was the second highest out of the set. Additionally, the nitrogen content of this carbon was almost entirely ascribed to aromatic groups, with ~90.7% of the N_2 being pyridinic or pyrrolic, which are often considered the most important of the common nitrogen types in PCMs for CO_2 capture.

Correlator		R² values				
		GAA – 0 °C			TGA – 25 °C	
		CO_2	N_2	CO_2/N_2	100% CO_2	500 PPM CO_2
Gas adsorption analysis	SSA	0.45	0.29	0.24	0.42	0.20
	TPV	0.41	0.28	0.20	0.33	0.22
	T-plot MPV	0.49	0.32	0.26	0.51	0.20
	NLDFT MPV	0.47	0.31	0.24	0.44	0.21
Raman	I_D/I_G	0.10	0.13	0.04	0.16	0.32
pH_{pzc}		0.03	0.01	0.92*(N)	0.07	0.34
Boehm Titrations	Carboxyl	0.21	0.05	0.77	0.41	0.07
	Lactones	0.33	0.23	0.10	0.27	0.02
	Phenols	0.50	0.32	0.56	0.67	0.01
	sum groups	0.50	0.25	0.57	0.60	0.00
XPS - atomic concentration (%)	C	0.41	0.49	0.06	0.54	0.20
	N	0.42	0.47	0.02	0.52	0.30
	O	0.40	0.48	0.05	0.54	0.23
XPS - N	Pyridinic	0.28	0.24	0.05	0.10	0.05
	Pyrrolic	0.67*	0.77*	0.03	0.51	0.27
	Graphitic	0.39	0.55	0.18	0.39	0.24
	Oxidized	0.28	0.19	0.09	0.53	0.11
XPS - O	O=C, P	0.29	0.25	0.05	0.16	0.00
	O-H, C, N or C-O-C	0.04	0.06	0.05	0.10	0.28
	O-C=O	0.82 (N)	0.83 (N)	0.00	0.81*(N)	0.41
XPS - C	C=C	0.00	0.00	0.05	0.03	0.22
	C-C,N,O,P	0.39	0.27	0.13	0.41	0.00
	C-O-C	0.16	0.27	0.18	0.06	0.84*(N)
	C=O,N or O-C=O	0.01	0.00	0.24	0.08	0.24

Table 16. Coefficients of determination across the set of carbons for adsorption of CO_2 and N_2 compared to the textural and chemical properties of the carbons. *Most important determined correlation for column (considers both value and slope of correlation). For correlations above 0.7, H and N denotations refer to horizontal and negative correlations, respectively.

Correlator		R² values				
		GAA – 0 °C			TGA – 25 °C	
		CO_2	N_2	CO_2/N_2	100% CO_2	500 PPM CO_2
Gas adsorption analysis	SSA	0.29	0.26	0.01	0.28	0.54
	TPV	0.25	0.24	0.04	0.18	0.57
	T-plot MPV	0.35	0.29	0.00	0.40	0.52
	NLDFT MPV	0.32	0.28	0.01	0.31	0.56
Raman	I_D/I_G	0.34	0.25	0.04	0.44	0.30
pH_{pzc}		0.35	0.48	0.74*(N)	0.08	0.84*
Boehm Titrations	Carboxyl	0.04	0.00	0.53	0.27	0.05
	Lactones	0.17	0.19	0.20	0.13	0.11
	Phenols	0.41	0.44	0.03	0.87	0.18
	sum groups	0.41	0.29	0.04	0.69	0.07
XPS - atomic concentration (%)	C	0.79	0.67	0.00	0.94*	0.18
	N	0.71	0.59	0.00	0.81	0.29
	O	0.81(N)	0.67	0.00	0.97 (N)	0.21
XPS - N	Pyridinic	0.11	0.20	0.69 (H)	0.00	0.21
	Pyrrolic	0.73*	0.77*	0.32	0.53	0.32
	Graphitic	0.82 (N)	0.78	0.11	0.76 (N)	0.22
	Oxidized	0.32	0.19	0.18	0.60	0.12
XPS - O	O=C, P	0.17	0.20	0.10	0.06	0.00
	O-H, C, N or C-O-C	0.14	0.11	0.00	0.24	0.26
	O-C=O	0.88 (N)	0.82 (N)	0.11	0.85 (N)	0.49
XPS - C	C=C	0.00	0.01	0.15	0.03	0.22
	C-C,N,O,P	0.25	0.22	0.02	0.29	0.03
	C-O-C	0.28	0.34	0.32	0.11	0.84 (N)
	C=O,N or O-C=O	0.00	0.01	0.42	0.06	0.23

Table 17. Coefficients of determination across the set of carbons (excluding K_2HPO_4-HAC) for adsorption of CO_2 and N_2 compared to the textural and chemical properties of the carbons. *Most important determined correlation for column (considers value and slope of correlation). For correlations above 0.7, H and N denotations refer to horizontal and negative correlations, respectively.

Beyond K_2HPO_4 activated histidine, several other carbons appear to be highly influenced by physisorption processes in addition to chemisorption. All CO_2 isotherms can be interpreted to have some chemisorption occurring. However, for some carbons, particularly the higher achieving PCs, there appears to be considerable physisorption occurring simultaneously. Yet, when attempting to identify strong correlations between the properties of the PCs and their ability to adsorb CO_2, textural properties are noted to have poor association. **Tables 16 and 17.** In fact, the best positive correlation with CO_2 uptake comes from increased pyrrolic nitrogen content, which is a trend that has been noted in literature. **Figure 24.** Interestingly, pyridinic nitrogen shows a negative correlation in the collected data.

The best correlation overall for the CO_2 uptake at 0 °C was a negative correlation between oxygens associated with a carboxyl group. While no direct conclusion can be determined for why this correlation exists, it is possible it could be related to the strong positive correlation between the pH_{pzc} and the CO_2/N_2 selectivity. This suggests that as the pH increases, the carbon's preference for CO_2 over N_2 increases, and acidic carboxyl groups could be attributing to this effect (or vice versa).

It is curious that these same correlations are also found for N_2 uptake, despite there being no expected interaction between either pyrrolic-N or carboxylic groups and N_2. Indeed, one would expect that given N_2's chemically inert nature, the best correlation for N_2 uptake would be with textural properties associated, especially those associated with SSA and PV_{micro}. Still, it is very possible that is simply a consequence of the small sample size.
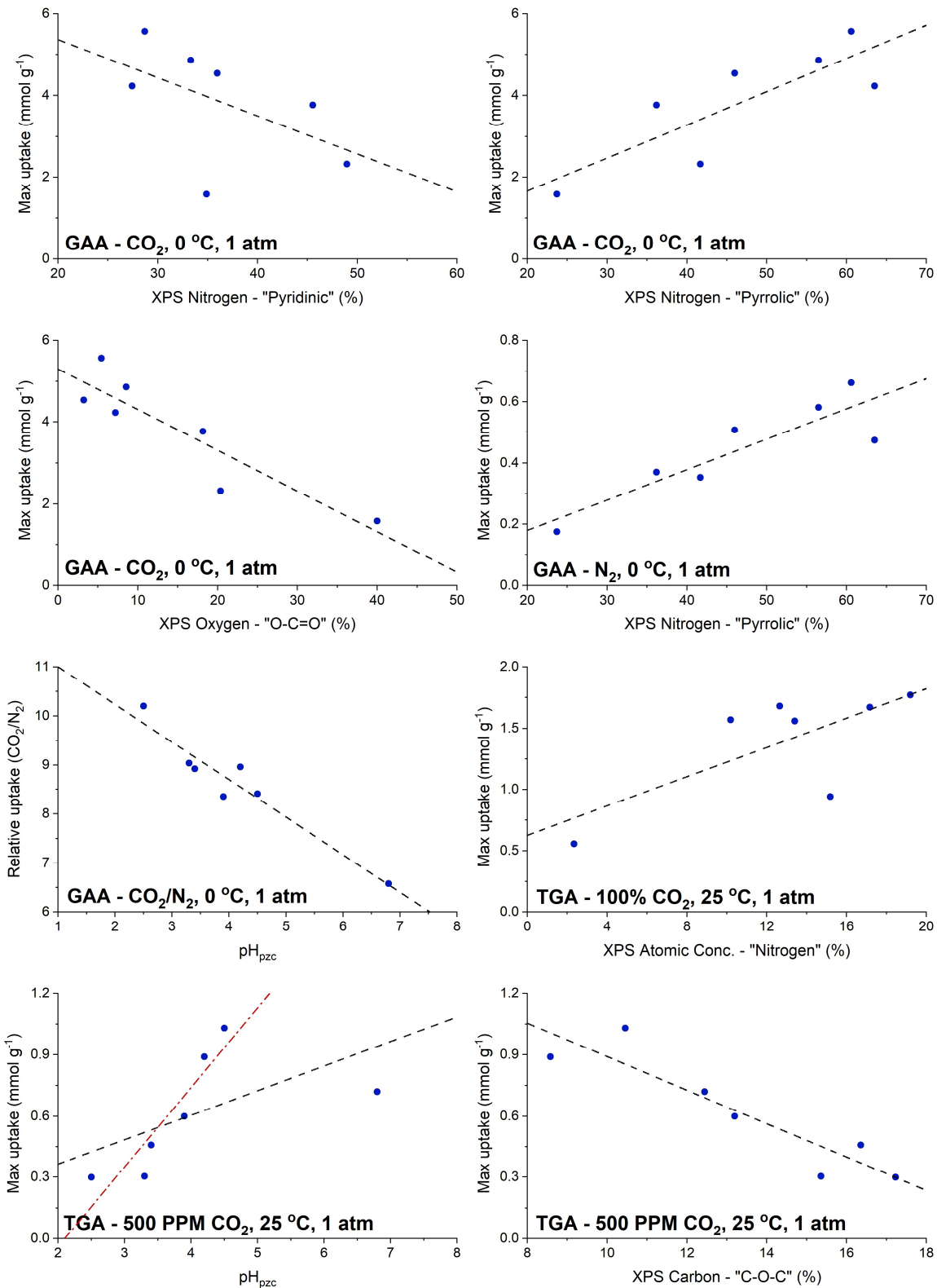
Figure 24. Select correlations of gas adsorption data for histidine-derived carbons with properties of the carbons.

105

Regardless of the reliability of the correlations, it can be clearly seen that high quantities of CO_2 were able to be captured by histidine-derived porous carbons. **Figure 24.** NaOH activated histidine was the highest achieving adsorbent with a max capacity of 5.57 mmol g^{-1} at 0 °C and 1.77 mmol g^{-1} at 25 °C. However, histidine activated with both alkali hydroxides and carbonates were all high achieving with the lowest, that being histidine activated with sodium bicarbonate (NaHCO$_3$), capturing 4.23 mmol g^{-1} at 0 °C. Of some interest is that although both carbonate-activated histidine's outperform ZnCl$_2$ activated histidine at 0 °C, ZnCl$_2$ captures the third most CO_2 at 25 °C (1.67 mmol g^{-1}), just behind KOH-activated histidine with 1.68 mmol g^{-1}.

Of particular interest is the capture capacity of these materials at atmospheric concentrations of CO_2. Thermogravimetric analysis suggests that several of these carbons can transiently adsorb significant quantities of CO_2. **Figure 25.** Again, NaOH-activated histidine was able to capture the largest quantity, at just over 1 mmol g^{-1}. Furthermore, it was able to capture this quantity of CO_2 at 500 PPM concentrations in under 8 minutes.
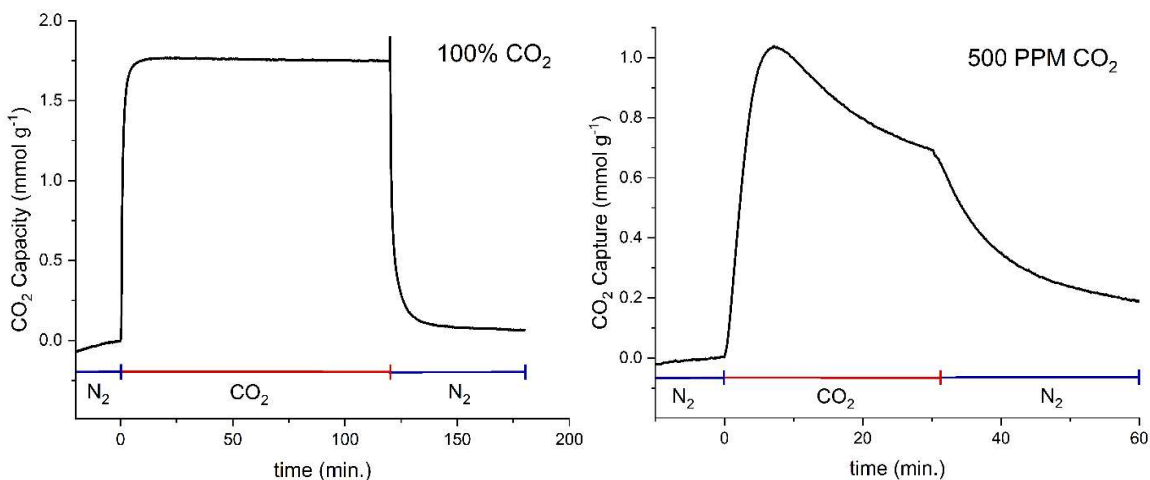
Figure 25. CO_2 capture isotherms for NaOH-activated histidine at 25 °C under both 100% and 500 PPM CO_2, suggesting the retention of much of the capture capacity even at low concentration, although an uninvestigated dynamic capture mechanism is also present.

However, despite this promising outlook, there is some worthwhile skepticism to be discussed. To begin, while the shape of the 100 % CO_2 run on the TGA is as one would expect, the 500 PPM run is completely unexpected. Indeed, it is completely possible that the initial uptake is not due to CO_2 uptake, but rather the uptake of any gas via physisorption processes, such as a temporary pressure gradient across the microporous channels due to the uptake of CO_2 before N_2 could be expelled or localized cooling of the carbon (adsorption is an exothermic process) leading to a temporary increase in capture capacity before reattaining thermal equilibrium with the flowing gas. Still, this is a promising start, and warrants further evaluation. For example, the evaluation of the CO_2 uptake by examining the outgas, such as in a flow-through apparatus, would be highly beneficial, as this could more directly measure the uptake of CO_2 and miscellaneous physisorption effects.

3.3.4 Conclusion

Overall, it was shown here that these activated materials can capture significant quantities of CO_2 (up to 5.77 and 1.03 mmol g^{-1} at 0 °C, 100% CO_2 and 25 °C, 500 PPM CO_2, respectively), and that this capture capacity is suspected to have a strong relationship with the chemical nature of the surface of the materials. Of note were trends found that suggest that while overall nitrogen content is linked to increased CO_2 capture, more specifically pyrrolic nitrogen appeared to have the best overall correlation. Additionally, it was found that the more acidic the surface, the lower capacity, a trend which may or may

not be directly related to increased carboxylic groups on the surface. Unexpectedly, no good trend was found between the SSA or PV_{micro} and CO_2 uptake.

Further work should be performed to increase the confidence of these findings. As previously discussed, this is a relatively small dataset (n = 7), and more data should be considered before relying upon the trends found here. Similarly, the inclusion of data from similar precursor materials should also be considered to determine if the findings here can be seen as universal trends for these types of materials. Moreover, for the interpretation of some of the CO_2 uptake data, such as the 500 PPM CO_2 datasets, direct measurements of the CO_2 concentration in the effluent gas could result in more reliable data.

3.3.5 Materials and Methods

Materials

All materials were used as purchased without further purification or alteration. L-Histidine HCl monohydrate ($\geq$ 99%), potassium hydroxide, sodium hydroxide ($\geq$99.8%), anhydrous $ZnCl_2$ ($\geq$98%), concentrated o-phosphoric acid, sodium carbonate anhydrous, and sodium bicarbonate were all purchased through Fisher scientific (Fair Lawn, NJ).

Preparation of porous carbons

All ACs in this study were prepared from the precursor L-histidine HCl with an activating agent (AA) in a 1:7 (His:AA) molar ratio. Activating conditions and ratios were selected based upon previous studies, preliminary analysis, and a need to keep some

simplicity in this study. Activating agents used in this study include KOH, NaOH, H_3PO_4, Na_2CO_3, $NaHCO_3$, K_2HPO_4, and $ZnCl_2$. The tube furnace used for AC synthesis was an across international STF1200 with a 4 in. ceramic tube. The synthesis procedure begins by grinding carefully measured amounts of precursors using a mortar and pestle until homogenous. Next the mixture was transferred to a ceramic boat, placed at the center of the furnace tube and sealed in. The heating process consisted of heating to 100 °C for one hour, followed by ramping to 650 °C and holding that temperature for two hours. The ramping rate was 10 °C min^{-1} and the nitrogen flow rate set to 200 mL min^{-1}. Activated materials were then allowed to cool naturally and were preliminarily rinsed with around 500 mL of ultrapure water before being added to 1 L of 0.1 M HCl solution (except for H_3PO_4 activated His which was added to 0.1 M NaOH) and stirred for 24 hours. Next, samples were filtered and rinsed with ultrapure water until the eluent reached neutral pH. The samples were then dried at 100 °C for ≥ 12 hours prior to characterization or use.

Characterization of porous carbons

Gas adsorption analysis (ASAP 2020, Micromeritics) with nitrogen (Airgas, > 99.999%) at 77 K was used to define total surface area and pore volume, as well as probe the pore structure. Additionally, CO_2 (Airgas, > 99.99%) and N_2 isotherms were found at 0 C. All resulting data was analyzed using Micromeritics ASAP 2020 Plus software, version 2.00. The single point total pore volume was determined at relative pressures of ≥ 0.985 P/P°. Brunauer-Emmett-teller (BET) theory was used in conjunction with a Rouquerol BET plot to determine the total surface area of the carbons. The t-plot method, using the carbon black STSA statistical thickness equation, was used to determine

micropore volume. NLDFT using a kernel for N_2 at 77 K on carbon black slit pores was used to determine micropore size and pore volumes.

Thermogravimetric analysis (Q50, TA instruments) under nitrogen and air was used to look at the synthesis of the carbons, as well as determine thermostability of the carbons. Synthesis analysis was performed by combining precursors in the same manner as during regular synthesis, then around 5-15 mg of the mixture is placed on a clean, tared pan for analysis. Analysis was performed under nitrogen at 65 mL min^{-1} and all ramping rates were 10 °C min^{-1}. The procedure then consisted of heating to 100 °C for 1 hour, then ramping to 650 °C and holding the temperature for 2 hours. It is worth noting that the internal temperature of this oven might vary when compared to the tube furnace used during synthesis, due to differences in the structure of the furnace and placement of the thermocouples. Thermostability of the final, rinsed and dried carbon material was also tested under both nitrogen and air at 65 mL min^{-1} using 5-15 mg of sample. The temperature was ramped at 10 °C min^{-1} to 900 °C, starting from room temperature.

The pH at zero charge (pH$_{zc}$) was determined based on literature precedent (cite). The process consisted of first adjusting ultrapure water to a series of different pH's (2, 3, 4, 6, 8, and 10) using stock NaOH and HCl solutions, followed by pipetting 20 mL of each solution into a series of small scintillation vials. The initial pH of each vial was then taken and subsequently 10 mg of AC was added. The suspension was then stirred for 24 hours before the pH was again tested. The pH$_{zc}$, is the pH at which point initial pH – final pH = 0. Plotted initial pH versus final pH, this where the series crosses the line y = x.

Scanning electron microscopy (SEM) was performed on a Scios Analytical Dualbeam.

Transmission electron microscopy (TEM) was performed using a FEI Tecnai F30 Twin 300kV TEM. A Formvar/Carbon 400 mesh, Copper was used as the support for analysis.

Elemental analysis was performed using X-ray photoelectron spectroscopy (XPS) with a Physical Electronics 5000 VersaProbe II Scanning ESCA Microprobe.

3.4 Silica templated porous carbons from histidine

As a bridge into the following chapter, let us take an aside to another type of porous carbon production: templating. Specifically, templating with mesoporous silicas. This templating material will be discussed in detail in the following chapter, and so only a brief summary will be given here. These materials are comprised primarily of silica (silicon and oxygen) though occasionally residual dopants might be found as well. Mesoporous silicas most often have pores ranging from 1 – 40+ nanometers, fully spanning the mesoporous range and beyond. Ordered porous silicas, are generally produced by either cooperative self-assembly or true liquid-crystal templating.[115] After, their (often organic) templating agent is burned off in open air.

Mesoporous silicas are useful for templating carbons because they are capable of withstanding high temperature without morphological changes and can be dissolved away by treatment with HF or strong base solutions. Therefore, porous carbon precursor can be infused within prepared mesoporous silica, carbonized, then the silica template can be removed. Thus, mesoporous silica templating can lead to hierarchical structures wherein porous characteristics relating to the carbon structure and the mesoporous silica can both be present.[116]

This can be advantageous when considering kinetics and/or transporting larger species into the porous structure. **Fig. 26**. For example, adsorbate species with dimensions near to the pore micropore dimensions in the adsorbent tend to diffuse more slowly than adsorbate species much smaller than the pore size. Thus, penetrating deep within a carbon

particle along purely microporous pathways can be a lengthy process for certain compounds. However, the addition of mesoporous channel can lead to a faster distribution to more of the microporous network. With more of the microporous network being rapidly accessible, the slower micropore diffusion can occur more frequently and the pathway is on average reduced in length.

Furthermore, these larger mesoporous channels can lead to a decrease in pore-blocking affects, where a microporous channel becomes inaccessible due to an adsorbate reaching an insurmountably small region of the pore. This of course will still occur in hierarchical structures, but the number of 'entry points' into the microporous channels will be increased, which can lead to the avoidance of these blocked pathways.

It should be noted that the silica's own porous structure is not expected to be retained, but rather used as the mould for the carbon product to be pyrolyzed within.
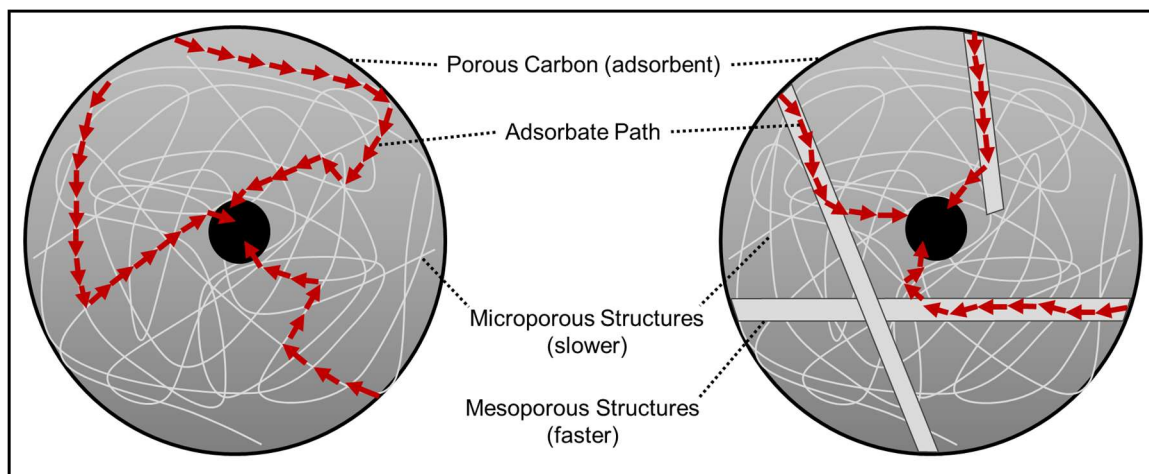
Figure 26. Descriptive illustration of the adsorption process in a purely microporous carbon, compared to a hierarchical mesoporous and microporous carbon.

3.4.1 Examining the effect of templating on the surface area and porosity of histidine-derived carbons

For this work we incorporated the two silicas ISM-01C and SBA-15, both made in house. Gas adsorption analysis (GAA) was used to analyze the materials. **Figure 27.** The first, ISM-01C, contains a very high BET specific surface area (SSA) of 909 m^2 g^{-1}, and has a multimodal pore size distribution (PSD) focused primarily around 30 nm with a smaller pore volume associated with 3-4.5 nm pores, and smaller yet associated with 1.8-2.6 nm pores. **Table 18.** With around 83% of the total pore volume being associated with the larger pores, it is assumed that these primary pores will be the foundation of the carbon's overall structure.

The SBA-15 like silica used contained a BET SSA of 765.8 m^2 g^{-1}. The PSD for this silica had shows some borderline micropores, but the bulk of the porosity centers around a sharp peak around 5 nm. Thus, although both silica templates should contain a similar overall structure, the SBA-15 and ISM-01C should provide a variety of scales that allows for a good comparison as porous carbon templates.
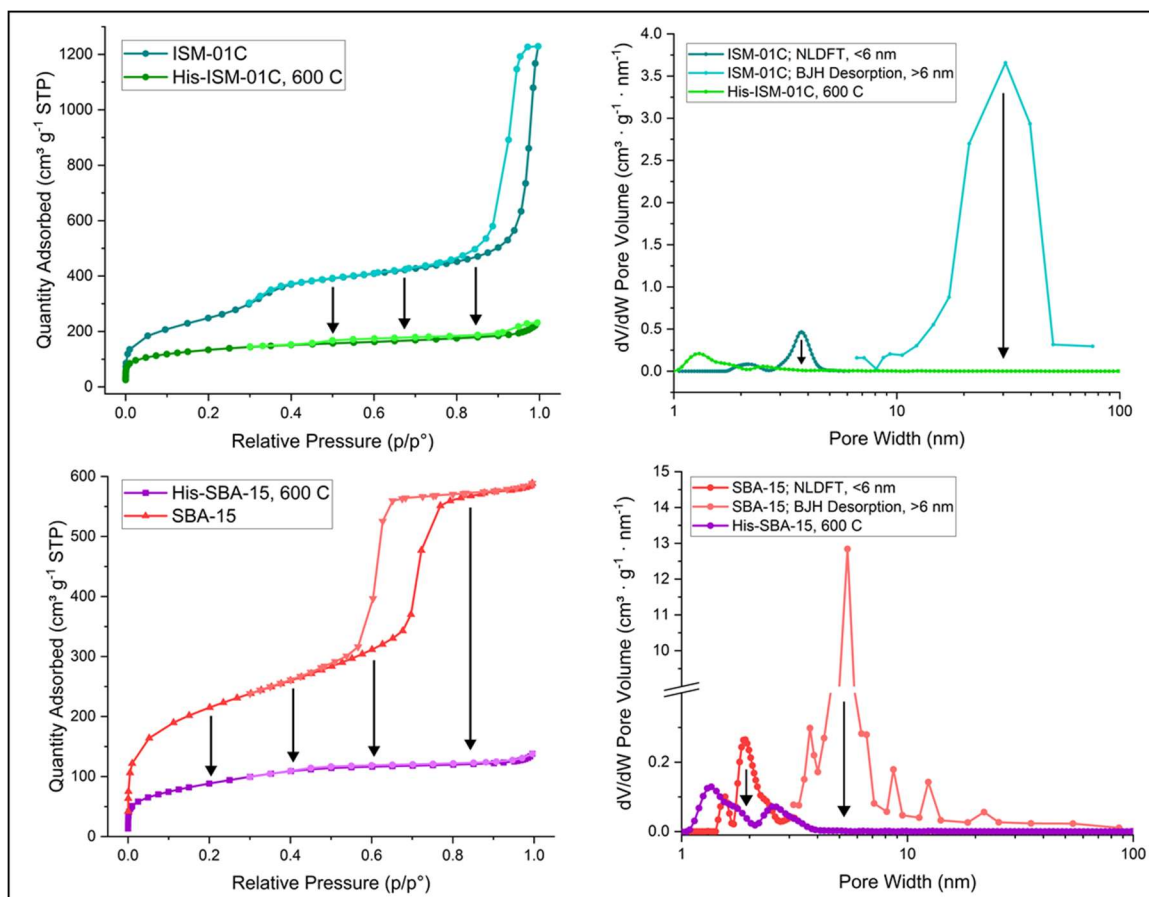
Figure 27. Isotherms collected with N_2 at 77 K (a, c) and pore size distributions (b, d) for both silicas and their respective templated porous carbons, which show that the porous properties of the template do not directly transfer to the final material.

	BET SSA	PV_{Micro}	PV_{Meso}	PV_{Total}
	$m^2 g^{-1}$	$cm^3 g^{-1}$	$cm^3 g^{-1}$	$cm^3 g^{-1}$
His-600	0.5	-	-	-
ISM-01C	909.5	-	1.7	1.7
His-ISM-01C	483.1	0.159	0.161	0.32
SBA-15	765.8	0.066	0.808	0.874
His-SBA-15	320.9	0.096	0.093	0.189

Table 18. Summary of textural properties for both silica and porous carbons used in this study.

The porous carbons (PCs) were shown to have substantially increased the SSA and porosity of pyrolyzed histidine. Alone, histidine pyrolyzed at 600 °C provides a very small SSA (0.5 m^2 g^{-1}). Yet both silica templates were shown to provide significant SSA (483.1 and 320.9 m^2 g^{-1} for ISM-01C and SBA-15 templated silicas. As expected, the pore size distribution from the silicas was not retained during the templating process, and the PSD for the PCs was shown to be primarily microporous, with some very small mesopores also being present.

Interestingly, GAA the pore structure was very similar between the two PCs, despite the silicas having such large differences in pore structure. One possible method for the development of these pores could be that the pores are related of the thickness of the silica pore walls. However, several issues arise with this method's candidacy. First, this would indicate a degree of uniformity between the two silicas that might not be expected. Moreover, this would most likely result in non-rigid particles and the isotherms of the resultant carbons would then be of type H3 yet type H4 is observed. **Fig. 28.**
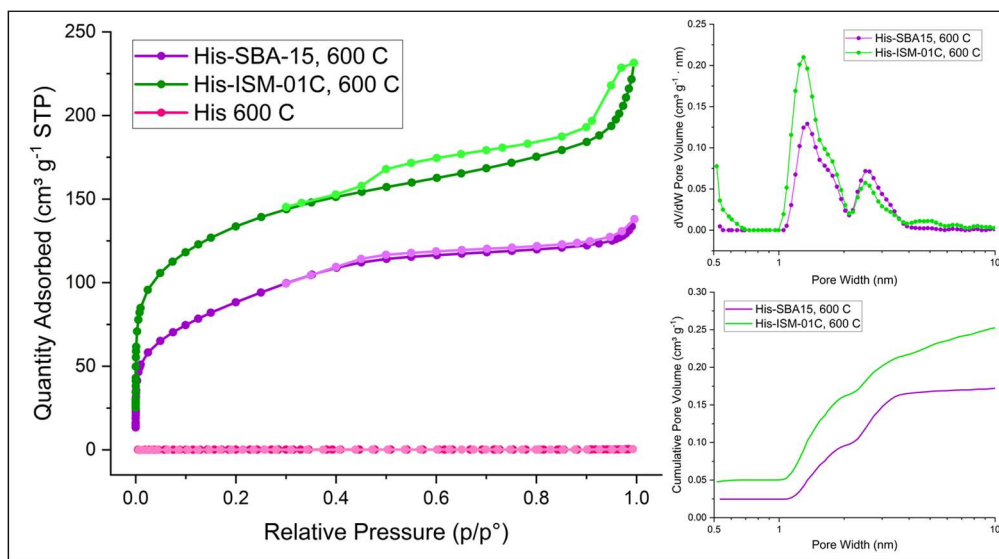
Figure 28. Isotherms collected with N_2 at 77 K for histidine-derived porous carbons (a), along with their respective pore size distribution plot (b) and cumulative pore volumes (c), which demonstrate the effect of templating-alone to improve porosity in the final material.

Another possibility for this could be that pore development lies primarily in the histidine pyrolysis chemistry. Given the lack of SSA and porosity exhibited for histidine carbonized alone, this would imply that the pyrolysis of histidine is affected by pyrolysis occurring inside the silica pores. A third, related possibility is an interaction between the silica walls and the histidine precursor. Indeed, the development of C-Si composites has been applied for nano-porous materials.[116-118] Further examination into the Si-C interactions and the transfer of silica to the carbon structure should be investigated.

3.4.2 Uptake of CO_2 in non-activated mesoSi-templated porous carbons

Despite the exceptional increase in textural characteristics, application of these materials for CO_2 capture proved less than exceptional. S15C templated histidine was able to increase the capacity of CO_2 to 1.47 mmol g^{-1}, a 25% increase when compared to the

non-porous His-600 that captured 1.18 mmol g^{-1} CO$_2$. **Figure 29.** However, a 10% decrease in capacity was observed for the carbon templated with ISM-01C, which captured 1.06 mmol g^{-1} of CO$_2$. It is clear that the 150,000% and 180,000% increases in SSA for S15C and ISM-01C templated his is not effective at increasing capture capacity.
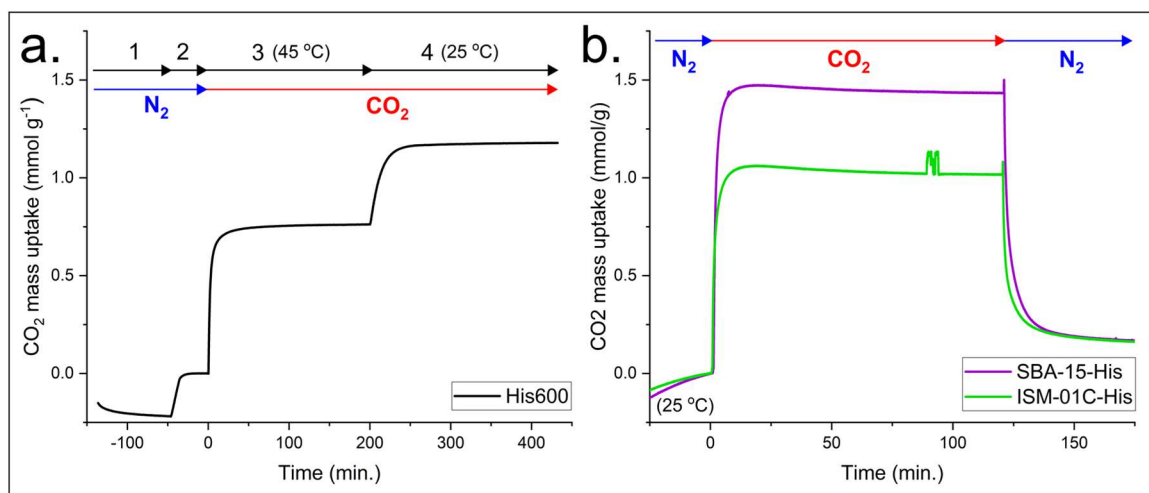
Figure 29. Thermogravimetric analysis examining the CO$_2$ capture of untemplated (a) and templated (b) carbons. The three-step analysis includes degassing at 90 °C (a.1), thermal equilibrium at analysis temperature (a.2), and switching gas flow to CO$_2$ (a.3). Optionally, the temperature can be reduced for continued analysis at a separate temperature (a.4).

One possibility for this unexpected result is that CO$_2$ can penetrate inside pores that are too small to be accessible to N$_2$ during GAA. This is based on the CO$_2$ having a slightly smaller liquid-like state than N$_2$ when adsorbed onto the surface, thanks to a stronger quadrupole.[119] However, diffusion into such pores tends to be very slow, and the uptake of CO$_2$ here was rapid.

It seems more likely that this CO$_2$ capture potential is tied to residual nitrogen moieties located on the surface of the carbon particle. GAA analyzing CO$_2$ adsorption at 0, 25, or 45 °C would be very useful for identifying whether chemisorption or physisorption is the principal source of CO$_2$ adsorption occurring.

118

It is possible that post-carbonization treatment of the carbons led to a decrease in the capture capacity. To remove the silica, the carbon was required to soak in a corrosive strong base solution. Even though carbons are generally regarded as having good chemical and thermal stability, it is possible that a reaction took place between the surface amine groups and the strong base or even dissolved silica. Again, more study is required to fully understand a lack of any significant increase in capacity. Additionally, another form of silica dissolution could be tried, such as with HF.

3.4.3 Materials and Methods

Histidine HCl monohydrate ($\geq$ 99%) were purchased through Fisher scientific (Fair Lawn, NJ). Tetraethyl orthosilicate (TEOS), poly (ethylene glycol)-block-poly (propylene glycol)-block-poly (ethylene glycol) (P_{123}, M = 5800 g mol^{-1}), citric acid, Cetyltrimethylammonium bromide (CTAB), ammonium hydroxide, and NaOH (> 99%) were all purchased through Sigma-Aldrich (St. Louis, MO).

Synthesis of the Materials

The silica S15C, a SBA-15-type mesoporous silica, was produced as described in literature.[120] Briefly, calculated quantities of TEOS, citric acid, and P_{123} were mixed and heated gently for 24 hours. After, the mixture was placed in a Teflon-lined stainless-steel autoclave and heated at 100 °C for 24 h. Last, the final product was calcined at 550 °C in air to remove the organic template.

The silica ISM-01C, a pore expanded MCM-41-type mesoporous silica, was produced as described in literature.[121] Briefly, an amount of CTAB was dissolved completely in water and allowed to stir for about an hour. Then, TEOS was added, and the mixture was allowed to stir for a further 15 minutes. Afterwards, 1 mL of aqueous ammonium hydroxide was added dropwise, and the reaction beaker was covered. The mixture was allowed to stir at room temperature for until the gel formed, solidified, and dried. The material was then recovered, washed in ultrapure water, calcined at 550 C, and ground in a mortar/pestle.

The porous carbons were produced by the following method. First, a 1:1 mass ratio of histidine to porous silica was combined in a falcon tube with just enough water to fully dissolve the histidine. The tube was then inverted for 24 hours before freeze drying to collect a uniform, fine, white powder. Next the mixture was transferred to a ceramic boat, placed at the center of a furnace tube and sealed in. The tube furnace used for AC synthesis was an across international STF1200 with a 4 in. ceramic tube. The heating process consisted of heating to 100 °C for one hour, followed by ramping to 650 °C and holding that temperature for two hours. The ramping rate was 10 °C min^{-1} and the nitrogen flow rate set to 200 mL min^{-1}. After, the materials were allowed to cool naturally and were preliminarily rinsed with around 500 mL of ultrapure water before being added to 500 mL of 1 M NaOH. This solution was agitated for 24 hours while the porous silica was dissolved. Finally, the product was rinsed off with DI until the pH of the eluent was neutral.

Analysis of the materials

Gas adsorption analysis (ASAP 2020, Micromeritics) with nitrogen (Airgas, > 99.999%) at 77 K was used to define total surface area and pore volume, as well as probe the pore structure. Additionally, CO_2 (Airgas, > 99.99%) and N_2 isotherms were found at 0 C. All resulting data was analyzed using Micromeritics ASAP 2020 Plus software, version 2.00. Brunauer-Emmett-teller (BET) theory was used in conjunction with a Rouquerol BET plot to determine the total surface area of the carbons. The t-plot method, using the carbon black STSA statistical thickness equation, was used to determine micropore volume. NLDFT using a kernel for N_2 at 77 K on carbon black slit pores was used to determine micropore size and pore volumes.

Carbon capture experiments were performed in the TGA. Generally, this consists of four parts, which include: 1) initial outgassing at elevated temperature (90 °C) under inert gas (N_2), 2) equilibration at desired temperature (25/45 °C), 3) gas exchange to adsorbate (CO_2), and 4) gas exchange to N_2 for desorption step. An additional step can be included if two analysis temperatures are desired, given that the lower temperature comes second.

4. Capturing CO2 using loaded nano-porous silica

4.1 Introduction to porous silica materials

Nanoscale materials have found many applications in today's world and as such continue to be heavily investigated. As such units of intensive study, they have been produced from a wide variety of components, often comprising of few or just one atomic species. One such type of nanomaterial are porous silicas, comprised of silicon and oxygen, with an occasional dopant depending on the researcher's intent.

Ordered porous silicas can have a variety of pore sizes ranging from macroporous (> 40 nm), mesoporous ($40 - 2$ nm), and microporous (< 2 nm). Likewise, these silicas also come in a variety of shapes such as an array of 2D hexagonal shafts, as with SBA-15, or 3D cage-like porous structures, as with KIT-6. Possibly the most common ordered porous silica is the Mobile Composition of Matter No. 41, more commonly referenced as MCM-41. This is, in effect, like SBA-15, as it is comprised of an array of 2D hexagonal shafts that are generally uniform in size and typically smaller than those of SBA-15. Ordered porous silicas are generally produced by either cooperative self-assembly or true liquid-crystal templating.[115]

We have successfully produced and characterized many different porous silica materials. **Figure 30.** This is evidenced by isothermal data collected that has revealed a wide variety of porous structures.
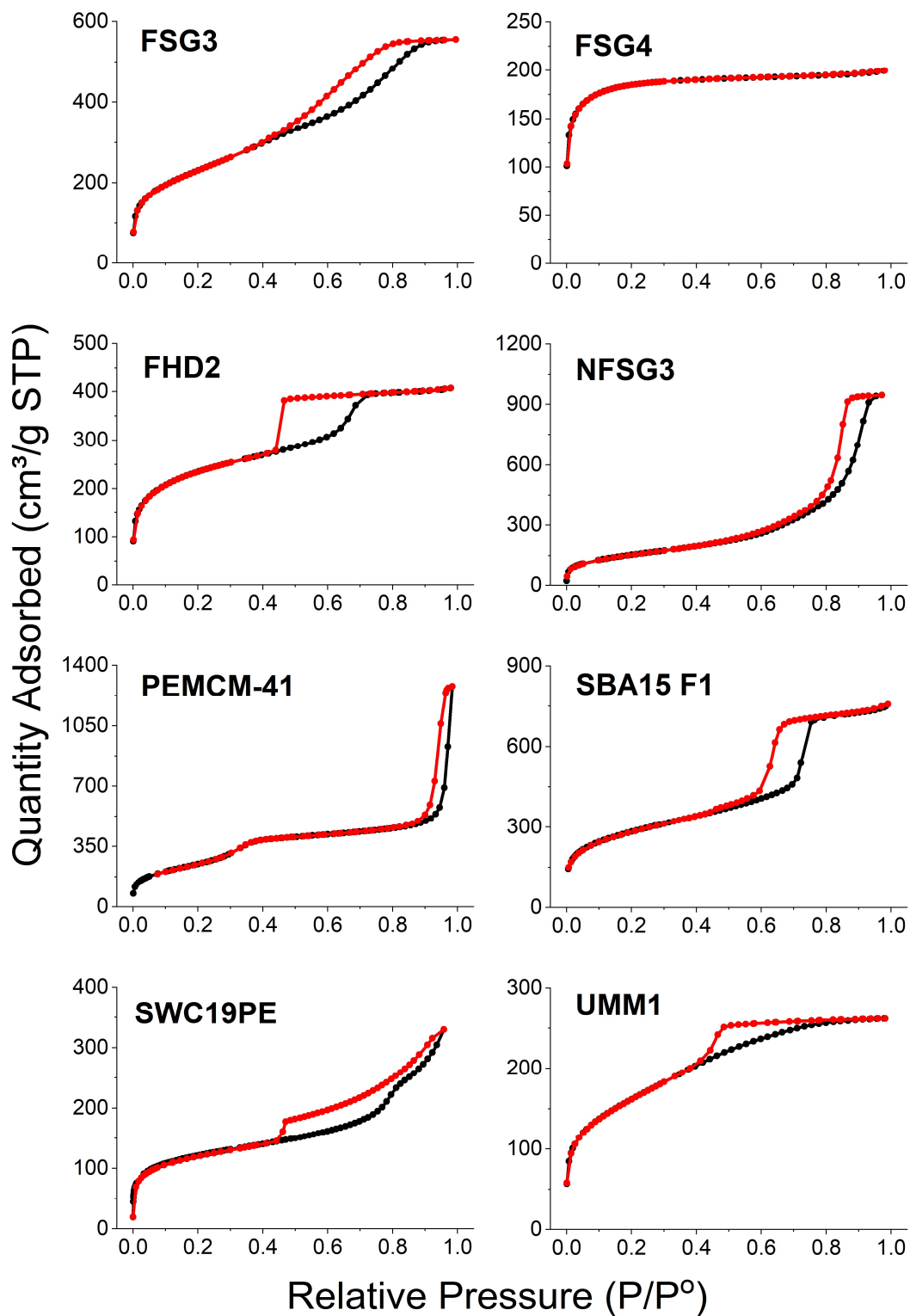
Figure 30. Example N$_2$ @77 K isotherms for a survey of different types of mesoporous silica illustrating the various types of porous structures achievable with these materials.

The application of these silicas for CO_2 capture does have a major drawback: nano-porous silicas do not capture CO_2 very well on their own. However, silicas can be used as a support for another adsorbent that does capture CO_2 well. Amines are one such adsorbent that can both interact with CO_2 and the silica surface.[122] One such amine is the polyethoxyamine, Jeffamine T-403. **Figure 31.**
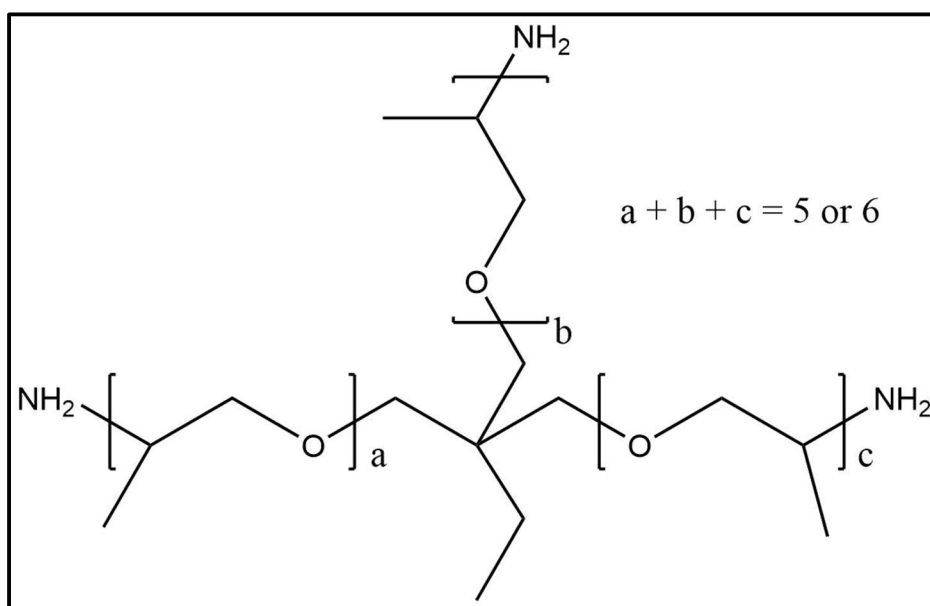
Figure 31. The polyethoxyamine Jeffamine T-403.

Together, we have produced and characterized many ordered porous silicas, however, implementation has not been straightforward. For example, increased surface area and pore volume on a silica does not necessarily lead to better CO_2 adsorption, despite having a higher theoretical active surface area. There are several issues that could be occurring that lead to poor results. One such issue could be cross interaction of several polyethoxyamine arms that naturally occurs when pore walls have a small enough diameter

to allow interaction between two or more adsorption sites. Another possibility could be that T-403 is effectively blocking the access to the internal porous structure. Both are possible and evidenced by reduced uptakes and slowed kinetics, but other possibilities still exist such as competitive interaction between proximal amines. Currently, research in our lab is occurring to address and overcome these issues. In any case another, cheaper alternative has been tested already and proven effective: fumed silica.

Fumed silica as a non-ordered porous silica produced by flame pyrolysis of a silicon containing precursor such as silicon tetrachloride or even sand. Being produced in this manner leads to these particles having a wide range of specific surface areas (SSAs) and particle sizes. Our lab has applied fumed silica with a typical particle size of 7 nm and a SSA of 334.4 m^2 g^{-1}. **Figure 32.** More importantly, this surface area is tied to large meso- and macropores and has proven to be effective at CO_2 adsorption at a 1:1 mass loading of Jeffamine T-403.[74, 75]
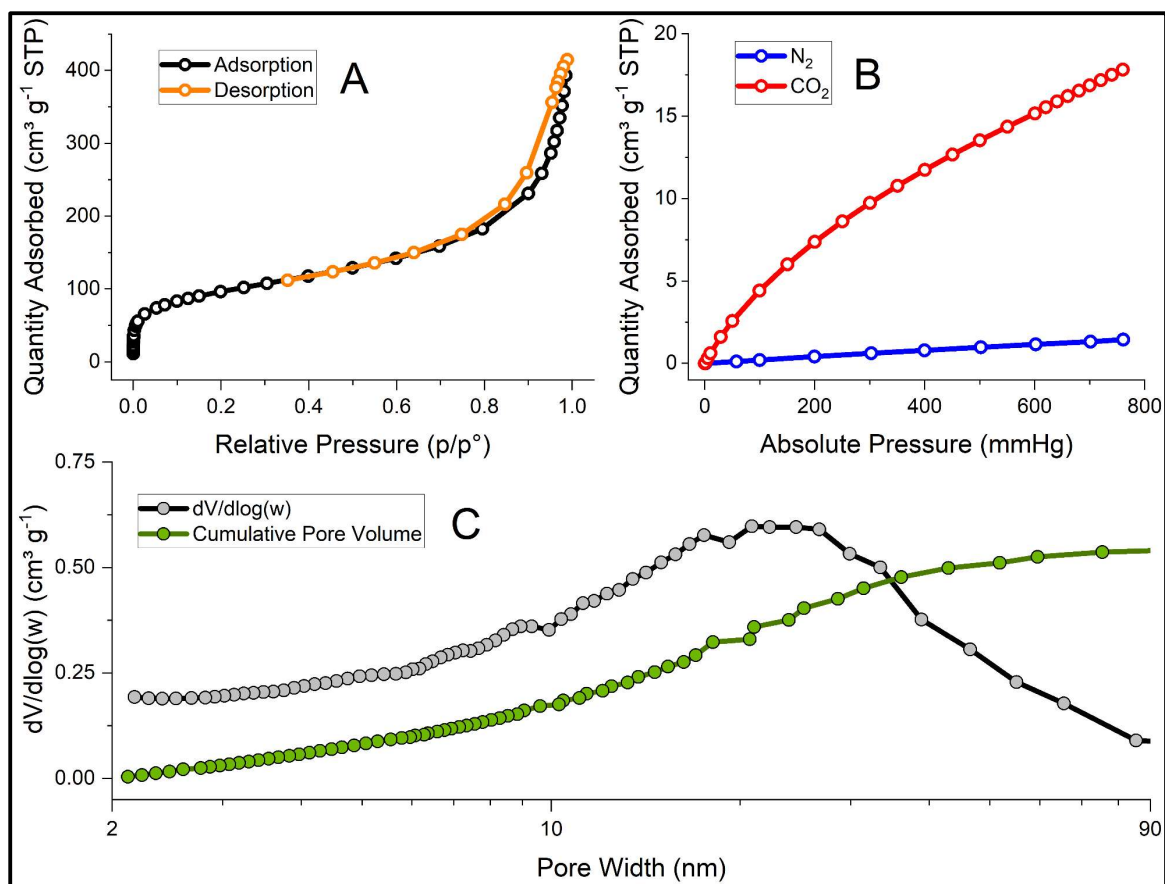
Figure 32. GAA data for 7 nm fumed silica including a 77 K N_2 isotherm (a), 0 °C N_2 and CO_2 isotherms (b) which demonstrate both the poor adsorption capabilities of silica surfaces on their own, and the 77 K N_2 pore size distribution (c) which highlights the wide disparity in pore sizes present in fumed silica.

4.2 Preparing amine loaded silica for CO_2 capture

As previously discussed, amines can interact with a silica surface.[74] If that silica surface has a large SSA, then more amines can interact with the surface. However, some issues have arisen when applying ultra-high nano-porous silicas, such as MCM-41 and SBA-15 type structures. Potential issues include amine-crosslinking, pore blocking by the organic components, competitive interaction between the adsorbent coating, or one of several other issues. Currently, work is being done to characterize and overcome these issues, however, for the purpose of the following work, fumed silica is substrate for the organic adsorbent Jeffamine T-403 to be applied upon.

A typical synthesis of the loaded silica material is very simple. Furthermore, as previously determined, a simple 1:1 mass ratio was previously determined to be best.[75] As an example synthesis: one gram of fumed silica can be dispersed in methanol with stirring, followed by one gram of Jeffamine being added dropwise with continued stirring. After, gentle heat of 70 °C is applied until the powder is dry.

A common question asked is why methanol? Is this the best solvent for dispersing the organic adsorbent across the silica surface? The quick answer for me is that those are the methods that I was given. Yet, there are some obvious benefits to using methanol, as it can be dried quickly and without the excessive heat that might damage the amine component to these adsorbents. Still, it seemed important to test the preparation porous silicas different solvents to assist in dispersion across silica surface.

Therefore, synthesis was attempted in a variety of common lab solvents, including water, ethanol, acetone, 2-propanol, chloroform, acetonitrile, and ethyl acetate. The synthesis followed the same procedure as the standard coating procedure in methanol. The results of this abbreviated study indicate that while some solvents are clearly worse than methanol, none are significantly better. In fact, the only solvent to outperform methanol was chloroform, which ended up adsorbing 1.33 mmol g^{-1} of CO_2 vs. the 1.31 mmol g^{-1} of CO_2 that methanol adsorbed.
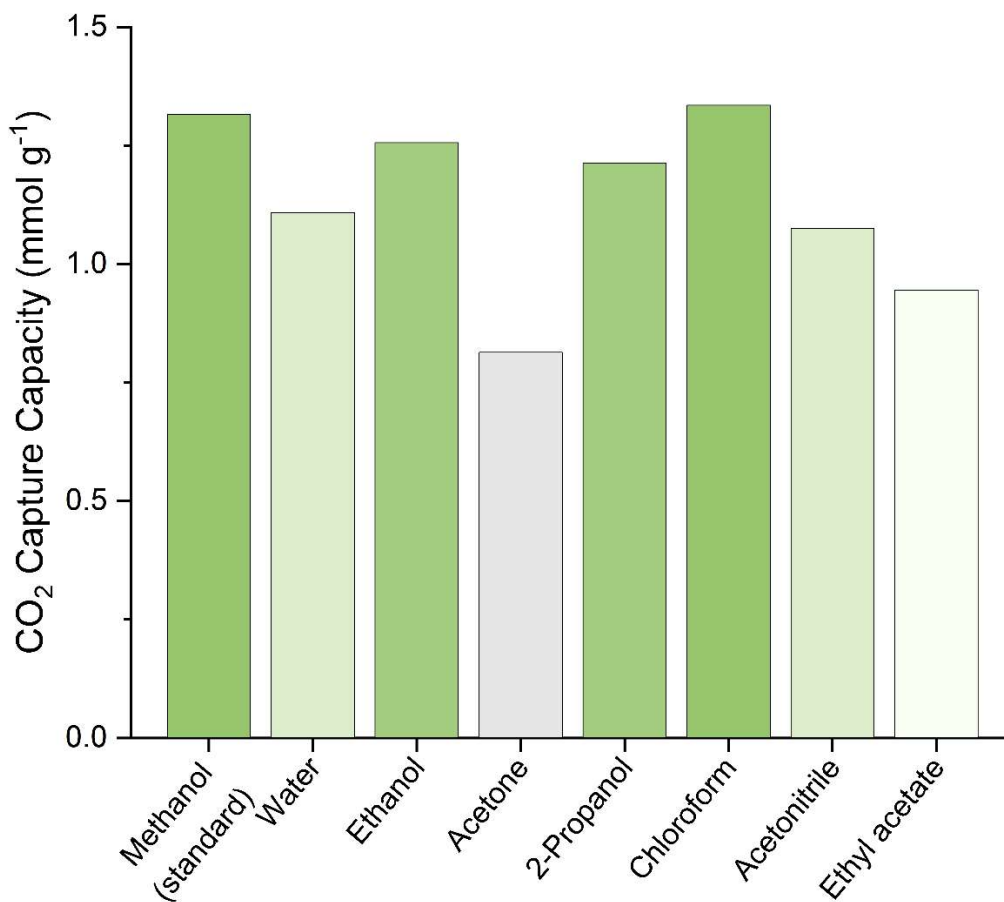
Figure 33. Survey study on the capture capacities of PEAS adsorbent, produced using various solvents.

The details of the CO_2 capture methodology is discussed in detail in the following section where a detailed discussion is required. It is also illustrated in **figure 35**.

Still, despite this minor increase in CO_2 capture capacity, the decision was made to keep using methanol, for consistency with previous studies and economic reasons, as methanol is less expensive than chloroform.[123] Therefore, in combination with previous studies relating to mass ratios, these PEAS are considered to be optimized for the adsorption of CO_2.

Moving forward, a more important issue is addressed; nano-scale size and electrostatic interactions can make the application of these particles difficult. These issues will be discussed, and a solution is suggested in the following section.

4.2.1 Materials and methods

Materials

All chemicals were used as purchased without further modification or purification. The polyethoxyamine, Jeffamine T-403, was obtained from Hunstman (Woodlands, TX). Fumed silica (7 nm powder size) and ethanol ($\geq$99.9) were purchased from Sigma-Aldrich (St. Louis, MO). Ethanol (200 proof) was purchased from DECON Laboratories (King of Prussia, PA).

Polyethoxyamine silica (PEAS) sorbents

The polyethoxyamine, Jeffamine T-403, was synthesized by a one-step combination of Jeffamine T-403 and fumed silica in a 1:1 mass ratio, combined in

methanol. A typical synthesis consists of one gram of fumed silica dispersed in methanol, followed by one gram of Jeffamine being added dropwise with stirring. After, gentle heat of 70 °C is applied until the powder is dry.

CO$_2$ capture/release experiment

Carbon capture experiments were performed in the TGA. This consists of four parts 1) initial outgassing at elevated temperature (90 °C) under inert gas (N$_2$), 2) equilibration at desired temperature (45 °C), 3) gas exchange to adsorbate (CO$_2$), and 4) gas exchange to N$_2$ for desorption step. For cycling trials, steps 3 and 4 are repeated for however many cycles are desired. See supplemental **figure S10** for further detail.

4.3 Enhancing the feasibility of nano-scale adsorbents for CO_2 capture in turbulent systems

Anthropogenic CO_2 is undoubtedly a considerable source of the greenhouse gas emissions which have resulted in increased global temperatures.[124] The largest source of these emissions come from industrial sources and power plants.[125] If international commitments (Paris agreement, Kyoto protocol, etc.) are to be kept, or as suggested by most experts exceeded, large point sources like these will need to be targeted for carbon capture and sequestration.

While technology is currently being developed to handle this predicament, such as absorption and membrane-based technologies, many consider adsorption to be the strongest candidate to solve this crisis.[126-129] This is because adsorbent-based systems can have many advantages over other technologies, including high-stability, low cost of implementation and regeneration, good selectivity, low or no vapor pressure, high specific uptake, and good kinetics. Research into nano-scale materials have fuelled much of the adsorbent-capture research.[130] However, some issues have been noted when it comes to implementing these nano-scale materials.

Incorporating adsorption technologies into flue systems can be challenging. Many adsorbents consist of fine powders that must be pelleted or otherwise contained prior to use in a turbulent environment. For example, the PEAS sorbent, a nanoparticle approximately 14 nm in diameter, is light enough such that electrostatic forces can cause the material to

be flung away, even in quiescent conditions. In order to apply such a sorbent in turbulent flue gas conditions for CO_2 capture, this issue must be addressed.

Pelleting through the use of binders has been considered for various adsorbents for CO_2 capture, with mixed results.[131-134] For example, work done by Rezaei *et al.* revealed that for several amine-modified silicas, increasing the pressure used in the pelleting process makes the adsorption kinetics worse, however as no impact on total capacity. This of course exacerbates one of the generic problems associated with pelleting, loss of material due to wear. Wilfong *et al.* recently demonstrated that several binders and binding methods do reduce total CO_2 capture capacity, as well as affect the mechanical strength of the pellet, and that additional additives such as fly ash may be required to mitigate some of the negative consequences of pelleting.[131]

Other immobilization means, such as monoliths and hollow fibres have also received much attention as alternatives to binding; however, each method has its own problems.[135-140] Pressure drop across the structure and pore blocking from impurities are possibly the two most important issues that monoliths face. Hollow fibres are quite promising however are comprised of a more complicated system that has not been fully evaluated in the presence of impurities and cannot be directly loaded with amine-based sorbents but must be loaded with a precursor and later modified. Additionally, research by Rezaei *et al.* and others have shown that the total capture capacity of several amine-modified silicas is significantly reduced when implemented in hollow fibres, compared to their powdered variation.[138] Therefore, alternative means of sorbent confinement remain an area of interest.

An alternative possibility for containing these sorbents is to trap it within a hydrogel. Bacterial cellulose (BC) is one such hydrogel, most often produced by the bacteria *Acetobacter xylinum,* and by mass consists of >99 % interstitial fluid and <1 % cellulose.[141, 142] Since this bloated matrix is mostly interstitial fluid, it is possible for very fine particles to penetrate into it by simply soaking the hydrogel in a solution or suspension. Drying then traps any dissolved or suspended compounds. The expansion of the cellulose matrix is non-elastic, so, once dried it will not expand back out.

In previous studies, we established that Jeffamine T-403, a polyethoxyamine, coated onto a silica surface was capable of CO_2 capture.[74, 75] A 1:1 mass ratio of Jeffamine T-403 and 14 nm fumed silica, both inexpensive precursors, produce a hybrid material (the PEAS sorbent) that has been reported to rapidly and reversibly capture up to 1.59 mmol CO_2 g^{-1} sorbent at 45 °C (approximating of flue gas conditions) with no additional heat necessary for desorption. Synthesizing the J-S hybrid is reported in the previous work but is simple and only requires a one-step combination of both components in methanol before stirring and drying. Complete CO_2 desorption can be achieved by applying vacuum or passing N_2 over the sample without the need for more energy-intensive desorption methods, such as heating aqueous solution, required for other sorbents.

4.3.1 Immobilization of PEAS sorbent in bacterial cellulose hydrogel

Immobilizing the PEAS sorbent in cellulose is a simple one-step process that involves incorporating and then drying the samples. In this process, bacterial cellulose initially contains ethanol as the interstitial fluid; a cut piece of BC was therefore added ethanol containing PEAS in a specific ratio (by mass) of BC to PEAS and agitated gently

for at least 1 hour. After the allotted time, the now-loaded BC was removed from the ethanol and dried in an oven at 90 °C.
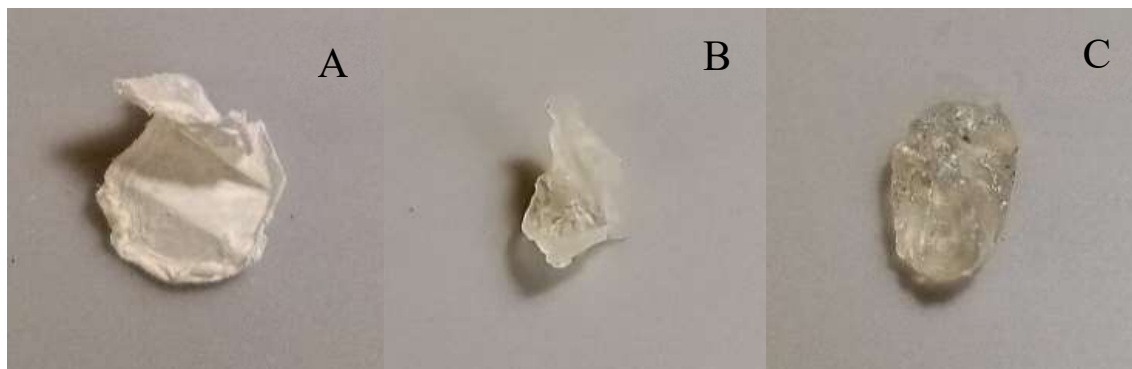
Figure 34. Dried bacterial cellulose hydrogels, loaded with PEAS in mass ratios of 2.0 % (A), 4.0 % (B), and 5.0 % (C), highlighting the textural differences between low mass ratios and high mass ratios.

Different mass loadings resulted in differently textured materials. **Figure 34.** Mass loadings of 3.0 % and below were able to be completely dried and resulted in a papery texture. At 4.0 % and above, samples always remained translucent, three-dimensional, and squishy. These 'bloated' samples appeared more bloated with increasing mass loadings. At 3.5 %, some mass loadings appear dry while others do not. In all samples, the PEAS can be contained within the hydrogel matrix with no noticeable loss of mass when handling, or even after aggravation of the sample.

4.3.2 CO$_2$ uptake and cycling studies for immobilized sorbent

Since PEAS captures CO$_2$ primarily through chemisorption, CO$_2$ capture capacities for the PEAS loaded cellulose were determined using thermogravimetric analysis (TGA, Q50 TA instruments) in an established four-step process.[74, 75, 143-145] **Figure 35.** After

loading a Pt pan with BC, an outgassing step was run at 90 °C under N_2 at 65 mL·min^{-1} until the mass levelled off to remove any pre-adsorbed CO_2, H_2O, or other substances. After, the temperature equilibrated at 45 °C. This is the initial mass used. Next, the gas switched to CO_2 at 65 mL·min^{-1} and the sample allowed to adsorb CO_2 until the mass levelled off over time, or if 500 minutes had passed without levelling off. Then, during regeneration, the gas was switched back to N_2 and the sorbent allowed to desorb completely. In cases where sorbent cycling was tested to study regeneration, the gas was immediately switched back to CO_2 following the degassing step, and the cycle was repeated over again.
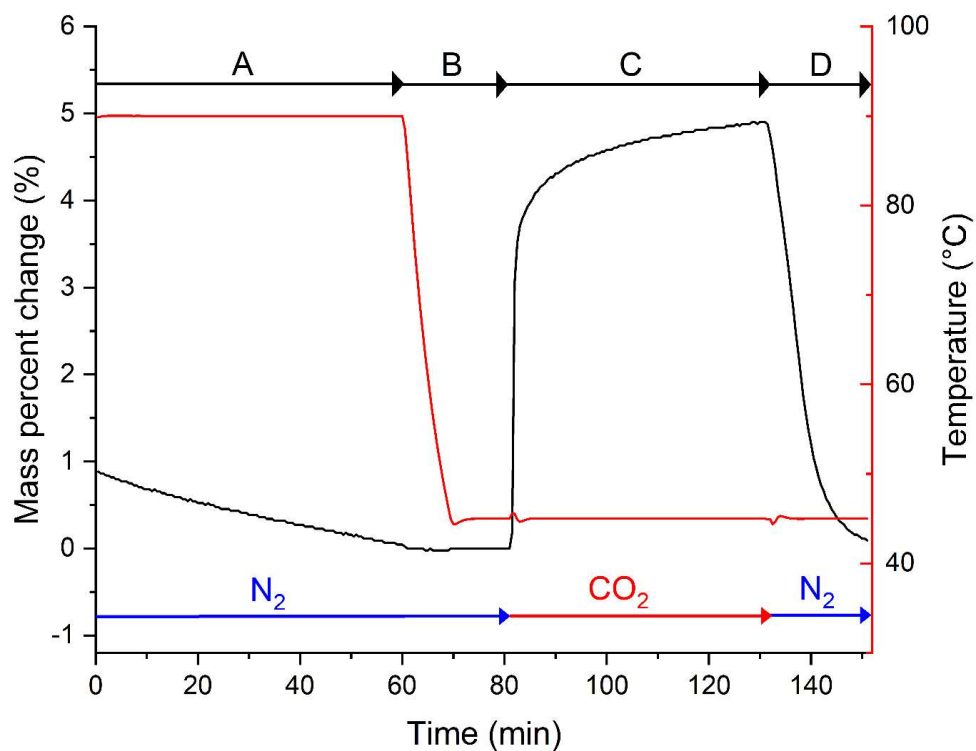
Figure 35. Typical TGA CO2 capture cycle. This consists of four parts initial outgassing at elevated temperature (90 °C) under inert gas (N_2) [A], equilibration at desired temperature (45 °C) [B], gas exchange to adsorbate (CO_2) [C], and gas exchange to N_2 for desorption step [D].

The CO_2 capture capacity for the J-S loaded BC increased with increasing PEAS mass loadings until 3.0 %, at which point the CO_2 uptake remained nearly constant. **Figure 2a.** Mass loadings 5.0 % and higher were attempted, however these resulted in materials that required excessively long capture times (greater than 500 min.) and did not improve upon the uptake values already seen by PEAS loaded BC in the 3.0 – 4.5 % range. This threshold has the same CO_2 uptake values as the PEAS alone. In fact, when normalized with the uptake values of the PEAS used, the filled hydrogels often slightly exceed the values of the PEAS. **Figure 2B.**
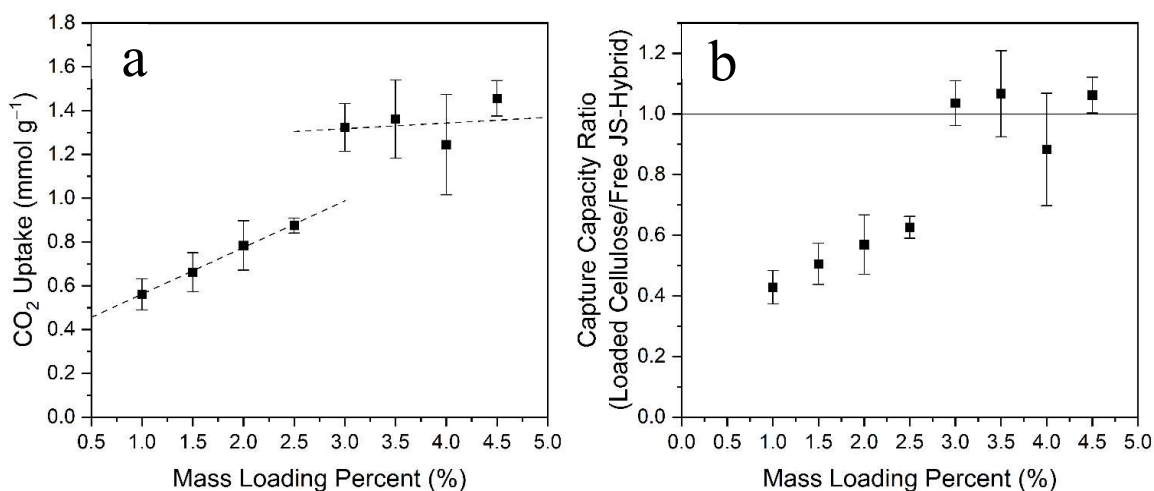
Figure 36. CO_2 capture capacities of the PEAS sorbent. Raw capacities (A) and capacities normalized by J-S hybrid as a free powder (B) demonstrate the ability of the hydrogel to be implemented without loss in specific capacity.

The kinetics of the adsorption process also appear to depend upon the PEAS mass loading. **Figure 37.** Since in all cases the initial uptake is linear, the initial slope values can be compared. Loadings below 2.5 % increase with increasing PEAS in the sample. Since, in this study, CO_2 capture occurred in an 100 % CO_2 atmosphere, it follows that the system behaves as a pseudo first-order system, thus increasing concentrations of PEAS should result in increasing rates. Data fitting suggests that indeed, for mass loadings of 2.5 % or

136

lower the pseudo first order equation provides a better fit. **Table 19.** Above 2.5 %, the
pseudo second order equation provides a better fit.
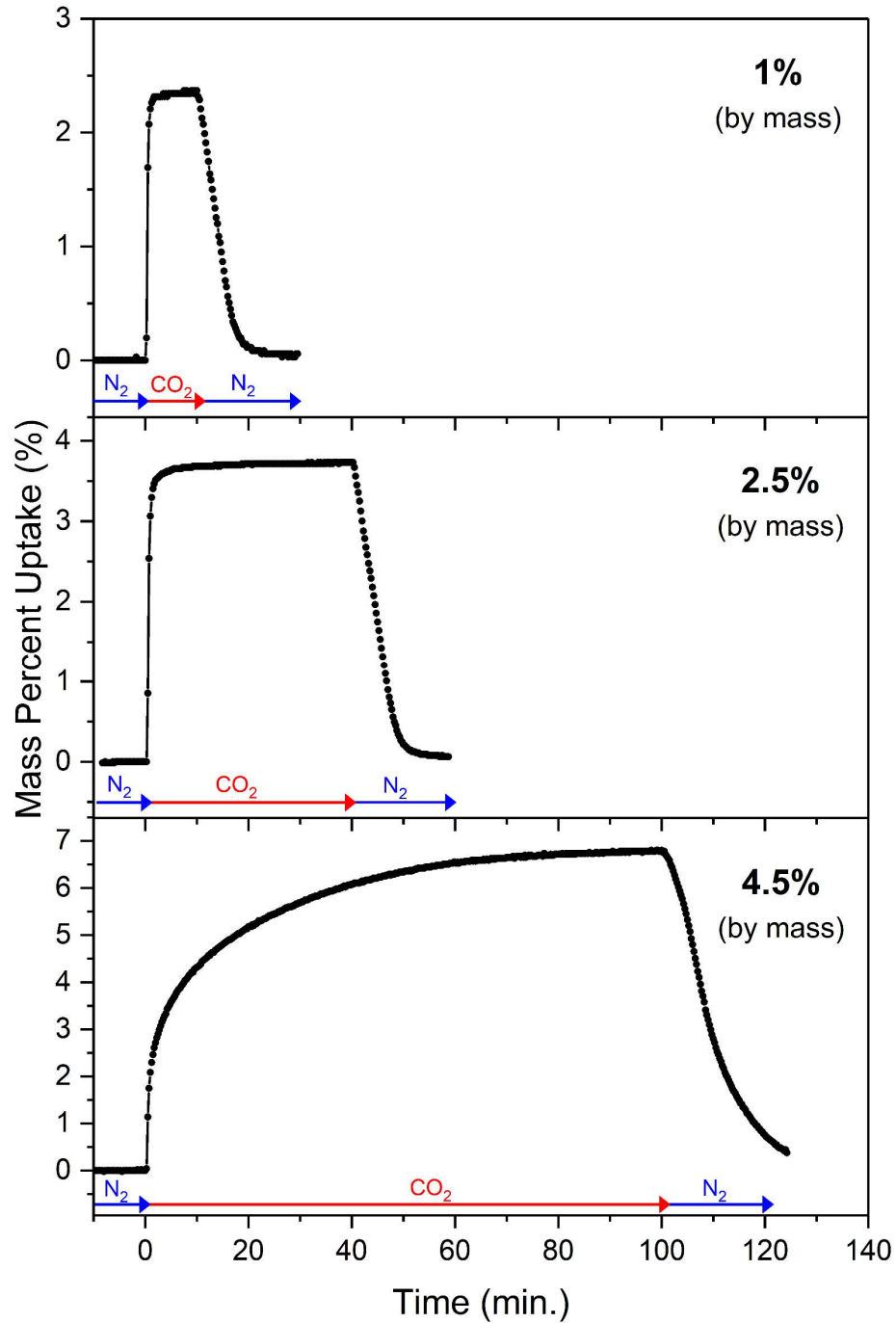
Figure 37. TGA CO_2 adsorption isotherms at 45 °C for several mass loadings of J-S hybrid into bacterial cellulose that show the effect of mass loading on the CO_2 uptake rate.

BC Mass loading	Pseudo first order			Pseudo second order		
	q_e	K	adj. R^2	q_e	K	adj. R^2
1.0%	2.793	1.610	**0.8967**	3.008	0.8320	0.8317
1.5%	2.863	1.644	**0.8940**	3.075	0.8433	0.8238
2.0%	3.549	2.321	**0.9871**	3.719	1.1980	0.9501
2.5%	4.021	1.512	**0.9496**	4.247	0.6081	0.8996
3.0%	4.665	0.8397	0.8359	4.862	0.2766	**0.9415**
3.5%	6.041	0.6063	0.8286	6.294	0.1545	**0.9382**
4.0%	6.257	0.08241	0.9028	7.012	0.01742	**0.9722**
4.5%	6.454	0.10026	0.8698	7.107	0.02239	**0.9636**

Table 19. Data fitting parameters for pseudo first and second order equations.

However, as mass loadings increase above 2.5 %, the sample no longer "dries out". In these samples, mass transport issues are believed to be the cause for increased adsorption time. In these samples CO_2 can no longer interact immediately with all the PEAS in the sample, rather CO_2 must first diffuse into the hydrogel and to the surface of a local PEAS. The optimal mass loading was determined to be 3.5 %. Despite having suboptimal kinetics, this mass loading was shown to have the best combination of speed and capacity. **Figure 38.A.**

The PEAS loaded BC was also shown to be highly regenerable. TGA cycling studies were performed by cycling between CO_2 and N_2 at 45 °C for 15 and 20 minutes, respectively, for five total cycles. **Figure S10.** The PEAS loaded BC was shown to capture identical amounts of CO_2 each cycle and desorb within 1 % of each other.
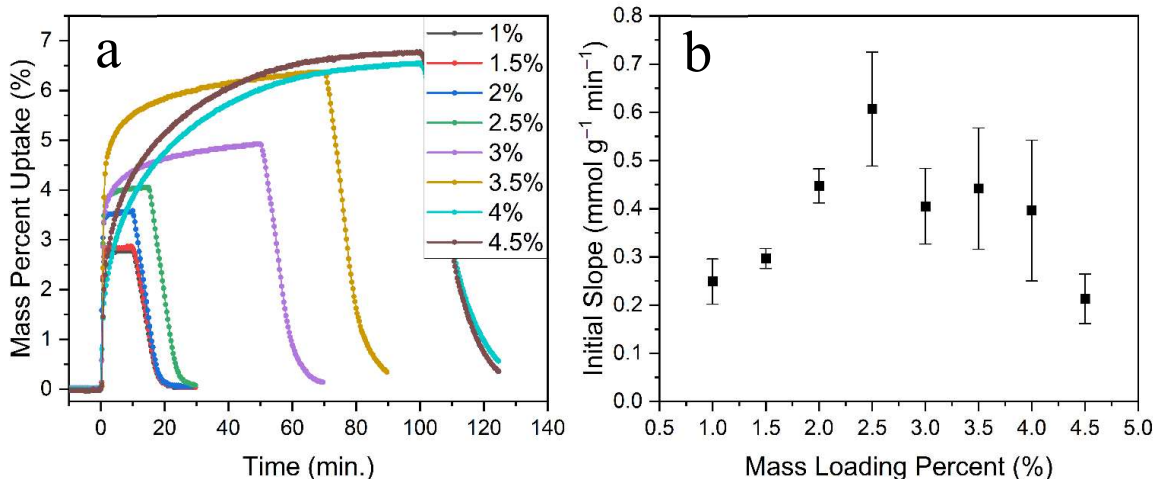
Figure 38. Example CO_2 adsorption/desorption curves (A) and initial slope values (B) for mass loadings of 1.0 – 4.5%, illustrating the effect of mass loading on both the kinetics and capacity of the PEAS sorbent loaded into a hydrogel.

Yet, while any single sample can be cycled with high reproducibility, replicate samples have considerable deviation in both their CO_2 uptakes and their initial slope values of all the mass loadings among replicate samples. In both instances, this deviation is larger among higher mass loadings.

Directly loading Jeffamine T-403, a liquid, into the hydrogel was also attempted. Neat T-403 and T-403 solutions were used in place of the PEAS suspension to load BC. Samples produced in both instances always resulted in a "bloated" hydrogel that was incapable of drying. These samples also contained very poor capacities (below 0.5 mmol g^{-1}) and extensive capture times (500+ minutes) without levelling off. This suggests that only solid adsorbents can be effectively loaded into bacterial cellulose hydrogels and maintain their functionality.

In this work we showed that bacterial cellulose hydrogels can be successfully used to immobilize solid nanoparticles for CO_2 adsorption without

compromising their effectiveness. Mass loadings of PEAS in ethanol at or above 3.0 % were shown to have the same specific CO_2 capture capacities as the PEAS alone. Loadings of 2.5 % were shown to have the best initial uptake times, however 3.5 % was suggested to be the best compromise between total capacity and rate based on the data. Future research will look at effective nanoparticle size range, other sorbents capable of being loaded, and other hydrogel systems to load into.

4.3.3 Materials and Methods

Materials

Ethanol (≥99.9%), sodium phosphate dibasic, and citric acid were purchased from Sigma-Aldrich (St. Louis, MO).

Gluconacetobacter xylinus (strain ATCC 700178) was obtained from ATCC (Manassas, VA). Yeast extract, peptone, and dextrose were purchased from Fisher Scientific (Waltham, MA). Mannitol was purchased from Calbiochem Merck (Billerica, MA).

Bacterial Cellulose

Bacterial cellulose (BC) was produced from cultures of Gluconacetobacter xylinus ATCC 700178, grown in a modified Hestrin-Schramm (H-S) medium following methods we reported previously.[32] The H-S medium consists of 2% w/v mannitol, 0.5% w/v yeast extract, 0.5% w/v peptone, 0.25% w/v sodium phosphate dibasic, and 0.15% w/v citric acid. The medium was adjusted to pH 6 by addition of 6.0 M HCl and then autoclaved at 125 °C, followed by the addition of 1% v/v ethanol using a sterile 0.2 μm syringe filter. Starter cultures were prepared by adding 5% v/v of a mother medium to fresh medium in 50 mL polypropylene tubes (Fisher Scientific). After 3 days of starter culture growth, 5% v/v of starter culture was added to 250 mL production cultures. Production cultures were allowed to grow for four days, the first pellicles were discarded, and then the second pellicles to develop were grown to the desired thicknesses, harvested with sterile forceps, and then washed in a 1% NaOH bath at 95 °C for 1 h. After the NaOH washing, pellicles

were transferred to a deionized water bath (~500 mL) where they were rinsed, with water changes every 2 h until a neutral pH was registered. Alcogels were prepared from the cleaned hydrogels by soaking them in a 200-proof ethanol bath (100 mL) which was refreshed after 2 h. The preparation of alcogels and storage in ethanol allowed for maintenance of the cellulose pellicles indefinitely until required.

PEAS@BC

PEAS were incorporated within bacterial cellulose by a one-step combination of freshly produced PEAS and bacterial cellulose (BC) in ethanol. Ethanol is chosen over methanol in this step because the bacterial cellulose is soaked in ethanol. A typical synthesis consists of combining a pre-weighed piece of the bacterial cellulose (approximately 0.3 x 0.5 x 0.8 cm^3; ~90 g) in 20 mL of ethanol, quickly to prevent the hydrogel from drying as much as possible. Gentle stirring is started. To this a predetermined amount of PEAS is added in accordance with the mass ratio desired and stirring is continued for 24 hours. After, a gentle heat of 75 °C is applied until the sample is dried.

CO_2 capture/release experiment

Carbon capture experiments were performed in the TGA. This consists of four parts 1) initial outgassing at elevated temperature (90 °C) under inert gas (N_2), 2) equilibration at desired temperature (45 °C), 3) gas exchange to adsorbate (CO_2), and 4) gas exchange

to N$_2$ for desorption step. For cycling trials, steps 3 and 4 are repeated for however many cycles are desired. See **Fig. S10** for further detail.

Modelling Equations

The pseudo-first order model (also known as the Lagergren model) suggests that the adsorption procedure is primarily influenced by the adsorbate concentration. Eq. 6.

Eq. 14 $\qquad \log(q_e - q_t) = \log q_e - \frac{K}{2.303} t \qquad$ *The pseudo-first order model*

Where q_e (mg · g^{-1}) represents the equilibrium capacity, q_t (mg · g^{-1}) represents the adsorbate uptake at time t (min), and K represents the first order adsorption rate (L · min^{-1}).

The pseudo-second order model can suggest that the rate of adsorption is proportional to the adsorbate concentration and the available sites on the adsorbent. Eq. 6.

Eq. 15 $\qquad \frac{t}{q_t} = \frac{1}{k_2 q_e^2} + \frac{t}{q_e} \qquad$ *The pseudo-second order model*

Where q_e (mg · g^{-1}) represents the equilibrium capacity, q_t (mg · g^{-1}) represents the

adsorbate uptake at time t (min), and k_2 represents the second order adsorption rate

constant.

5. Conclusions and Future Outlook

Above, the synthesis and characterization of several nanoporous materials have been described, as well as the application of these materials towards environmentally positive means. Largely, this work has involved porous carbon materials produced from the amino acid precursor L-histidine. This precursor, high in both nitrogen and oxygen led to a variety of amorphous carbon materials as different activating conditions, activating agents, and co-precursor compounds were implemented. The various resultant porous carbon materials, as well as some loaded and functionalized porous silicas were then successfully applied for CO_2 sequestration. Additionally, several of the porous carbon materials also found application in capturing both pharmaceutical and textile dye aqueous pollutants.

A constant thread throughout all the collected work here was adsorption, the separation of a particular analyte from a medium, such as water or air, by adhesion onto the surface of an introduced material. This generic definition can be subdivided into two categories: chemisorption, the adsorption of a compound due to some chemical interaction or reaction between analyte and active site on the material's surface, and physisorption, the adsorption of a compound without chemical influence. The presented body of work has displayed both classes of adsorption, at times either individually or simultaneously. In the porous carbon materials presented above, it was likely that both processes were observed, rather than exclusive chemisorption or physisorption occurring.

5.1 Adsorption of Aqueous Pollutants

When evaluating histidine derived porous carbons for their ability to uptake a variety of aqueous pollutants, these mechanisms were ultimately investigated. Thorough evaluation of a set of porous carbon's textural and chemical properties, coupled with isothermal and kinetic pollutant uptake studies, was used to better identify which properties were most beneficial. It became quickly apparent that no universality exists for optimizing these carbons. In some cases, textural properties seem more important, such as with the adsorption of methyl orange. At other times the chemical makeup of the carbon surface appears highly or even principally influential of the total adsorption capacity, such as with methyl green. The ultimate conclusion was that for any particular pollutant of interest, porous carbons should be individually tuned for maximizing the sorption ability, as the optimal process may tend towards a particular chemisorption process or physisorption process from adsorbate to adsorbate.

Additionally, this also suggests that the ability of porous carbons to contain such a diverse set of textural and chemical properties makes them very good candidates for continued research and use in this field. Thus, future studies could see an expansion of this work in several ways. To begin, the aqueous pollutants used here can hardly be considered as representative of the vast variety of unwanted compounds present in our oceans, waterways, lakes, etc. To this end, and expansion of the scope of this work should be considered to include representatives from any of the many classes of compounds poorly represented here, such as other cosmetic and pharmaceutical compounds like sulfa drugs or phthalates.

An alternative route of expansion would consider increasing the variety of porous carbons used. This is important to consider for two reasons. First, although a diverse set of properties was shown, many of these properties can be varied even more widely and other textural properties and surface chemistries entirely could be probed for their efficacy in pollutant separation. Even more, while this data serves as a good starting point, seven porous carbons alone do not provide enough data to conclusively dictate meaningful trends. Thus, a wider set of data would make for a better foundation for the possible conclusions above.

5.2 Adsorption of CO_2 with porous carbons

The capture of CO_2 was also pervasive throughout this body of work. In the case of histidine-derived porous carbons, many iterations were applied towards the creation of high-achieving materials. Initially, activation with simple and common activating agents was attempted. In this first pass, NaOH came out as the best activating agent, producing porous carbons with surface areas ranging from $500 - 1,200 \text{ m}^2 \text{ g}^{-1}$ and capable of capturing up to 3.38 mmol g^{-1} of CO_2. With this serving as a starting point, continued work would eventually demonstrate that histidine-derived porous carbons are capable of producing good materials for the capture of CO_2.

Other activating agents and co-pyrolysis mechanisms constituted much of the continued research. In a study that included a variety of activating agents (KOH, NaOH, H_3PO_4, Na_2CO_3, $NaHCO_3$, K_2HPO_4, and $ZnCl_2$), it was still found that NaOH was a leader in producing maximal surface area ($1,370 \text{ m}^2 \text{ g}^{-1}$), microporosity ($0.5022 \text{ cm}^3 \text{ g}^{-1}$), and total

CO_2 capacity (5.57 mmol g^{-1}). Still, other agents were also found to produce enhanced capacities, such as KOH (4.54 mmol g^{-1}) and even greener activating agents like Na_2CO_3 (4.86 mmol g^{-1}) and $NaHCO_3$ (4.23 mmol g^{-1}). It was also found that comparing across a set of carbons, the nitrogen content (particularly pyrrolic nitrogen) and the surface pH were the most influential in determining the overall capture capacity of CO_2.

The co-pyrolysis of histidine and choline hydroxide from their ionic liquid was also found to produce great CO_2 capture properties in the resultant porous carbon material. Here is the first time that NaOH activation was not the best, though this title went to the related KOH, while $ZnCl_2$ produced only modest CO_2 capacities. More interesting was varying the molar ratios of ChoOH and histidine, which had a strong apparent effect on the adsorption mechanism. While higher ratios of histidine resulted in a material capable of capturing over 8.30 mmol CO_2 g^{-1} at 0 °C, the capture process appears to be non-specific physisorption, unlikely to transfer well to real-world application. Alternatively, an even molar ratio of choline hydroxide and histidine resulted in a smaller capture capacity (5.57 mmol g^{-1}), but with a process that was appeared to be influenced by chemisorption, in conjunction with physisorption. Additional selectivity data also suggested that this carbon would transition better to real world mixed-gas application.

The future of this research has many potential directions. Thus far, some green activating agents have been applied, but the activating conditions were largely optimized for the combination of histidine and NaOH or KOH. Thus, optimizing the pyrolysis of histidine and Na_2CO_3 or $NaHCO_3$, which already show promise could result in very worthwhile materials. Additionally, continuing the search for other "green" activating agents that might produce even better results than we have seen here.

Although histidine has been the precursor of choice due to its initial success with common activating agents in early studies, several other amino acids also showed promise such as lysine. Though other research groups have continued some of this work, there is still much to explore in the realm of amino acid derived porous carbon materials.

Additionally, templating these materials with mesoporous silicas has also been considered and initial efforts have been attempted. Though hierarchical materials were produced, and a dramatically higher surface area was observed when compared to histidine pyrolyzed alone, the capture capacities of such materials has thus far been unimpressive. Still, many templates exist and upon activation, these already porous carbons could prove to be impressive materials.

5.3 Adsorption of CO_2 with coated porous silicas

Coated porous silicas were also applied for the application of CO_2 capture. In this work, hybrid materials were produced from nanoporous silica and an amine-containing organic molecule, namely the polyethoxyamine, Jeffamine T-403. These were initially produced based upon previous work in this research group. Capturing CO_2 through chemisorption, these sorbents prove capable of cycling CO_2 by gas exchange alone, suggesting that limited energy would be required for regeneration of the sorbent. A primary source of work here was towards the functionalization of these sorbents.

A big issue that I have addressed with these coated nanoparticles is that they are small and prone to static interactions. In a typical sample the static charge between your hand or the particles themselves would be enough to cause the sorbent to fly away, if a

gentle breeze had not already done so. Functionalization with bacterial cellulose hydrogel was found to be effective in immobilizing the sorbent, while maintaining its ability to capture CO_2 efficiently.

It was found that a mass loading ratio of 2.5 – 3.5% loaded silica in ethanol-bloated hydrogel proved to be optimal. Smaller percentages resulted in wasted specific capacity of the final sorbent. Higher mass loadings achieved a similar capacity as the loaded silica alone, but were kinetically poorer, likely due to a mass transport issue as the other hydrogels never fully dry out. Within the range of 2.5 – 3.5% the optimal capacity was reached without sacrificing the rapid kinetics found in the original loaded silica material.

From here, some future work has already been undertaken by several people, including myself. Initially, ordered mesoporous silicas have been produced and loading T-403 was attempted. Yet, little success has been found, with only diminished capacities being observed alongside highly elongated capture times. Others in our group have continued with various alternate amine-coatings and mesoporous silicas and have found some success. Still, many potential supports and adsorbent coatings are available and waiting to be tested. Additionally, this method of immobilization could be attempted and optimized for the successful sorbents, making their application more practical.

5.4 More Outlooks

Finally, the lessons learned here from these few materials could be applied towards many other materials and applications. The production of porous carbon materials from waste materials such as plastic has very promising potential for both application and waste

reduction. Indeed, there is still much to explore in these areas. For example, the carbonization and activation of plastics has seen some good progress, but still has very far to go before it is fully fleshed out. Many plastics have only a few publications dedicated to them so far. Those that do are often dedicated primarily to traditional activating agents and pyrolysis conditions. Emerging methods of activation such as microwave and hydrothermal processing offer new avenues of porous carbon production that have the potential to even be more environmentally sound. Likewise, alternative and greener activating agents (such as NaCl or Na_2CO_3) are constantly being considered and applied.

Additionally, the scope of application seen here has been quite limited, only considering the capture of pollutants. Yet, many applications are possible for these materials, such as energy or gas storage, desalination, medicine, or catalysis. Directly applying the already produced materials for these applications could be quite simple and lead to promising future work.

Supplemental Graphs, Tables, and Information
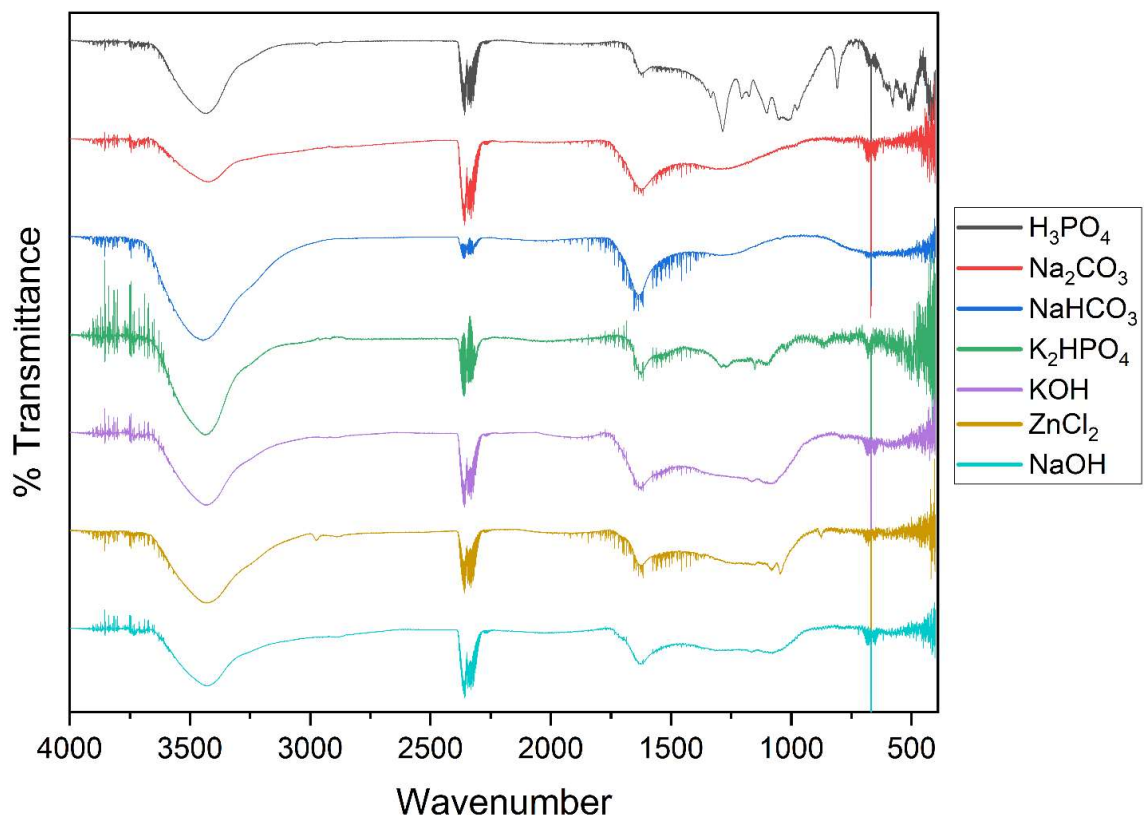
Fig. S1. IR spectra for seven histidine-derived activated porous carbons, exhibiting a number of common features among the various carbons produced here.
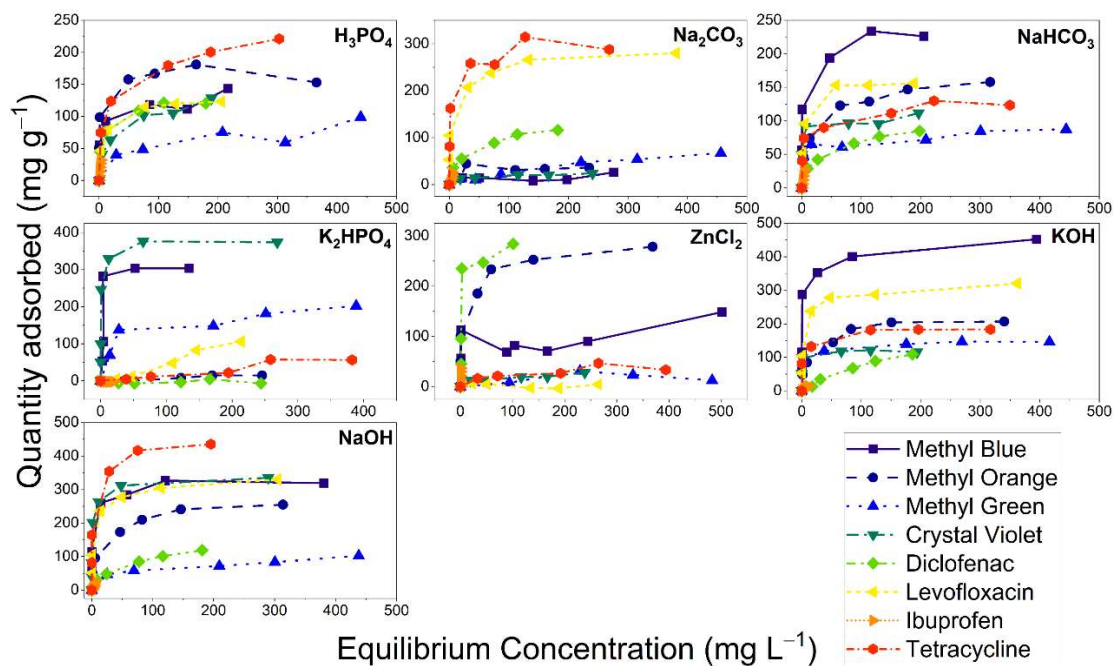
Figure S2. Equilibrium isotherms obtained in this study at 25 °C, sorted by adsorbent. Full isotherms were observed with a plateau for each adsorbate-adsorbent pair, except for isotherms of ibuprofen, which reached the solubility limit given the experimental parameters. To see these sorted by adsorbate, refer to **Figure 9.**
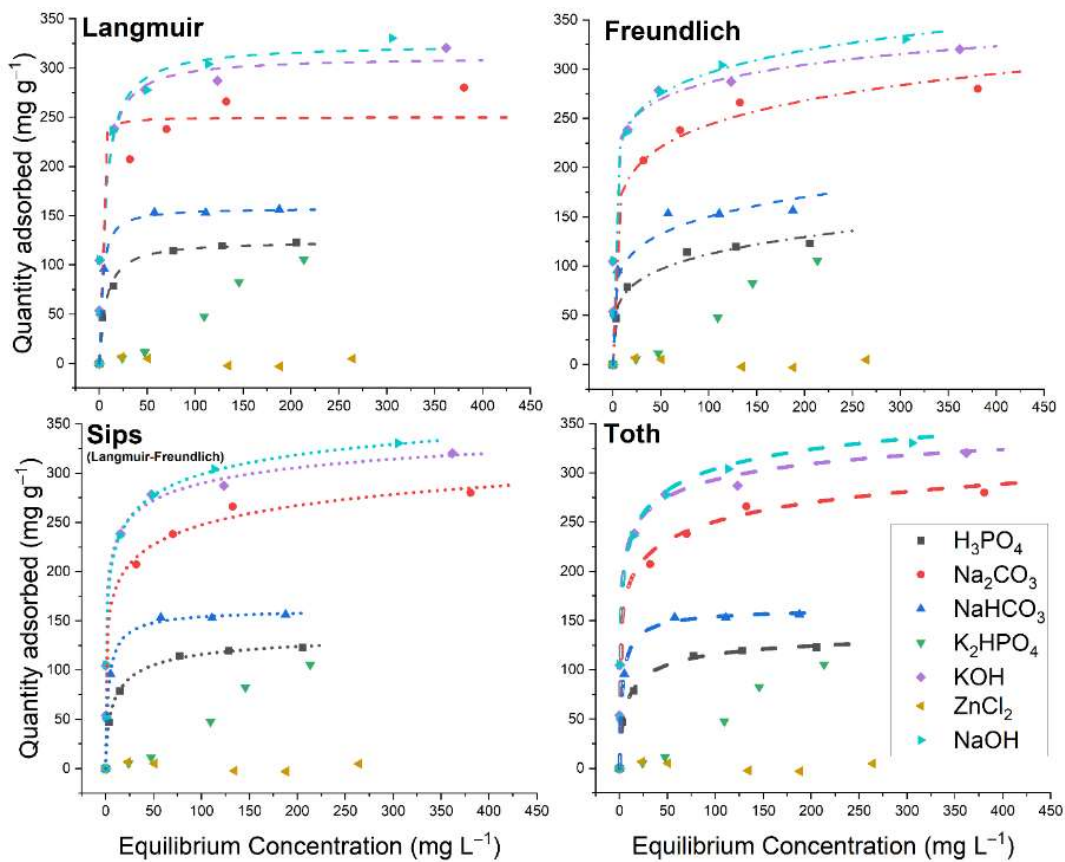
Figure S3. An example of the isotherm modelling used for further analysis of the adsorption process. (example: levofloxacin adsorption)

154

	Langmuir			Freundlich			Sips				Toth			
	$Q°$	b	R^2	K_F	n	R^2	K_{LF}	n_{LF}	a_{LF}	R^2	q_m	K	n	R^2
Methyl Blue														
KOH	404.77	3.121	0.654	264.30	10.800	0.969	478.09	0.1705	0.1417	0.980	5.195E+10	9.471	0.111	0.980
NaOH	298.98	6.151	0.948	156.60	7.228	0.904	350.82	0.4087	0.9859	0.975	8.869E+03	4.148	0.309	0.978
H₃PO₄	121.43	0.784	0.720	59.99	6.711	0.882	73.43	0.222	0.00201	0.826	3.754E+05	3.715	0.154	0.827
Na₂CO₃	-	-	-	-	-	-	-	-	-	-	-	-	-	-
NaHCO₃	178.72	5.245	0.953	109.24	9.693	0.733	738.99	0.861	5.161	0.937	2.540E+02	5.070	0.825	0.936
K₂HPO₄	316.97	0.388	0.280	162.81	7.228	0.159	3.07E-06	13.844	0.2643	0.978	-	-	-	-
ZnCl₂	-	-	-	-	-	-	-	-	-	-	-	-	-	-
Methyl Orange														
KOH	210.68	0.076	0.922	55.36	4.110	0.912	38.21	0.5854	0.03668	0.959	1.649E+02	0.666	0.410	0.954
NaOH	245.36	0.102	0.925	64.62	3.970	0.960	54.35	0.5031	0.2404	0.990	4.323E+02	0.996	0.308	0.988
H₃PO₄	163.72	1.829	0.820	93.08	8.820	0.834	224.19	0.443	1.6465	0.923	3.492E+03	4.382	0.335	0.916
Na₂CO₃	37.06	0.118	0.059	19.15	16.220	0.156	6.62E-09	7.599	0.0523	0.458	2.481E+07	5.19E-08	5.062	0.115
NaHCO₃	152.41	0.086	0.904	41.63	4.180	0.974	36.85	0.43775	0.0134	0.988	8.133E+02	1.310	0.236	0.987
K₂HPO₄	342.15	0.000	0.833	0.04	0.919	0.837	1.069	0.4583	8.92E-04	0.749	2.007E+02	3.46E-04	0.008	0.749
ZnCl₂	288.67	0.060	0.610	118.98	6.764	0.936	125.81	0.1594	1.10E-08	0.915	1.272E+10	4.986	0.089	0.905
Methyl Green														
KOH	140.13	0.860	0.757	87.07	11.128	0.985	101.4	0.114	2.12E-07	0.978	1.276E+06	5.770	0.168	0.961
NaOH	97.04	0.027	0.727	18.02	3.634	0.923	17.39	0.2817	5.30E-32	0.884	4.361E+06	1.808	0.078	0.867
H₃PO₄	91.33	0.019	0.549	12.83	3.177	0.670	14.172	0.297	4.76E-28	0.501	1.523E+06	1.509	0.075	0.494
Na₂CO₃	125.31	0.003	0.990	1.15	1.494	0.970	4.912	0.4148	1.13E-23	0.741	9.238E+02	3.07E-05	1.389	0.988
NaHCO₃	79.65	0.201	0.149	43.87	9.369	0.601	43.83	0.1071	2.04E-35	0.401	3.583E+07	5.053	0.117	0.319
K₂HPO₄	193.35	0.055	0.786	49.80	4.323	0.783	44.2	0.3769	3.71E-03	0.677	1.290E+02	0.606	0.400	0.683
ZnCl₂	-	-	-	-	-	-	-	-	-	-	-	-	-	-
Crystal Violet														
KOH	116.37	22.255	0.952	84.86	13.740	0.770	792.62	0.6366	19.45	0.992	6.999E+02	11.425	0.580	0.992
NaOH	310.78	1.476	0.826	178.61	8.020	0.886	367.85	0.4088	0.983	0.997	1.298E+04	4.144	0.290	0.996
H₃PO₄	127.49	0.062	0.909	25.80	3.300	0.977	24.68	0.3744	4.50E-04	0.968	2.892E+04	1.474	0.110	0.968
Na₂CO₃	24.11	0.049	0.780	6.11	4.080	0.903	6.08	0.2464	4.04E-31	0.854	3.200E+04	1.895	0.113	0.843
NaHCO₃	100.06	5.152	0.884	67.21	11.250	0.792	254.1	0.5811	4.625	0.867	4.704E+02	5.076	0.520	0.868
K₂HPO₄	364.51	2.959	0.872	267.19	14.550	0.852	738.54	0.4064	4.491	0.944	9.305E+03	5.824	0.360	0.941
ZnCl₂	28.19	0.026	0.656	3.73	2.830	0.842	3.431	0.3707	1.27E-24	0.760	7.092E+05	1.353	0.068	0.746

	Langmuir			Freundlich			Sips				Toth			
	$Q°$	b	R^2	K_F	n	R^2	K_{LF}	n_{LF}	a_{LF}	R^2	q_m	K	n	R^2
Diclofenac														
KOH	224.70	0.0052	0.991	2.86	1.421	0.977	10.34	0.4366	2.26E-22	0.753	855.13	1.24E-03	1.310	0.987
NaOH	141.09	0.0233	0.949	13.16	2.348	0.996	12.58	0.4535	3.93E-05	0.994	3.50E+09	1.1537	0.039	0.994
H₃PO₄	120.47	0.2360	0.940	45.43	5.013	0.951	45.87	0.5487	1.22E-01	0.988	188.53	1.1440	0.413	0.870
Na₂CO₃	126.61	0.0426	0.950	19.77	2.885	0.988	15.99	0.5036	4.11E-03	0.989	267.78	0.8217	0.217	0.988
NaHCO₃	93.58	0.0346	0.964	13.45	2.835	0.994	10.32	0.5181	3.88E-03	0.998	114.64	0.7036	0.239	0.997
K₂HPO₄	-	-	-	-	-	-	-	-	-	-	-	-	-	-
ZnCl₂	277.68	0.8554	0.737	150.02	7.136	0.484	139.43	2.7470	7.91E-01	0.899	2.59E+05	3.64E-04	7.638	0.899
Levofloxacin														
KOH	311.77	0.1990	0.848	191.71	11.458	0.939	268.97	0.2822	2.24E-01	0.898	6.79E+04	4.0880	0.218	0.900
NaOH	324.61	0.1722	0.889	180.26	9.277	0.983	219.24	0.3280	1.20E-01	1.000	1.32E+04	2.9630	0.245	1.000
H₃PO₄	124.82	0.1491	0.969	42.63	4.766	0.939	31.95	0.6555	1.04E-01	0.995	96.52	0.6110	0.541	0.994
Na₂CO₃	250.28	1.7615	0.809	128.13	7.176	0.970	169.03	0.2500	1.81E-02	0.980	2.85E+06	4.1400	0.143	0.978
NaHCO₃	158.21	0.3519	0.991	65.59	5.560	0.884	63.80	0.8323	3.25E-01	0.995	140.19	0.5859	0.776	0.994
K₂HPO₄	-	-	-	-	-	-	-	-	-	-	-	-	-	-
ZnCl₂	-	-	-	-	-	-	-	-	-	-	-	-	-	-
Ibuprofen														
KOH														
NaOH														
H₃PO₄														
Na₂CO₃														
NaHCO₃														
K₂HPO₄														
ZnCl₂														
Tetracycline														
KOH	188.81	0.1586	0.373	107.41	9.779	0.962	107.55	0.1022	2.97E-35	0.925	1.11E+10	7.9860	0.107	0.828
NaOH	451.80	0.1384	0.135	249.06	9.089	0.987	302.52	0.1358	6.34E-07	0.977	4.43E+08	7.5191	0.131	0.956
H₃PO₄	208.84	0.1057	0.866	60.64	4.391	0.997	61.53	0.2984	4.08E-04	0.999	1.10E+05	2.0620	0.134	0.999
Na₂CO₃	284.40	0.7457	0.805	162.00	2.312	0.816	247.38	0.4012	4.46E-01	0.800	3324.30	2.9250	0.324	0.799
NaHCO₃	102.14	0.8691	0.886	52.45	6.550	0.895	83.79	0.4988	4.85E-01	0.880	447.70	2.2640	0.392	0.891
K₂HPO₄	-	-	-	-	-	-	-	-	-	-	-	-	-	-
ZnCl₂	-	-	-	-	-	-	-	-	-	-	-	-	-	-

Table S1. Constants and correlations coefficients (R^2) for isotherm data fitting sorted by adsorbate.

		Langmuir			Freundlich			Sips				Toth			
		$Q°$	b	R^2	K_F	n	R^2	K_{LF}	n_{LF}	a_{LF}	R^2	q_m	K	n	R^2
KOH															
	Methyl Blue	404.77	3.121	0.654	264.30	10.800	0.969	478.09	0.1705	0.1417	0.980	5.195E+10	9.471	0.111	0.980
	Methyl Orange	210.68	0.076	0.922	55.36	4.110	0.912	38.21	0.5854	0.03668	0.959	1.649E+02	0.666	0.410	0.954
	Methyl Green	140.13	0.860	0.757	87.07	11.128	0.985	101.4	0.114	2.12E-07	0.978	1.276E+06	5.770	0.168	0.961
	Crystal Violet	116.37	22.255	0.952	84.86	13.740	0.770	792.62	0.6366	19.45	0.992	6.999E+02	11.425	0.580	0.992
	Diclofenac	224.70	0.0052	0.991	2.86	1.421	0.977	10.34	0.4366	2.26E-22	0.753	855.13	1.24E-03	1.310	0.987
	Levofloxacin	311.77	0.1990	0.848	191.71	11.458	0.939	268.97	0.2822	2.24E-01	0.898	6.79E+04	4.0880	0.218	0.900
	Ibuprofen														
	Tetracycline	188.81	0.1586	0.373	107.41	9.779	0.962	107.55	0.1022	2.97E-35	0.925	1.11E+10	7.9860	0.107	0.828
NaOH															
	Methyl Blue	298.98	6.151	0.948	156.60	7.228	0.904	350.82	0.4087	0.9859	0.975	8.869E+03	4.148	0.309	0.978
	Methyl Orange	245.36	0.102	0.925	64.62	3.970	0.960	54.35	0.5031	0.2404	0.990	4.323E+02	0.996	0.308	0.988
	Methyl Green	97.04	0.027	0.727	18.02	3.634	0.923	17.39	0.2817	5.30E-32	0.884	4.361E+06	1.808	0.078	0.867
	Crystal Violet	310.78	1.476	0.826	178.61	8.020	0.886	367.85	0.4088	0.983	0.997	1.298E+04	4.144	0.290	0.996
	Diclofenac	141.00	0.0233	0.949	13.16	2.348	0.996	12.58	0.4535	3.93E-05	0.994	3.50E+09	1.1537	0.039	0.994
	Levofloxacin	324.61	0.1722	0.889	180.26	9.277	0.983	219.24	0.3280	1.20E-01	1.000	1.32E+04	2.9630	0.245	1.000
	Ibuprofen														
	Tetracycline	451.80	0.1384	0.135	249.06	9.089	0.987	302.52	0.1358	6.34E-07	0.977	4.43E+08	7.5191	0.131	0.956
H₃PO₄															
	Methyl Blue	121.43	0.784	0.720	59.99	6.711	0.882	73.43	0.222	0.00201	0.826	3.754E+05	3.715	0.154	0.827
	Methyl Orange	163.72	1.829	0.820	93.08	8.820	0.834	224.19	0.443	1.6465	0.923	3.492E+03	4.382	0.335	0.916
	Methyl Green	91.33	0.019	0.549	12.83	3.177	0.670	14.172	0.297	4.76E-28	0.501	1.523E+06	1.509	0.075	0.494
	Crystal Violet	127.49	0.062	0.909	25.80	3.300	0.977	24.68	0.3744	4.50E-04	0.968	2.892E+04	1.474	0.110	0.968
	Diclofenac	120.47	0.2360	0.940	45.43	5.013	0.951	45.87	0.5487	1.22E-01	0.988	188.53	1.1440	0.413	0.870
	Levofloxacin	124.82	0.1491	0.969	42.63	4.766	0.939	31.95	0.6555	1.04E-01	0.995	96.52	0.6110	0.541	0.994
	Ibuprofen														
	Tetracycline	208.84	0.1057	0.866	60.64	4.391	0.997	61.53	0.2984	4.08E-04	0.999	1.10E+05	2.0620	0.134	0.999
Na₂CO₃															
	Methyl Blue	-	-	-	-	-	-	-	-	-	-	-	-	-	-
	Methyl Orange	37.06	0.118	0.059	19.15	16.220	0.156	6.62E-09	7.599	0.0523	0.458	2.481E+07	5.19E-08	5.062	0.115
	Methyl Green	125.31	0.003	0.990	1.15	1.494	0.970	4.912	0.4148	1.13E-23	0.741	9.238E+02	3.07E-04	1.389	0.988
	Crystal Violet	24.11	0.049	0.780	6.11	4.080	0.903	6.08	0.2464	4.04E-31	0.854	3.200E+04	1.895	0.113	0.843
	Diclofenac	126.61	0.0426	0.950	19.77	2.885	0.988	15.99	0.5036	4.11E-03	0.989	267.78	0.8217	0.217	0.988
	Levofloxacin	250.28	1.7615	0.809	128.13	7.176	0.970	169.03	0.2500	1.81E-02	0.980	2.85E+06	4.1400	0.143	0.978
	Ibuprofen														
	Tetracycline	284.40	0.7457	0.805	162.00	2.312	0.816	247.38	0.4012	4.46E-01	0.800	3324.30	2.9250	0.324	0.799

		Langmuir			Freundlich			Sips				Toth			
		$Q°$	b	R^2	K_F	n	R^2	K_{LF}	n_{LF}	a_{LF}	R^2	q_m	K	n	R^2
NaHCO₃															
	Methyl Blue	178.72	5.245	0.953	109.24	9.693	0.733	738.99	0.861	5.161	0.937	2.540E+02	5.070	0.825	0.936
	Methyl Orange	152.41	0.086	0.904	41.63	4.180	0.974	36.85	0.43775	0.0134	0.988	8.133E+02	1.310	0.236	0.987
	Methyl Green	79.65	0.201	0.149	43.87	9.369	0.601	43.83	0.1071	2.04E-35	0.401	3.583E+07	5.053	0.117	0.319
	Crystal Violet	100.06	5.152	0.884	67.21	11.250	0.792	254.1	0.5811	4.625	0.867	4.704E+02	5.076	0.520	0.868
	Diclofenac	93.58	0.0346	0.964	13.45	2.835	0.994	10.32	0.5181	3.88E-03	0.998	114.64	0.7036	0.239	0.997
	Levofloxacin	158.21	0.3519	0.991	65.59	5.560	0.884	63.80	0.8323	3.25E-01	0.995	140.19	0.5859	0.776	0.994
	Ibuprofen														
	Tetracycline	102.14	0.8691	0.886	52.45	6.550	0.895	83.79	0.4988	4.85E-01	0.880	447.70	2.2640	0.392	0.891
K₂HPO₄															
	Methyl Blue	316.97	0.388	0.280	162.81	7.228	0.159	3.07E-06	13.844	0.2643	0.978	-	-	-	-
	Methyl Orange	342.15	0.000	0.833	0.04	0.919	0.837	1.069	0.4583	8.92E-21	0.287	2.007E+02	3.46E-04	0.008	0.749
	Methyl Green	193.35	0.055	0.786	49.80	4.323	0.783	44.2	0.3769	3.71E-06	0.677	1.290E+02	0.606	0.400	0.683
	Crystal Violet	364.51	2.959	0.872	267.19	14.550	0.852	738.54	0.4064	4.491	0.944	9.305E+03	5.824	0.360	0.941
	Diclofenac	-	-	-	-	-	-	-	-	-	-	-	-	-	-
	Levofloxacin	-	-	-	-	-	-	-	-	-	-	-	-	-	-
	Ibuprofen														
	Tetracycline	-	-	-	-	-	-	-	-	-	-	-	-	-	-
ZnCl₂															
	Methyl Blue	-	-	-	-	-	-	-	-	-	-	-	-	-	-
	Methyl Orange	288.67	0.060	0.610	118.98	6.764	0.936	125.81	0.1594	1.10E-08	0.915	1.272E+10	4.986	0.089	0.905
	Methyl Green	-	-	-	-	-	-	-	-	-	-	-	-	-	-
	Crystal Violet	28.19	0.026	0.656	3.73	2.830	0.842	3.431	0.3707	1.27E-24	0.760	7.092E+05	1.353	0.068	0.746
	Diclofenac	277.68	0.8554	0.737	150.02	7.136	0.484	139.43	2.7470	7.91E-01	0.899	2.59E+05	3.64E-04	7.638	0.899
	Levofloxacin	-	-	-	-	-	-	-	-	-	-	-	-	-	-
	Ibuprofen														
	Tetracycline	-	-	-	-	-	-	-	-	-	-	-	-	-	-

Table S2. Constants and correlation coefficients (R^2) for isotherm data fitting sorted by activating agent.
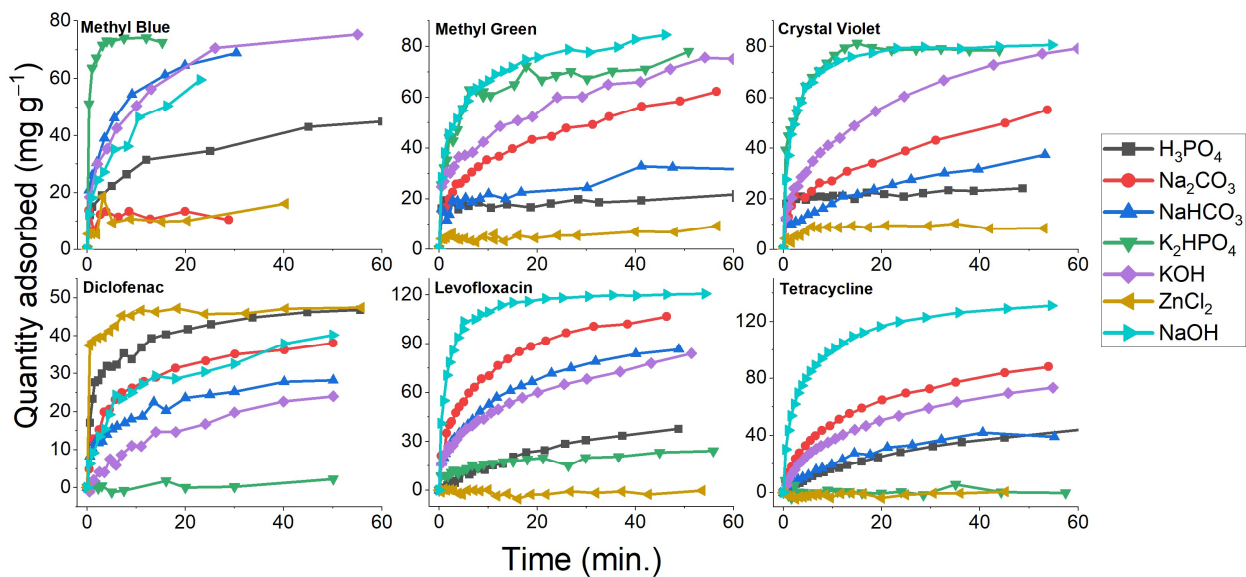
Figure S4. 25 °C isotherms for the adsorption of several aqueous pollutants on histidine-derived activated carbons, collected for the analysis of the uptake kinetics.

	Pseudo First Order			Pseudo Second Order			Elovich			Intraparticle diffusion*		
	q_e	K	R^2	q_e	k_2	R^2	β_e	α	R^2	k_{id}	C	R^2
Methyl Blue												
KOH	70.14	0.1659	0.837	78.70	2.91E-03	0.917	0.0768	73.17	0.956	8.681	19.359	0.904
NaOH	53.54	0.2123	0.820	63.17	4.11E-03	0.882	0.0981	74.08	0.892	10.864	7.894	0.985
H_3PO_4	39.94	0.1765	0.742	43.74	6.08E-03	0.854	0.1433	51.81	0.953	4.622	11.583	0.965
Na_2CO_3	-	-	-	-	-	-	-	-	-	-	-	-
$NaHCO_3$	62.44	0.3293	0.814	69.67	6.65E-03	0.904	0.0861	127.58	0.961	10.249	18.269	0.951
K_2HPO_4	71.59	0.3510	0.819	74.75	8.41E-02	0.978	0.1971	3.84E+04	0.797	5.123	58.086	0.505
$ZnCl_2$	-	-	-	-	-	-	-	-	-	-	-	-
Methyl Orange												
KOH												
NaOH												
H_3PO_4												
Na_2CO_3												
$NaHCO_3$												
K_2HPO_4												
$ZnCl_2$												
Methyl Green												
KOH	68.33	0.1510	0.675	75.76	2.87E-03	0.815	0.0835	77.23	0.931	6.871	22.020	0.982
NaOH	74.21	0.3782	0.770	81.39	7.14E-03	0.929	0.0800	244.85	0.993	8.044	36.589	0.875
H_3PO_4	-	-	-	-	-	-	-	-	-	-	-	-
Na_2CO_3	52.04	0.1438	0.829	60.25	2.96E-03	0.912	0.0928	35.46	0.952	7.030	11.117	0.990
$NaHCO_3$	250.33	0.4396	0.295	27.96	2.10E-02	0.541	0.2480	106.13	0.787	2.698	12.179	0.884
K_2HPO_4	67.48	0.4415	0.854	73.43	9.02E-03	0.940	0.0915	265.75	0.932	6.817	34.647	0.768
$ZnCl_2$	-	-	-	-	-	-	-	-	-	-	-	-
Crystal Violet												
KOH	74.24	0.0965	0.924	86.40	1.34E-03	0.964	0.0662	34.09	0.964	9.344	9.789	0.967
NaOH	76.16	0.5200	0.954	82.33	9.64E-03	0.995	0.0869	448.45	0.962	8.428	35.264	0.652
H_3PO_4	21.46	2.8450	0.932	22.01	2.86E-01	0.957	0.9142	3.32E+07	0.979	1.610	14.874	0.361
Na_2CO_3	46.46	0.1142	0.814	53.02	2.90E-03	0.884	0.1094	30.07	0.930	6.664	6.392	0.974
$NaHCO_3$	31.82	0.0971	0.807	37.79	3.10E-03	0.856	0.1690	20.21	0.865	4.559	4.007	0.965
K_2HPO_4	76.13	0.6205	0.891	81.36	1.28E-02	0.960	0.0967	965.21	0.958	8.654	37.609	0.636
$ZnCl_2$	9.17	0.3615	0.883	9.93	5.61E-02	0.868	0.6844	32.18	0.811	1.041	3.780	0.548

	Pseudo First Order			Pseudo Second Order			Elovich			Intraparticle diffusion*		
	q_e	K	R^2	q_e	k_2	R^2	β_e	α	R^2	k_{id}	C	R^2
Diclofenac												
KOH	24.80	0.0562	0.981	34.15	1.35E-03	0.984	0.1756	4.905	0.938	3.956	-2.312	0.977
NaOH	34.17	0.1705	0.933	40.09	4.98E-03	0.969	0.1334	23.42	0.975	4.971	7.395	0.910
H_3PO_4	39.62	0.6014	0.836	43.67	1.86E-01	0.940	0.1603	229.19	0.990	3.914	22.185	0.876
Na_2CO_3	33.98	0.2051	0.946	38.77	6.85E-03	0.985	0.1418	31.81	0.997	4.630	9.628	0.883
$NaHCO_3$	24.27	0.2147	0.838	27.50	1.05E-02	0.920	0.2086	27.96	0.970	3.277	7.474	0.961
K_2HPO_4	-	-	-	-	-	-	-	-	-	-	-	-
$ZnCl_2$	44.49	2.7500	0.936	45.98	1.12E-01	0.971	0.3982	1.16E+07	0.988	1.488	38.718	0.680
Levofloxacin												
KOH	71.56	0.1247	0.851	83.88	1.81E-03	0.920	0.0674	43.59	0.942	10.259	12.373	0.992
NaOH	114.77	0.5607	0.916	122.92	7.30E-03	0.991	0.0618	9.89E+02	0.913	9.356	68.221	0.667
H_3PO_4	42.83	0.0420	0.990	63.48	4.79E-04	0.991	0.1185	6.894	0.878	6.360	-5.179	0.988
Na_2CO_3	95.77	0.1712	0.914	111.99	1.85E-03	0.967	0.0484	71.32	0.974	14.626	19.880	0.946
$NaHCO_3$	78.09	0.1294	0.915	93.21	1.59E-03	0.958	0.0591	44.02	0.954	11.994	11.258	0.978
K_2HPO_4	19.36	0.2409	0.632	21.70	1.56E-02	0.760	0.2915	35.88	0.860	2.319	7.386	0.889
$ZnCl_2$	-	-	-	-	-	-	-	-	-	-	-	-
Ibuprofen												
KOH												
NaOH												
H_3PO_4												
Na_2CO_3												
$NaHCO_3$												
K_2HPO_4												
$ZnCl_2$												
Tetracycline												
KOH	67.93	0.0814	0.968	85.54	9.42E-04	0.989	0.0626	19.65	0.971	10.437	1.757	0.982
NaOH	117.85	0.2673	0.896	132.35	2.77E-03	0.978	0.0436	166.51	0.993	14.296	45.168	0.857
H_3PO_4	47.73	0.0398	0.992	66.45	4.82E-04	0.996	0.1083	7.976	0.899	6.451	-4.315	0.997
Na_2CO_3	80.26	0.0986	0.962	98.35	1.06E-03	0.987	0.0566	32.80	0.959	12.144	6.328	0.974
$NaHCO_3$	41.72	0.0671	0.989	55.33	1.07E-03	0.987	0.1037	10.01	0.937	6.761	-2.609	0.954
K_2HPO_4	-	-	-	-	-	-	-	-	-	-	-	-
$ZnCl_2$	-	-	-	-	-	-	-	-	-	-	-	-

Table S3. Constants and correlations for kinetic data fitting sorted by adsorbate. *This is the data for the IPD when fit across the entire dataset, rather than in a piecewise manner.

	Pseudo First Order			Pseudo Second Order			Elovich			Intraparticle diffusion*		
	q_e	K	R^2	q_e	k_2	R^2	β_e	α	R^2	k_{id}	C	R^2
KOH												
Methyl Blue	70.14	0.1659	0.837	78.70	2.91E-03	0.917	0.0768	73.17	0.956	8.681	19.359	0.904
Methyl Orange												
Methyl Green	68.33	0.1510	0.675	75.76	2.87E-03	0.815	0.0835	77.23	0.931	6.871	22.020	0.982
Crystal Violet	74.24	0.0965	0.924	86.40	1.34E-03	0.964	0.0662	34.09	0.964	9.344	9.789	0.967
Diclofenac	24.80	0.0562	0.981	34.15	1.35E-03	0.984	0.1756	4.905	0.938	3.956	-2.312	0.977
Levofloxacin	71.56	0.1247	0.851	83.88	1.81E-03	0.920	0.0674	43.59	0.942	10.259	12.373	0.992
Ibuprofen												
Tetracycline	67.93	0.0814	0.968	85.54	9.42E-04	0.989	0.0626	19.65	0.971	10.437	1.757	0.982
NaOH												
Methyl Blue	53.54	0.2123	0.820	63.17	4.11E-03	0.882	0.0981	74.08	0.892	10.864	7.894	0.985
Methyl Orange												
Methyl Green	74.21	0.3782	0.770	81.39	7.14E-03	0.929	0.0800	244.85	0.993	8.044	36.589	0.875
Crystal Violet	76.16	0.5200	0.954	82.33	9.64E-03	0.995	0.0869	448.45	0.962	8.428	35.264	0.652
Diclofenac	34.17	0.1705	0.933	40.09	4.98E-03	0.969	0.1334	23.42	0.975	4.971	7.395	0.910
Levofloxacin	114.77	0.5607	0.916	122.92	7.30E-03	0.991	0.0618	9.89E+02	0.913	9.356	68.221	0.667
Ibuprofen												
Tetracycline	117.85	0.2673	0.896	132.35	2.77E-03	0.978	0.0436	166.51	0.993	14.296	45.168	0.857
H₃PO₄												
Methyl Blue	39.94	0.1765	0.742	43.74	6.08E-03	0.854	0.1433	51.81	0.953	4.622	11.583	0.965
Methyl Orange												
Methyl Green	-	-	-	-	-	-	-	-	-	-	-	-
Crystal Violet	21.46	2.8450	0.932	22.01	2.86E-01	0.957	0.9142	3.32E+07	0.979	1.610	14.874	0.361
Diclofenac	39.62	0.6014	0.836	43.67	1.86E-01	0.940	0.1603	229.19	0.990	3.914	22.185	0.876
Levofloxacin	42.83	0.0420	0.990	63.48	4.79E-04	0.991	0.1185	6.894	0.878	6.360	-5.179	0.988
Ibuprofen												
Tetracycline	47.73	0.0398	0.992	66.45	4.82E-04	0.996	0.1083	7.976	0.899	6.451	-4.315	0.997
Na₂CO₃												
Methyl Blue	-	-	-	-	-	-	-	-	-	-	-	-
Methyl Orange												
Methyl Green	52.04	0.1438	0.829	60.25	2.96E-03	0.912	0.0928	35.46	0.952	7.030	11.117	0.990
Crystal Violet	46.46	0.1142	0.814	53.02	2.90E-03	0.884	0.1094	30.07	0.930	6.664	6.392	0.974
Diclofenac	33.98	0.2051	0.946	38.77	6.85E-03	0.985	0.1418	31.81	0.997	4.630	9.628	0.883
Levofloxacin	95.77	0.1712	0.914	111.99	1.85E-03	0.967	0.0484	71.32	0.974	14.626	19.880	0.946
Ibuprofen												
Tetracycline	80.26	0.0986	0.962	98.35	1.06E-03	0.987	0.0566	32.80	0.959	12.144	6.328	0.974

	Pseudo First Order			Pseudo Second Order			Elovich			Intraparticle diffusion*		
	q_e	K	R^2	q_e	k_2	R^2	β_e	α	R^2	k_{id}	C	R^2
NaHCO₃												
Methyl Blue	62.44	0.3293	0.814	69.67	6.65E-03	0.904	0.0861	127.58	0.961	10.249	18.269	0.951
Methyl Orange												
Methyl Green	250.33	0.4396	0.295	27.96	2.10E-02	0.541	0.2480	106.13	0.787	2.698	12.179	0.884
Crystal Violet	31.82	0.0971	0.807	37.79	3.10E-03	0.856	0.1690	20.21	0.865	4.559	4.007	0.965
Diclofenac	24.27	0.2147	0.838	27.50	1.05E-02	0.920	0.2086	27.96	0.970	3.277	7.474	0.961
Levofloxacin	78.09	0.1294	0.915	93.21	1.59E-03	0.958	0.0591	44.02	0.954	11.994	11.258	0.978
Ibuprofen												
Tetracycline	41.72	0.0671	0.989	55.33	1.07E-03	0.987	0.1037	10.01	0.937	6.761	-2.609	0.954
K₂HPO₄												
Methyl Blue	71.59	0.3510	0.819	74.75	8.41E-02	0.978	0.1971	3.84E+04	0.797	5.123	58.086	0.505
Methyl Orange												
Methyl Green	67.48	0.4415	0.854	73.43	9.02E-03	0.940	0.0915	265.75	0.932	6.817	34.647	0.768
Crystal Violet	76.13	0.6205	0.891	81.36	1.28E-02	0.960	0.0967	965.21	0.958	8.654	37.609	0.636
Diclofenac	-	-	-	-	-	-	-	-	-	-	-	-
Levofloxacin	19.36	0.2409	0.632	21.70	1.56E-02	0.760	0.2915	35.88	0.860	2.319	7.386	0.889
Ibuprofen												
Tetracycline	-	-	-	-	-	-	-	-	-	-	-	-
ZnCl₂												
Methyl Blue	-	-	-	-	-	-	-	-	-	-	-	-
Methyl Orange												
Methyl Green	-	-	-	-	-	-	-	-	-	-	-	-
Crystal Violet	9.17	0.3615	0.883	9.93	5.61E-02	0.868	0.6844	32.18	0.811	1.041	3.780	0.548
Diclofenac	44.49	2.7500	0.936	45.98	1.12E-01	0.971	0.3982	1.16E+07	0.988	1.488	38.718	0.680
Levofloxacin	-	-	-	-	-	-	-	-	-	-	-	-
Ibuprofen												
Tetracycline	-	-	-	-	-	-	-	-	-	-	-	-

Table S4. Constants and correlations for kinetic data fitting sorted by carbon activating agent. *This is the data for the IPD when fit across the entire dataset, rather than in a piecewise manner.

159
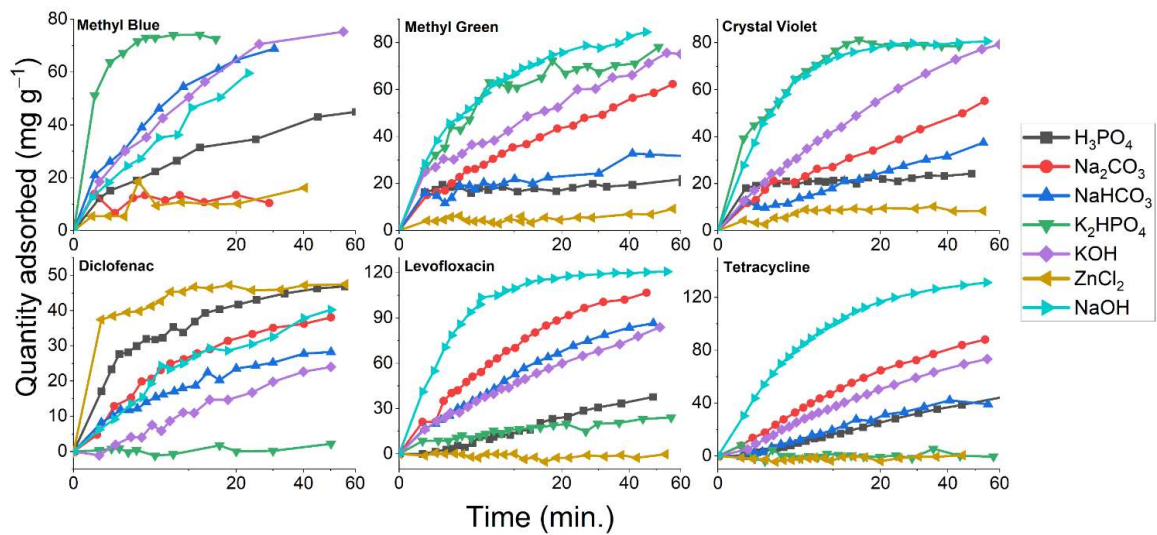
Figure S5. Adjustment of the data collected for kinetic analysis to be graphed versus $\sqrt{t}$ for the purpose of intraparticle diffusion analysis.
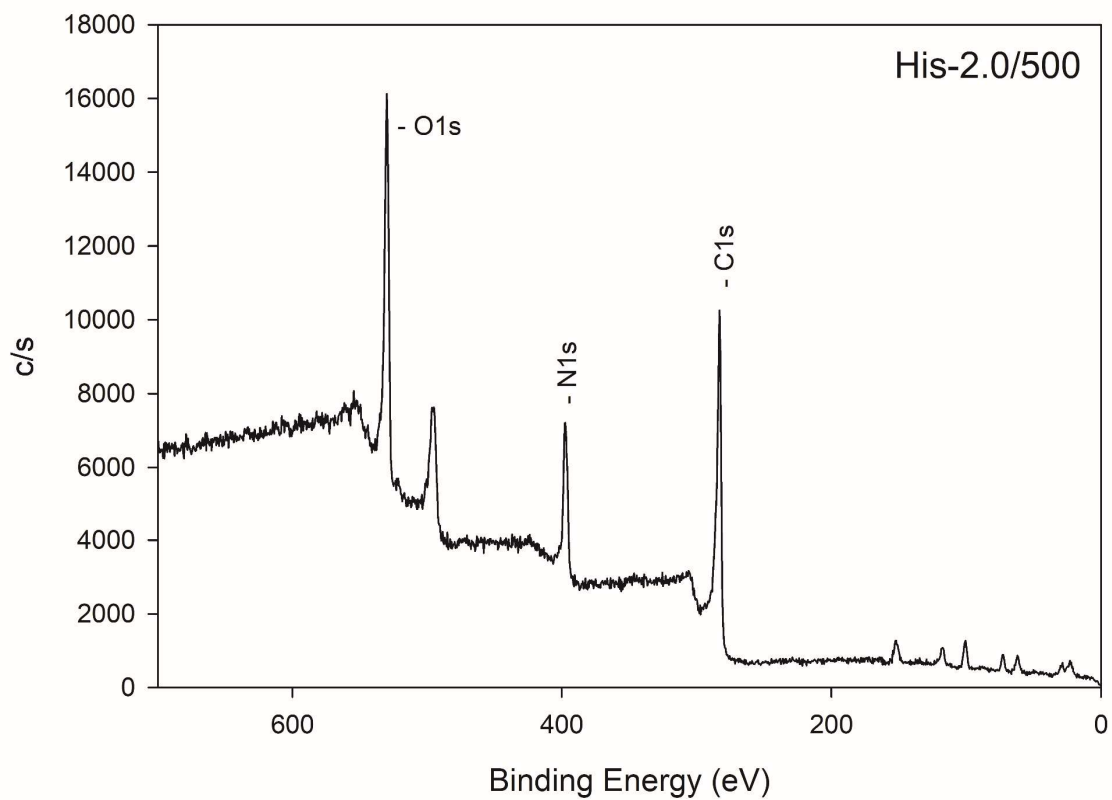
Figure S6. XPS survey for NaOH activated histidine-derived carbon produced at 500 °C, revealing principally the presence of carbon, oxygen, and nitrogen, with some impurities also noted.
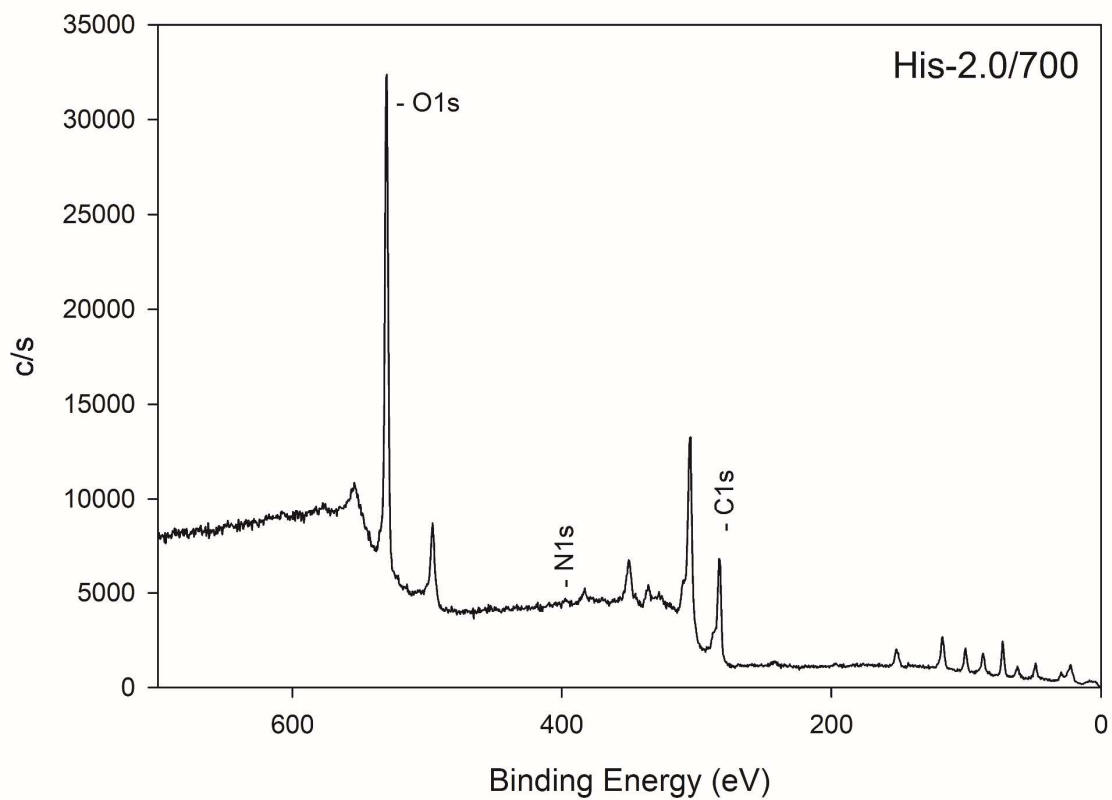
Figure S7. XPS survey for NaOH activated histidine-derived carbon produced at 700 °C, revealing principally the presence of carbon and oxygen, with some impurities also noted.
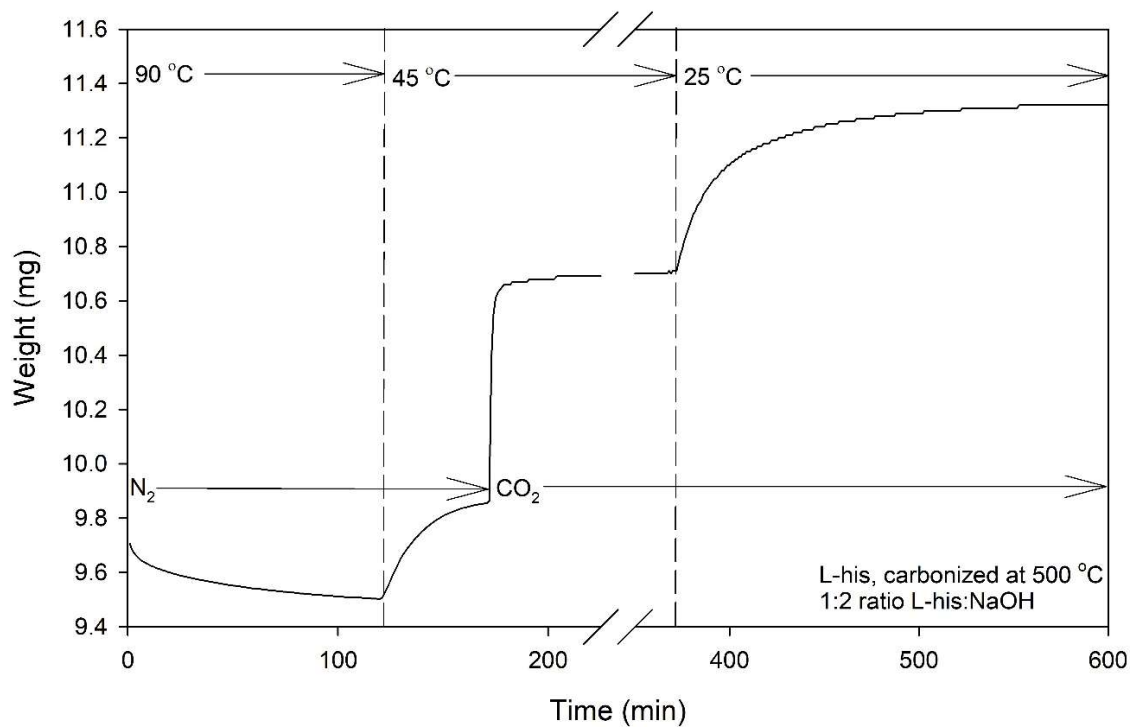
Figure S8. Representative gravimetric CO_2 adsorption analysis with identified gases used at each phase of the isothermal runs at 25 °C and at 45 °C for activated carbons activated with NaOH and carbonized at 500 °C.
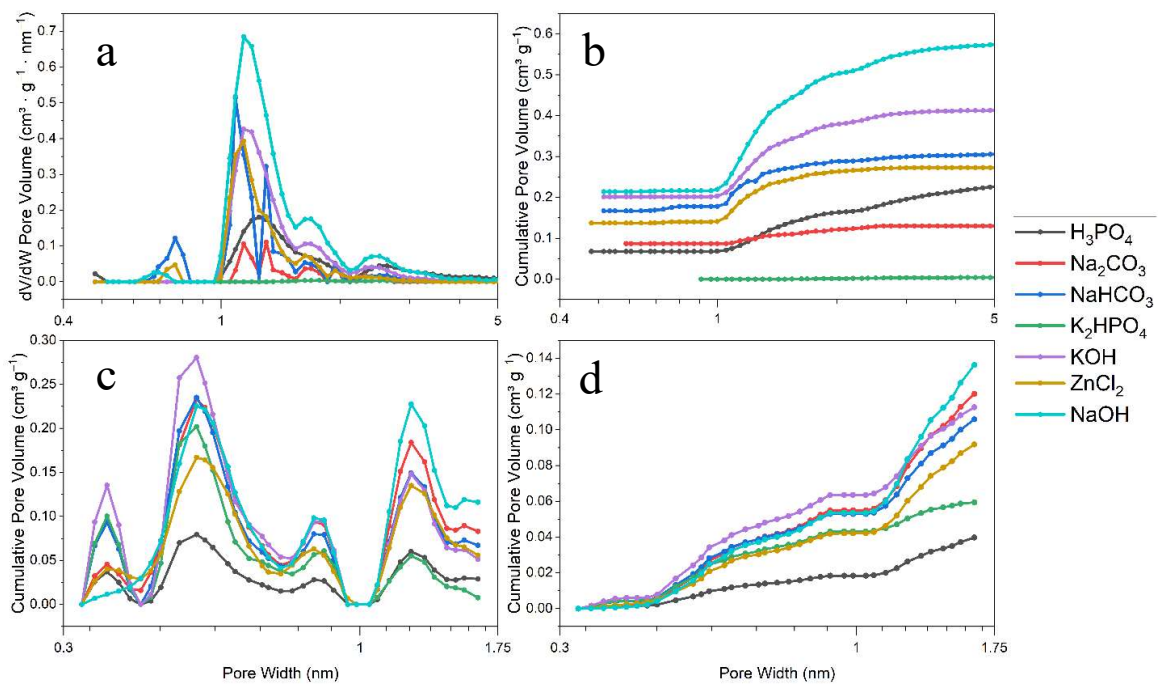
Figure S9. NLDFT pore size distribution and cumulative pore volume plots using N_2 at 77 K (a, b) and CO_2 at 0 °C (c, d) for the porous carbons used in this study.
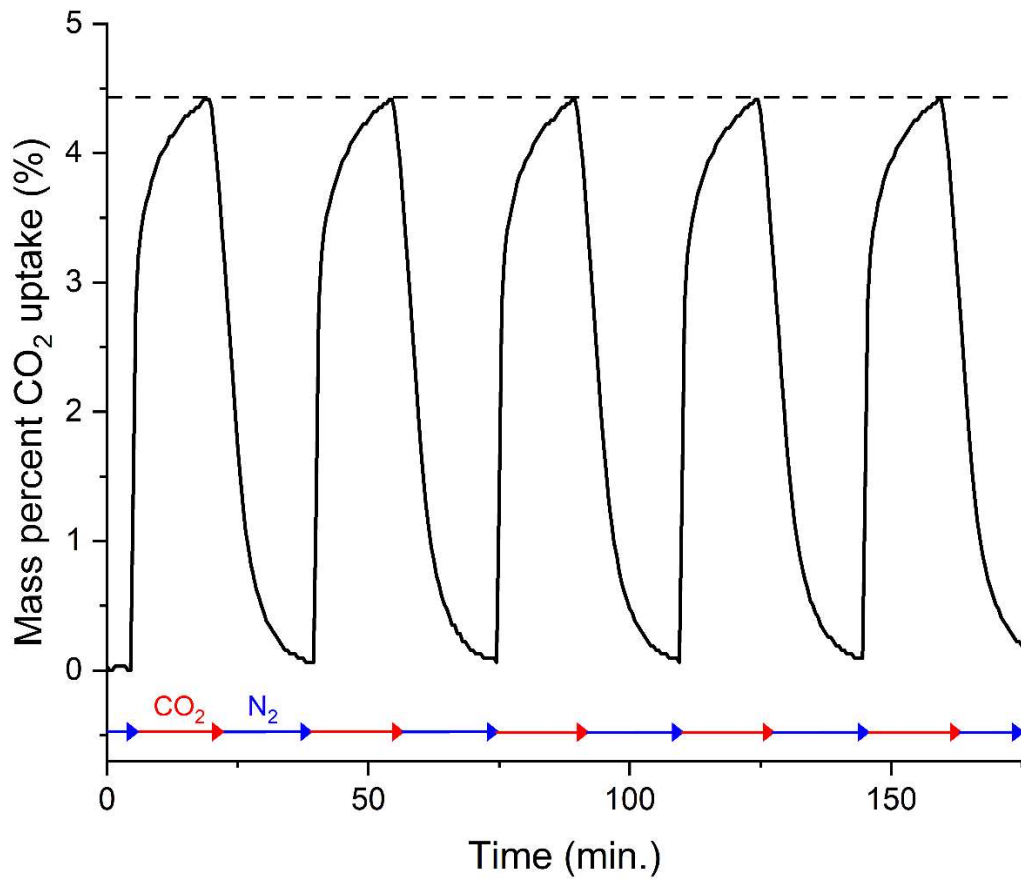
Fig. S10. CO_2/N_2 cycling isotherm at 45 °C for a 3% mass loading of J-S hybrid loaded cellulose.

REFERENCES

1.   Gupta, T., Historical Production and Use of Carbon Materials: The Activated Carbon. In *Carbon: The Black, the Gray and the Transparent*, Springer International Publishing: Cham, 2018; pp 47-70.

2.   Derlet, R. W.; Albertson, T. E., Activated Charcoal - Past, Present and Future. *The Western Journal of Medicine* **1986,** *145* (4), 493-496.

3.   Sing, K. S. W., Adsorption by Active Carbons. In *Adsorption by Powders and Porous Solids*, Ltd., E., Ed. Elsevier: 2014; pp 321 - 392.

4.   Childres, I.; Jauregui, L. A.; Park, W.; Cao, H.; Chen, Y. P., RAMAN SPECTROSCOPY OF GRAPHENE AND RELATED MATERIALS. *New Developments in Photon and Materials Research* **2013**, 403-418.

5.   Wang, L.; Zhao, J.; Sun, Y. Y.; Zhang, S. B., Characteristics of Raman spectra for graphene oxide from ab initio simulations. *J Chem Phys* **2011,** *135* (18), 184503.

6.   Schwan, J.; Ulrich, S.; Batori, V.; Ehrhardt, H.; Silva, S. R. P., Raman spectroscopy on amorphous carbon films. *Journal of Applied Physics* **1996,** *80* (1), 440-447.

7.   Gao, Y.; Yue, Q.; Gao, B.; Li, A., Insight into activated carbon from different kinds of chemical activating agents: A review. *Sci Total Environ* **2020,** *746*, 141094.

8.   Sevilla, M.; Diez, N.; Fuertes, A. B., More Sustainable Chemical Activation Strategies for the Production of Porous Carbons. *ChemSusChem* **2021,** *14* (1), 94-117.

9.   Wu, H.; Tian, D.; Fan, X.; Fan, W.; Zhang, Y.; Jiang, S.; Wen, C.; Ma, Q.; Chen, N.; Xie, X., Highly Efficient Production of l-Histidine from Glucose by Metabolically Engineered Escherichia coli. *ACS Synth Biol* **2020,** *9* (7), 1813-1822.

10.   Zheng, C.; Hu, X.; Sun, X.; Yoo, S. J.; Li, X., Large-scale synthesis of nitrogen-rich hierarchically porous carbon as anode for lithium-ion batteries with high capacity and rate capability. *Electrochimica Acta* **2019,** *306*, 339-349.

11.   Cai, J.-J.; Zhou, Q.-Y.; Gong, X.-F.; Liu, B.; Zhang, Y.-L.; Dai, Y.-K.; Gu, D.-M.; Zhao, L.; Sui, X.-L.; Wang, Z.-B., Metal-free amino acid glycine-derived nitrogen-doped carbon aerogel with superhigh surface area for highly efficient Zn-Air batteries. *Carbon* **2020,** *167*, 75-84.

12.   Yan, J.; Meng, H.; Xie, F.; Yuan, X.; Yu, W.; Lin, W.; Ouyang, W.; Yuan, D., Metal free nitrogen doped hollow mesoporous graphene-analogous spheres as effective electrocatalyst for oxygen reduction reaction. *Journal of Power Sources* **2014,** *245*, 772-778.

13.   Kang, J.; Wang, H.; Ji, S.; Key, J.; Wang, R., Synergy among manganese, nitrogen and carbon to improve the catalytic activity for oxygen reduction reaction. *Journal of Power Sources* **2014,** *251*, 363-369.

14.   Choi, I.-A.; Kwak, D.-H.; Han, S.-B.; Park, J.-Y.; Park, H.-S.; Ma, K.-B.; Kim, D.-H.; Won, J.-E.; Park, K.-W., Doped porous carbon nanostructures as non-precious metal catalysts prepared by amino acid glycine for oxygen reduction reaction. *Applied Catalysis B: Environmental* **2017,** *211*, 235-244.

15.   Jeong, H.; Kim, H. J.; Lee, Y. J.; Hwang, J. Y.; Park, O.-K.; Wee, J.-H.; Yang, C.-M.; Ku, B.-C.; Lee, J. K., Amino acids derived nitrogen-doped carbon materials for electrochemical capacitive energy storage. *Materials Letters* **2015,** *145*, 273-278.

16.   Tran, T.-N.; Jung Kim, H.; Samdani, J. S.; Hwang, J. Y.; Ku, B.-C.; Kwan Lee, J.; Yu, J.-S., A facile in-situ activation of protonated histidine-derived porous carbon for electrochemical capacitive energy storage. *Journal of Industrial and Engineering Chemistry* **2019,** *73*, 316-327.

17.   Zhou, M.; Lin, Y.; Xia, H.; Wei, X.; Yao, Y.; Wang, X.; Wu, Z., A Molecular Foaming and Activation Strategy to Porous N-Doped Carbon Foams for Supercapacitors and CO2 Capture. *Nano-Micro Letters* **2020,** *12* (1).

18.   Peng, C.; Zeng, T.; Kuai, Z.; Li, Z.; Yu, Y.; Zuo, J.; Jin, Y.; Wang, Y.; Li, L., A Self-Activation Green Strategy to Fabricate N/P Co-Doped Carbon for Excellent Electrochemical Performance. *Journal of The Electrochemical Society* **2019,** *166* (14), A3287-A3293.

19.   Huang, H.; Li, C.; Zhu, S.; Wang, H.; Chen, C.; Wang, Z.; Bai, T.; Shi, Z.; Feng, S., Histidine-derived nontoxic nitrogen-doped carbon dots for sensing and bioimaging applications. *Langmuir* **2014,** *30* (45), 13542-8.

20.   Wang, M.; Han, K.; Qi, J.; Li, J.; Teng, Z.; Zhang, J., Heteroatom-Rich Porous Carbons Derived from Nontoxic Green Organic Crystals for High-Performance Symmetric and Asymmetric Supercapacitors with Aqueous/Gel Electrolyte. *ACS Sustainable Chemistry & Engineering* **2020,** *8* (36), 13634-13647.

21.   Chen, Z.; Gao, X.; Wei, X.; Wang, X.; Li, Y.; Wu, T.; Guo, J.; Gu, Q.; Wu, W. D.; Chen, X. D.; Wu, Z.; Zhao, D., Directly anchoring Fe3C nanoclusters and FeNx sites in ordered mesoporous nitrogen-doped graphitic carbons to boost electrocatalytic oxygen reduction. *Carbon* **2017,** *121*, 143-153.

22.   Zhou, H.; Zhou, Y.; Li, L.; Li, Y.; Liu, X.; Zhao, P.; Gao, B., Amino Acid Protic Ionic Liquids: Multifunctional Carbon Precursor for N/S Codoped Hierarchically Porous Carbon Materials toward Supercapacitive Energy Storage. *ACS Sustainable Chemistry & Engineering* **2019,** *7* (10), 9281-9290.

23.   Min, J.; Xu, X.; Li, J.; Ma, C.; Gong, J.; Wen, X.; Chen, X.; Azadmanjiri, J.; Tang, T., Sustainable polylysine conversion to nitrogen-containing porous carbon flakes: Potential application in supercapacitors. *Journal of Applied Polymer Science* **2019,** *136* (48).

24.   Wang, R.; Zhou, T.; Wang, H.; Feng, H.; Ji, S., Lysine-derived mesoporous carbon nanotubes as a proficient non-precious catalyst for oxygen reduction reaction. *Journal of Power Sources* **2014,** *269*, 54-60.

25.   Zhou, H.; Zhou, Y.; Wu, S.; Li, L.; Li, Y.; Guo, M.; Qi, Z.; Feng, C., Synthesis of N/S co-doped porous carbon microspheres based on amino acid protic salt for supercapacitor. *Journal of Alloys and Compounds* **2020,** *829*.

26.   Dong, X.-L.; Li, W.-C.; Jiang, B.; Zhou, Y.-Q.; Lu, A.-H., Using inorganic dynamic porogens for preparing high-surface-area capacitive carbons with tailored micropores. *Journal of Materials Chemistry A* **2019,** *7* (2), 687-692.

27.   Dong, X.-L.; Lu, A.-H.; He, B.; Li, W.-C., Highly microporous carbons derived from a complex of glutamic acid and zinc chloride for use in supercapacitors. *Journal of Power Sources* **2016,** *327*, 535-542.

28.   Ma, G.; Zhang, Z.; Peng, H.; Sun, K.; Ran, F.; Lei, Z., Facile preparation of nitrogen-doped porous carbon for high performance symmetric supercapacitor. *Journal of Solid State Electrochemistry* **2016,** *20* (6), 1613-1623.

29.   Zhang, J.; Qi, L.; Zhu, X.; Yan, X.; Jia, Y.; Xu, L.; Sun, D.; Tang, Y., Proline-derived in situ synthesis of nitrogen-doped porous carbon nanosheets with encaged Fe2O3@Fe3C nanoparticles for lithium-ion battery anodes. *Nano Research* **2017,** *10* (9), 3164-3177.

30.   Ma, Y.; Wu, D.; Wang, T.; Jia, D., Nitrogen, Phosphorus Co-doped Carbon Obtained from Amino Acid Based Resin Xerogel as Efficient Electrode for Supercapacitor. *ACS Applied Energy Materials* **2019,** *3* (1), 957-969.

31.   Wang, Y.; Pan, Y.; Zhu, L.; Guo, N.; Wang, R.; Zhang, Z.; Qiu, S., Structure regulation of amino acids derived nitrogen doped porous carbon nanosheet through facile solid state assembly method. *Microporous and Mesoporous Materials* **2019,** *277*, 36-44.

32.   Choi, C. H.; Park, S. H.; Woo, S. I., Heteroatom doped carbons prepared by the pyrolysis of bio-derived amino acids as highly active catalysts for oxygen electro-reduction reactions. *Green Chem.* **2011,** *13* (2), 406-412.

33.   Gao, X.; Chen, Z.; Yao, Y.; Zhou, M.; Liu, Y.; Wang, J.; Wu, W. D.; Chen, X. D.; Wu, Z.; Zhao, D., Direct Heating Amino Acids with Silica: A Universal Solvent-Free

Assembly Approach to Highly Nitrogen-Doped Mesoporous Carbon Materials. *Advanced Functional Materials* **2016,** *26* (36), 6649-6661.

34.   Maruyama, J.; Fukui, N.; Kawaguchi, M.; Abe, I., Application of nitrogen-rich amino acids to active site generation in oxygen reduction catalyst. *Journal of Power Sources* **2008,** *182* (2), 489-495.

35.   Stepansky, A.; Leustek, T., Histidine biosynthesis in plants. *Amino Acids* **2006,** *30* (2), 127-42.

36.   Alifano, P.; Fani, R.; Lio, P.; Lazcano, A.; Bazzicalupo, M.; Carlomagno, M. S.; Bruni, C. B., Histidine biosynthetic pathway and genes: structure, regulation, and evolution. *Microbiol Rev* **1996,** *60* (1), 44-69.

37.   Eggeling, L.; Bott, M., A giant market and a powerful metabolism: L-lysine provided by Corynebacterium glutamicum. *Appl Microbiol Biotechnol* **2015,** *99* (8), 3387-94.

38.   Scholl, M.; Nguyen, T. Q.; Bruchmann, B.; Klok, H.-A., The thermal polymerization of amino acids revisited; Synthesis and structural characterization of hyperbranched polymers fromL-lysine. *Journal of Polymer Science Part A: Polymer Chemistry* **2007,** *45* (23), 5494-5508.

39.   Santoso, E.; Ediati, R.; Kusumawati, Y.; Bahruji, H.; Sulistiono, D. O.; Prasetyoko, D., Review on recent advances of carbon based adsorbent for methylene blue removal from waste water. *Materials Today Chemistry* **2020,** *16*.

40.   Aljeboree, A. M., Adsorption of crystal violet dye by Fugas Sawdust from aqueous solution. *International Journal of ChemTech Research* **2016,** *9*, 412-423.

41.   Azari, A.; Nabizadeh, R.; Nasseri, S.; Mahvi, A. H.; Mesdaghinia, A. R., Comprehensive systematic review and meta-analysis of dyes adsorption by carbon-based adsorbent materials: Classification and analysis of last decade studies. *Chemosphere* **2020,** *250*, 126238.

42.   Reza, M. S.; Yun, C. S.; Afroze, S.; Radenahmad, N.; Bakar, M. S. A.; Saidur, R.; Taweekun, J.; Azad, A. K., Preparation of activated carbon from biomass and its' applications in water and gas purification, a review. *Arab Journal of Basic and Applied Sciences* **2020,** *27* (1), 208-238.

43.   Chenab, K. K.; Sohrabi, B.; Jafari, A.; Ramakrishna, S., Water treatment: functional nanomaterials and applications from adsorption to photodegradation. *Materials Today Chemistry* **2020,** *16*.

44.   Wang, H.; Xie, R.; Zhang, J.; Zhao, J., Preparation and characterization of distillers' grain based activated carbon as low cost methylene blue adsorbent: Mass transfer and equilibrium modeling. *Advanced Powder Technology* **2018,** *29* (1), 27-35.

45.   EPA, U. *KOWWIN*, 1.69; United States Environmental Protection Agency: Estimation Programs Interface Suite v. 4.11, 2012.

46.   Tsai, R.-S.; Tayar, N. E.; Testa, B.; Ito, Y., Toroidal coil centrifugal partition chromatography, a method for measuring partition coefficients. *Journal of Chromatography A* **1991,** *538* (1), 119-123.

47.   Hansch, C.; Leo, A.; Hoekman, D., *Exploring QSAR - Hydrophobic, Electronic, and Steric Constants*. American Chemical Society Washington, DC 1995; Vol. 2.

48.   Avdeef, A., pH-metric log P. II: Refinement of partition coefficients and ionization constants of multiprotic substances. *J Pharm Sci* **1993,** *82* (2), 183-90.

49.   Childres, I.; Jauregui, L. A.; Park, W.; Cao, H.; Chen, Y. P., Raman spectroscopy of graphene and related materials. In *New developments in photon and materials research*, 2013; pp 1-20.

50.   Shroder, R. E.; Nemanich, R. J.; Glass, J. T., Analysis of the composite structures in diamond thin films by Raman spectroscopy. *Phys Rev B Condens Matter* **1990,** *41* (6), 3738-3745.

51.   Schönherr, J.; Buchheim, J. R.; Scholz, P.; Adelhelm, P., Boehm Titration Revisited (Part I): Practical Aspects for Achieving a High Precision in Quantifying Oxygen-Containing Surface Groups on Carbon Materials. *C* **2018,** *4* (2).

52.   Oickle, A. M.; Goertzen, S. L.; Hopper, K. R.; Abdalla, Y. O.; Andreas, H. A., Standardization of the Boehm titration: Part II. Method of agitation, effect of filtering and dilute titrant. *Carbon* **2010,** *48* (12), 3313-3322.

53.   Goertzen, S. L.; Thériault, K. D.; Oickle, A. M.; Tarasuk, A. C.; Andreas, H. A., Standardization of the Boehm titration. Part I. CO2 expulsion and endpoint determination. *Carbon* **2010,** *48* (4), 1252-1261.

54.   Azizian, S., Kinetic models of sorption: a theoretical analysis. *J Colloid Interface Sci* **2004,** *276* (1), 47-52.

55.   Paunovic, O.; Pap, S.; Maletic, S.; Taggart, M. A.; Boskovic, N.; Turk Sekulic, M., Ionisable emerging pharmaceutical adsorption onto microwave functionalised biochar derived from novel lignocellulosic waste biomass. *J Colloid Interface Sci* **2019,** *547*, 350-360.

56. Qu, Z.; Dong, G.; Zhu, S.; Yu, Y.; Huo, M.; Xu, K.; Liu, M., Recycling of groundwater treatment sludge to prepare nano-rod erdite particles for tetracycline adsorption. *Journal of Cleaner Production* **2020,** *257*.

57. Castro, C. S. d.; Viau, L. N.; Andrade, J. T.; Mendonça, T. A. P.; Gonçalves, M., Mesoporous activated carbon from polyethyleneterephthalate (PET) waste: pollutant adsorption in aqueous solution. *New Journal of Chemistry* **2018,** *42* (17), 14612-14619.

58. Ayawei, N.; Ebelegi, A. N.; Wankasi, D., Modelling and Interpretation of Adsorption Isotherms. *Journal of Chemistry* **2017,** *2017*, 1-11.

59. Rouquerol, F.; Rouquerol, J.; Sing, K. S. W.; Llewellyn, P.; Maurin, G., *Adsorption by powders and porous solids: principles, methodology and applications*. Second ed.; Elsevier: Academic Press, 2014.

60. Wang, J.; Guo, X., Adsorption kinetic models: Physical meanings, applications, and solving methods. *J Hazard Mater* **2020,** *390*, 122156.

61. Tan, K. L.; Hameed, B. H., Insight into the adsorption kinetics models for the removal of contaminants from aqueous solutions. *Journal of the Taiwan Institute of Chemical Engineers* **2017,** *74*, 25-48.

62. Kajjumba, G. W.; Emik, S.; Atakan Öngen; Özcan, H. K.; Aydın, S., Modelling of Adsorption Kinetic Processes - Errors, Theory and Application. In *Advanced Sorption Process Applications*, Edebali, S., Ed. IntechOpen: 2018.

63. Simonin, J.-P., On the comparison of pseudo-first order and pseudo-second order rate laws in the modeling of adsorption kinetics. *Chemical Engineering Journal* **2016,** *300*, 254-263.

64. Feely, R. A.; Sabine, C. L.; Lee, K.; Berelson, W.; Kleypas, J.; Fabry, V. J.; Millero, F. J., Impact of Anthropogenic CO_2 on the $CaCO_3$ System in the Oceans. *Science* **2004,** *305* (5682), 362-366.

65. Dlugokencky, E.; Tans, P., Trends in Atmospheric CO2. National Oceanic and Atmostpheric Administration: Earth Systems Research Laboratory, 2017.

66. Paltsev, S.; Monier, E.; Chen, H.; Fant, C.; Morris, J.; Rielly, J.; Sokolov, A.; Huang, J.; Strzepek, K.; Ejaz, Q.; KickLighter, D.; Kutkiewicz, S.; Scott, J.; Schlosser, A.; Jacoby, H.; Resutek, A.; Batholomay, J.; Slinn, A. *Energy & Climate Outlook*; MIT: MIT, 2014.

67. Haszeldine, R. S., Carbon Capture and Storage: How Green Can Black Be? *Science* **2009,** *325* (5948), 1647.

68.   Zeng, S.; Zhang, X.; Bai, L.; Zhang, X.; Wang, H.; Wang, J.; Bao, D.; Li, M.; Liu, X.; Zhang, S., Ionic-Liquid-Based CO2 Capture Systems: Structure, Interaction and Process. *Chemical Reviews* **2017,** *117* (14), 9625-9673.

69.   Banu, L. A.; Wang, D.; Baltus, R. E., Effect of Ionic Liquid Confinement on Gas Separation Characteristics. *Energy & Fuels* **2013,** *27* (8), 4161-4166.

70.   Zhou, J.; Mok, M. M.; Cowan, M. G.; McDanel, W. M.; Carlisle, T. K.; Gin, D. L.; Noble, R. D., High-Permeance Room-Temperature Ionic-Liquid-Based Membranes for CO2/N2 Separation. *Industrial & Engineering Chemistry Research* **2014,** *53* (51), 20064-20067.

71.   Kruk, M.; Jaroniec, M., Gas adsorption characterization of ordered organic-inorganic nanocomposite materials. *Chemistry of Materials* **2001,** *13* (10), 3169-3183.

72.   Merkel, T. C.; Lin, H.; Wei, X.; Baker, R., Power plant post-combustion carbon dioxide capture: An opportunity for membranes. *Journal of Membrane Science* **2010,** *359* (1–2), 126-139.

73.   Li, J.-R.; Ma, Y.; McCarthy, M. C.; Sculley, J.; Yu, J.; Jeong, H.-K.; Balbuena, P. B.; Zhou, H.-C., Carbon dioxide capture-related gas adsorption and separation in metal-organic frameworks. *Coordination Chemistry Reviews* **2011,** *255* (15–16), 1791-1823.

74.   Al-Azzawi, O. M.; Hofmann, C. M.; Baker, G. A.; Baker, S. N., Nanosilica-supported polyethoxyamines as low-cost, reversible carbon dioxide sorbents. *J Colloid Interface Sci* **2012,** *385* (1), 154-9.

75.   Zhu, J.; Baker, S. N., Lewis Base Polymers for Modifying Sorption and Regeneration Abilities of Amine-Based Carbon Dioxide Capture Materials. *ACS Sustainable Chemistry & Engineering* **2014,** *2* (12), 2666-2674.

76.   Liu, L.; Xie, Z.-H.; Deng, Q.-F.; Hou, X.-X.; Yuan, Z.-Y., One-pot carbonization enrichment of nitrogen in microporous carbon spheres for efficient CO2capture. *J. Mater. Chem. A* **2017,** *5* (1), 418-425.

77.   Wang, J.; Li, G.; Li, Z.; Tang, C.; Feng, Z.; An, H.; Liu, H.; Liu, T.; Li, C., A highly selective and stable ZnO-ZrO2 solid solution catalyst for CO_2 hydrogenation to methanol. *Science advances* **2017,** *3* (10).

78.   Alabadi, A.; Abbood, H. A.; Li, Q.; Jing, N.; Tan, B., Imine-Linked Polymer Based Nitrogen-Doped Porous Activated Carbon for Efficient and Selective CO2 Capture. *Sci Rep* **2016,** *6*, 38614.

79.   Balahmar, N.; Al-Jumialy, A. S.; Mokaya, R., Biomass to porous carbon in one step: directly activated biomass for high performance CO2 storage. *J. Mater. Chem. A* **2017,** *5* (24), 12330-12339.

80.   Caturla, F. M.-S., M.; Rodriguez-Reinoso, F., Preparation of activated carbon by chemical activation with ZnCl2. *Carbon* **1991,** *29* (7).

81.   Choi, S.; Drese, J. H.; Jones, C. W., Adsorbent materials for carbon dioxide capture from large anthropogenic point sources. *ChemSusChem* **2009,** *2* (9), 796-854.

82.   Cukierman, A. L.; Bonelli, P. R., Agricultural wastes as potential feedstock for activated carbons development. In *Agricultural Research Updates*, Nova Science Publishers, Inc.: 2017; Vol. 18, pp 1-30.

83.   Wickramaratne, N. P.; Jaroniec, M., Importance of small micropores in CO2 capture by phenolic resin-based activated carbon spheres. *Journal of Materials Chemistry A* **2013,** *1* (1), 112-116.

84.   Zhu, X.; Chai, S.; Tian, C.; Fulvio, P. F.; Han, K. S.; Hagaman, E. W.; Veith, G. M.; Mahurin, S. M.; Brown, S.; Liu, H.; Dai, S., Synthesis of Porous, Nitrogen-Doped Adsorption/Diffusion Carbonaceous Membranes for Efficient CO2 Separation. *Macromolecular Rapid Communications* **2013,** *34* (5), 452-459.

85.   Mahurin, S. M.; Fulvio, P. F.; Hillesheim, P. C.; Nelson, K. M.; Veith, G. M.; Dai, S., Directed Synthesis of Nanoporous Carbons from Task-Specific Ionic Liquid Precursors for the Adsorption of CO2. *ChemSusChem* **2014,** *7* (12), 3284-3289.

86.   Primo, A.; Forneli, A.; Corma, A.; García, H., From Biomass Wastes to Highly Efficient CO2 Adsorbents: Graphitisation of Chitosan and Alginate Biopolymers. *ChemSusChem* **2012,** *5* (11), 2207-2214.

87.   Wickramaratne, N. P.; Xu, J.; Wang, M.; Zhu, L.; Dai, L.; Jaroniec, M., Nitrogen Enriched Porous Carbon Spheres: Attractive Materials for Supercapacitor Electrodes and CO2 Adsorption. *Chemistry of Materials* **2014,** *26* (9), 2820-2828.

88.   Liu, J.; Wickramaratne, N. P.; Qiao, S. Z.; Jaroniec, M., Molecular-based design and emerging applications of nanoporous carbon spheres. *Nature Materials* **2015,** *14*, 763.

89.   Dassanayake, R. S.; Gunathilake, C.; Abidi, N.; Jaroniec, M., Activated carbon derived from chitin aerogels: preparation and CO2 adsorption. *Cellulose* **2018,** *25* (3), 1911-1920.

90.   Alhwaige, A. A.; Ishida, H.; Qutubuddin, S., Carbon Aerogels with Excellent CO2 Adsorption Capacity Synthesized from Clay-Reinforced Biobased Chitosan-Polybenzoxazine Nanocomposites. *ACS Sustainable Chemistry & Engineering* **2016,** *4* (3), 1286-1295.

91.   Leżańska, M.; Olejniczak, A.; Łukaszewicz, J. P., Hierarchical porous carbon templated with silica spheres of a diameter of 14 nm from pure chitosan or a chitosan/ZnCl2 solution. *Journal of Porous Materials* **2018,** *25* (6), 1633-1648.

92.   Fulvio, P. F.; Lee, J. S.; Mayes, R. T.; Wang, X.; Mahurin, S. M.; Dai, S., Boron and nitrogen-rich carbons from ionic liquid precursors with tailorable surface properties. *Physical Chemistry Chemical Physics* **2011,** *13* (30), 13486-13491.

93.   Lee, J. S.; Wang, X.; Luo, H.; Dai, S., Fluidic Carbon Precursors for Formation of Functional Carbon under Ambient Pressure Based on Ionic Liquids. *Advanced Materials* **2010,** *22* (9), 1004-+.

94.   Lee, J. S.; Wang, X. Q.; Luo, H. M.; Baker, G. A.; Dai, S., Facile Ionothermal Synthesis of Microporous and Mesoporous Carbons from Task Specific Ionic Liquids. *Journal of the American Chemical Society* **2009,** *131* (13), 4596-+.

95.   Wang, X.; Dai, S., Ionic Liquids as Versatile Precursors for Functionalized Porous Carbon and Carbon-Oxide Composite Materials by Confined Carbonization. *Angewandte Chemie-International Edition* **2010,** *49* (37), 6664-6668.

96.   Fulvio, P. F.; Hillesheim, P. C.; Bauer, J. C.; Mahurin, S. M.; Dai, S., Magadiite templated high surface area graphene-type carbons from metal-halide based ionic liquids. *Journal of Materials Chemistry A* **2013,** *1* (1), 59-62.

97.   Fulvio, P. F.; Hillesheim, P. C.; Oyola, Y.; Mahurin, S. M.; Veith, G. M.; Dai, S., A new family of fluidic precursors for the self-templated synthesis of hierarchical nanoporous carbons. *Chemical Communications* **2013,** *49* (66), 7289-7291.

98.   Drage, T. C.; Blackman, J. M.; Pevida, C.; Snape, C. E., Evaluation of Activated Carbon Adsorbents for CO2 Capture in Gasification. *Energy & Fuels* **2009,** *23* (5), 2790-2796.

99.   Yu, J.; Guo, M.; Muhammad, F.; Wang, A.; Zhang, F.; Li, Q.; Zhu, G., One-pot synthesis of highly ordered nitrogen-containing mesoporous carbon with resorcinol–urea–formaldehyde resin for CO2 capture. *Carbon* **2014,** *69*, 502-514.

100.   Sevilla, M.; Valle-Vigón, P.; Fuertes, A. B., N-Doped Polypyrrole-Based Porous Carbons for CO2 Capture. *Advanced Functional Materials* **2011,** *21* (14), 2781-2787.

101.   Grassie, N.; McGuchan, R., Pyrolysis of polyacrylonitrile and related polymers—II: The effect of sample preparation on the thermal behaviour of polyacrylonitrile. *European Polymer Journal* **1971,** *7* (8), 1091-1104.

102.   Mrozek, A.; Karolak-Wojciechowska, J.; Kieć-Kononowicz, K., Five-membered heterocycles. Part III. Aromaticity of 1,3-imidazole in 5+n hetero-bicyclic molecules. *Journal of Molecular Structure* **2003,** *655* (3), 397-403.

103.   Jiang, J.; He, Y.; Li, S.; Cui, H., Amino acids as the source for producing carbon nanodots: microwave assisted one-step synthesis, intrinsic photoluminescence property

and intense chemiluminescence enhancement. *Chem Commun (Camb)* **2012,** *48* (77), 9634-6.

104.   Scholl, M.;   Nguyen, T. Q.;   Bruchmann, B.; Klok, H.-A., The thermal polymerization of amino acids revisited; Synthesis and structural characterization of hyperbranched polymers from L-lysine. *Journal of Polymer Science Part A: Polymer Chemistry* **2007,** *45* (23), 5494-5508.

105.   Erdmenger, T.;   Vitz, J.;   Wiesbrock, F.; Schubert, U. S., Influence of different branched alkyl side chains on the properties of imidazolium-based ionic liquids. *Journal of Materials Chemistry* **2008,** *18* (43), 5267-5273.

106.   Lillo-Ródenas, M. A.;   Cazorla-Amorós, D.; Linares-Solano, A., Understanding chemical reactions between carbons and NaOH and KOH: An insight into the chemical activation mechanism. *Carbon* **2003,** *41* (2), 267-275.

107.   Jagiello, J., Stable Numerical Solution of the Adsorption Integral Equation Using Splines. *Langmuir* **1994,** *10* (8), 2778-2785.

108.   Programme, U. N. E. *Emissions Gap Report 2020*; Nairobi: 2020.

109.   Kumar, A.;   Singh, P.;   Raizada, P.; Hussain, C. M., Impact of COVID-19 on greenhouse gases emissions: A critical review. *Sci Total Environ* **2021,** *806* (Pt 1), 150349.

110.   Asghar, U.;   Rafiq, S.;   Anwar, A.;   Iqbal, T.;   Ahmed, A.;   Jamil, F.;   Khurram, M. S.;   Akbar, M. M.;   Farooq, A.;   Shah, N. S.; Park, Y.-K., Review on the progress in emission control technologies for the abatement of CO2, SOx and NOx from fuel combustion. *Journal of Environmental Chemical Engineering* **2021,** *9* (5).

111.   Figueroa, J. D.; Fout, T.; Plasynski, S.; McIlvried, H.; Srivastava, R. D., Advances in CO2 capture technology—The U.S. Department of Energy's Carbon Sequestration Program. *International Journal of Greenhouse Gas Control* **2008,** *2* (1), 9-20.

112.   Rashidi, N. A.; Yusup, S., An overview of activated carbons utilization for the post-combustion carbon dioxide capture. *Journal of CO2 Utilization* **2016,** *13*, 1-16.

113.   Płotka-Wasylka, J.;   de la Guardia, M.;   Andruch, V.; Vilková, M., Deep eutectic solvents vs ionic liquids: Similarities and differences. *Microchemical Journal* **2020,** *159*.

114.   Zhang, Z.;   Kang, N.;   Zhou, J.;   Li, X.;   He, L.; Sui, H., Novel Synthesis of Choline-Based Amino Acid Ionic Liquids and Their Applications for Separating Asphalt from Carbonate Rocks. *Nanomaterials (Basel)* **2019,** *9* (4).

115.   Florek, J.;   Guillet-Nicolas, R.; Kleitz, F., Ordered mesoporous silica: synthesis and applications. In *Functional materials: Synthesis and applications*, De Gruyter: 2014; pp 61 - 100.

116. Glover, T. G.; Dunne, K. I.; Davis, R. J.; LeVan, M. D., Carbon–silica composite adsorbent: Characterization and adsorption of light gases. *Microporous and Mesoporous Materials* **2008,** *111* (1-3), 1-11.

117. Janekarn, I.; Hunt, A. J.; Ngernyen, Y.; Youngme, S.; Supanchaiyamat, N., Graphitic mesoporous carbon-silica composites from low-value sugarcane by-products for the removal of toxic dyes from wastewaters. *R Soc Open Sci* **2020,** *7* (9), 200438.

118. Yang, X.; Huang, H.; Li, Z.; Zhong, M.; Zhang, G.; Wu, D., Preparation and lithium-storage performance of carbon/silica composite with a unique porous bicontinuous nanostructure. *Carbon* **2014,** *77*, 275-280.

119. Sing, K. S. W.; Rouquerol, F.; Llewellyn, P.; Rouquerol, J., Assesment of Microporosity. In *Adsorption by Powders and Porous Solids*, Ltd., E., Ed. Elsevier: 2014; pp 301 - 320.

120. Li, L.; Liu, D.; Guo, Z.; Liu, Y.; Chu, W., Improved Facile synthesis of mesoporous SBA-15-CTA using citric acid under mild conditions. *Journal of Solid State Chemistry* **2020,** *282*, 1-9.

121. Loganathan, S.; Tikmani, M.; Ghoshal, A. K., Novel pore-expanded MCM-41 for CO2 capture: synthesis and characterization. *Langmuir* **2013,** *29* (10), 3491-9.

122. Goeppert, A.; Meth, S.; Prakash, G. K. S.; Olah, G. A., Nanostructured silica as a support for regenerable high-capacity organoamine-based CO_2 sorbents. *Energy and Environmental Science* **2010,** *3*, 1949 - 1960.

123. Passos, H.; Freire, M. G.; Coutinho, J. A., Ionic liquid solutions as extractive solvents for value-added compounds from biomass. *Green Chem* **2014,** *16* (12), 4786-4815.

124. Dlugokencky, E.; Tans, P. Trends in Atmospheric Carbon Dioxide. www.esrl.noaa.gov/gmd/ccgg/trends/ (accessed July).

125. Paltsev, S.; Monier, E.; Chen, H.; Fant, C.; Morris, J.; Reilly, J.; Sokolov, A.; Huang, J.; Strzepek, K.; Ejaz, Q.; Kicklighter, D.; Dutkiewicz, S.; Scott, J.; Schlosser, A.; Jacoby, H.; Resutek, A.; Bartholomay, J.; Slinn, A. *2014 Energy & Climate Outlook*; MIT: 2004.

126. Carvalho, P. J.; Kurnia, K. A.; Coutinho, J. A., Dispelling some myths about the CO2 solubility in ionic liquids. *Phys Chem Chem Phys* **2016,** *18* (22), 14757-71.

127. Yaumi, A. L.; Bakar, M. Z. A.; Hameed, B. H., Recent advances in functionalized composite solid materials for carbon dioxide capture. *Energy* **2017,** *124*, 461-480.

128. Luis, P.; Van Gerven, T.; Van der Bruggen, B., Recent developments in membrane-based technologies for $CO2$ capture. *Progress in Energy and Combustion Science* **2012,** *38* (3), 419-448.

129. Sun, N.; Tang, Z.; Wei, W.; Snape, C. E.; Sun, Y., Solid Adsorbents for Low-Temperature $CO2$ Capture with Low-Energy Penalties Leading to More Effective Integrated Solutions for Power Generation and Industrial Processes. *Frontiers in Energy Research* **2015,** *3*.

130. Lee, Z. H.; Lee, K. T.; Bhatia, S.; Mohamed, A. R., Post-combustion carbon dioxide capture: Evolution towards utilization of nanomaterials. *Renewable and Sustainable Energy Reviews* **2012,** *16* (5), 2599-2609.

131. Wilfong, W. C.; Gray, M. L.; Kail, B. W.; Howard, B. H., Pelletization of Immobilized Amine Carbon Dioxide Sorbents with Fly Ash and Poly(vinyl chloride). *Energy Technology* **2016,** *4* (5), 610-619.

132. Hu, Y.; Liu, X.; Zhou, Z.; Liu, W.; Xu, M., Pelletization of MgO-based sorbents for intermediate temperature $CO 2$ capture. *Fuel* **2017,** *187*, 328-337.

133. Manovic, V.; Anthony, E. J., Screening of Binders for Pelletization of CaO-Based Sorbents for $CO2$Capture†. *Energy & Fuels* **2009,** *23* (10), 4797-4804.

134. Rezaei, F.; Sakwa-Novak, M. A.; Bali, S.; Duncanson, D. M.; Jones, C. W., Shaping amine-based solid $CO2$ adsorbents: Effects of pelletization pressure on the physical and chemical properties. *Microporous and Mesoporous Materials* **2015,** *204*, 34-42.

135. Ribeiro, R. P. P. L.; Grande, C. A.; Rodrigues, A. E., Activated carbon honeycomb monolith – Zeolite 13X hybrid system to capture $CO2$ from flue gases employing Electric Swing Adsorption. *Chemical Engineering Science* **2013,** *104*, 304-318.

136. Rezaei, F.; Mosca, A.; Webley, P.; Hedlund, J.; Xiao, P., Comparison of Traditional and Structured Adsorbents for $CO2$ Separation by Vacuum-Swing Adsorption. *Industrial and Engineering Chemistry Research* **2010,** *49*, 4832-4841.

137. Thiruvenkatachari, R.; Su, S.; An, H.; Yu, X. X., Post combustion $CO2$ capture by carbon fibre monolithic adsorbents. *Progress in Energy and Combustion Science* **2009,** *35* (5), 438-455.

138. Rezaei, F.; Lively, R. P.; Labreche, Y.; Chen, G.; Fan, Y.; Koros, W. J.; Jones, C. W., Aminosilane-grafted polymer/silica hollow fiber adsorbents for CO(2) capture from flue gas. *ACS Appl Mater Interfaces* **2013,** *5* (9), 3921-31.

139.   Lively, R. P.; Chance, R. R.; Kelley, B. T.; Deckman, H. W.; Drese, J. H.; Jones, C. W.; Koros, W. J., Hollow Fiber Adsorbents for CO_2 Removal from Flue Gas. *Industrial and Engineering Chemistry Research* **2009,** *48*, 7314-7324.

140.   Labreche, Y.; Lively, R. P.; Rezaei, F.; Chen, G.; Jones, C. W.; Koros, W. J., Post-spinning infusion of poly(ethyleneimine) into polymer/silica hollow fiber sorbents for carbon dioxide capture. *Chemical Engineering Journal* **2013,** *221*, 166-175.

141.   Esa, F.; Tasirin, S. M.; Rahman, N. A., Overview of Bacterial Cellulose Production and Application. *Agriculture and Agricultural Science Procedia* **2014,** *2*, 113-119.

142.   Iguchi, M.; Yamanaka, S.; Budhiono, A., Bacterial cellulose-a masterpiece of nature's arts. *Journal of Materials Science* **2000,** *35*, 261-270.

143.   Plaza, M. G.; Pevida, C.; Arias, B.; Fermoso, J.; Arenillas, A.; Rubiera, F.; Pis, J. J., Application of thermogravimetric analysis to the evaluation of aminated solid sorbents for CO2 capture. *Journal of Thermal Analysis and Calorimetry* **2008,** *92* (2), 601-606.

144.   Monazam, E. R.; Shadle, L. J.; Miller, D. C.; Pennline, H. W.; Fauth, D. J.; Hoffman, J. S.; Gray, M. L., Equilibrium and kinetics analysis of carbon dioxide capture using immobilized amine on a mesoporous silica. *AIChE Journal* **2013,** *59* (3), 923-935.

145.   Zeleňák, V.; Badaničová, M.; Halamová, D.; Čejka, J.; Zukal, A.; Murafa, N.; Goerigk, G., Amine-modified ordered mesoporous silica: Effect of pore size on carbon dioxide capture. *Chemical Engineering Journal* **2008,** *144* (2), 336-342.

VITA

Nathan Bays was born in Mehlville, MO on Feb. 27, 1994, to parents Kevin Bays and Christine Mayse. Early on in life he moved to the Camdenton, MO on the Lake of the Ozarks, alongside his parents and two sisters, Keiley and Lauren.

Growing up Nathan's interests included enjoying and exploring nature, delving into science, creating music, and reading, watching, or playing fantasy. Though high school saw all these interests deepen, it was probably the impact of Mr. Reeves and his biology courses that ultimately led to the general pursuit of science as a career path. Finally, in his senior year of high school, Nathan first took a chemistry course and quickly found an interest he would go to college and ultimately graduate school to pursue.

While at Lindenwood University, Nathan pursued not only a degree in chemistry, but also Kelli M. (from the aforementioned biology classes). With the encouragement of his instructors, Nathan applied for and was eventually accepted into the graduate program at the University of Missouri. In May 2016, Nathan graduated from Lindenwood University with a B.S. in Chemistry.

While at the University of Missouri, Nathan pursued environmentally minded research with nanomaterials. It was also during this time that he would marry Kelli (now Dr. Kelli Bays) in Grand Teton National Park.

In December 2021, Nathan Robert Bays graduated from the University of Missouri with a Ph.D. in Chemistry.